=========================== **PHYSICS** ===========================

New Forms of Crystalline Carbon

Yu. M. Korolev

Presented by Academician N.P. Yushkin May 12, 2003

Received May 14, 2003

This paper presents the X-ray crystallography of various carbon materials produced by pyrolysis of light hydrocarbons under nonequilibrium conditions in different regimes in supersonic flows, which makes it possible to synthesize various metastable carbonic structures.

The materials were obtained by Yu.A. Moiseev (Institute of Chemistry of Oil and Natural Resources, Academy of Sciences of Kazakhstan, Gur'ev, Kazakhstan) who specially designed a 10-kW dc plasmatron with the supersonic Laval nozzle for the quenching of reaction products with a rate of 10^8 K/s [1, 2]. Ethylene (~99.99%) and argon (~99.99%) were used as a hydrocarbon material and plasma-producing gas, respectively. Their flow rates varied in the experiments. The average temperature in the plasma jet ranged between 1000 and 4500 K.

The X-ray crystallography of 15 specimens of synthesized carbonic materials were carried out on a DRON-1.5 diffractometer with modernized collimation (CuK_α radiation). The spectra were handled and identified by the PowTool software package. Test specimens prepared on mica plates were studied with an EVM-100 electron microscope.

The diffraction spectra of all test specimens include reflections from two X-ray amorphous phases: graphite-like (Gph) with $d_{002} = 3.55–3.42$ Å and polynaphthenic (Nph) with $d = 4.7$ Å (γ line). As is known [3], such phases exist in many natural and artificial carbonic materials (Figs. 1a, 1b, Table 1). The size L_{csr} of coherent-scattering regions for these phases lies in the range 30–120 Å.

It was found that the main feature of most specimens under study is the presence of sharp pronounced reflections from crystalline structures with different sets of interplanar spacings d.

The systematic analysis of the quantity d for all crystalline components showed that most specimens contain a common phase with the fcc cell. It was established that this crystalline phase in the pure form, along with the amorphous Gph and Nph components, exists in specimen nos. 5 and 7 (Fig. 1b, Table 1). The values of θ, d, and hkl for this phase are listed in Table 2.

Reflections typical of structures with a lower (monoclinic) symmetry were identified in the diffraction spectra of some specimens (Table 1, Fig. 1a). The X-ray parameters of these structures are listed in Tables 1 and 2.

We emphasize that the time τ of the presence of a hydrocarbon in the reactor, as well as the quenching rate, has a significant effect on the phase composition of the products. In the first series of experiments ($10^4 < \tau < 10^5$ s and quenching rate $< 10^5$ K/s), only the Gph, Nph, and fcc phases were usually formed. In the second series of experiments ($10^3 < \tau < 10^4$ s and quenching
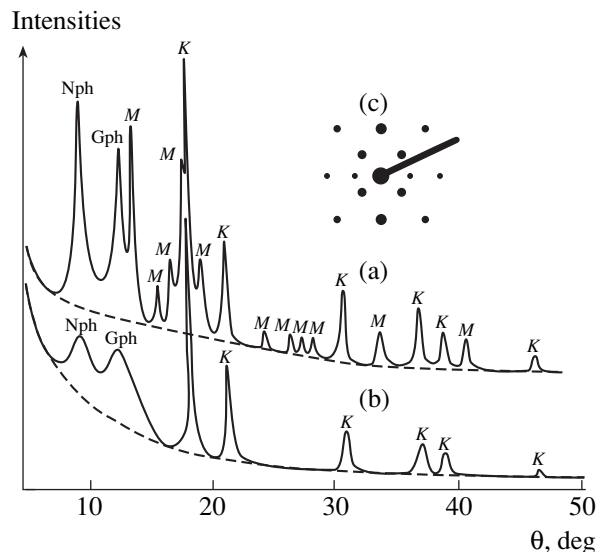

Fig. 1. X-ray diffraction spectra from the specimens produced by the plasma chemical synthesis: (a) specimen 3, (b) specimens 5 and 7, and (c) point electron diffraction pattern from specimen 3; Nph is the polynaphthenic phase, Gph is the graphite-like phase; K are reflections from the fcc cell, and M are reflections from the phase with a monoclinic cell.

Topchiev Institute of Petrochemical Synthesis,
Russian Academy of Sciences,
Leninskiĭ pr. 29, Moscow, 117912 Russia
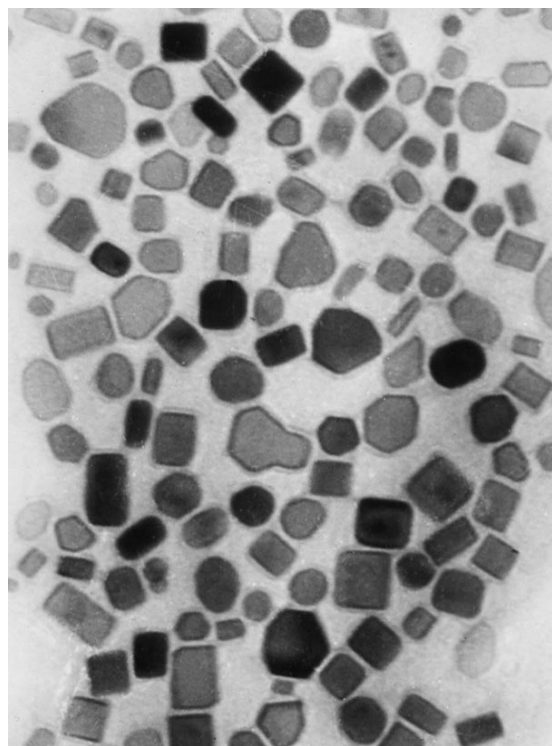*e-mail: tips@ips.ac.ru*

Fig. 2. Electron microscope photograph of specimen 3 with a magnification of 250000.

rate $>10^6$ K/s), crystalline carbon components characterized by a monoclinic cell, i.e., by a lower symmetry, appeared in the products along with the above phases.

The analysis of the morphology of carbon particles with an electron microscope provided interesting results. As a rule, the products obtained with low quenching rates contain irregular-shaped particles with diffuse edges. At high quenching rates, particles with surprisingly regular crystallographic shapes—squares, hexagons, polygons, etc.—are formed (see Fig. 2).

Particles with a similar morphology were described in [4, 5]. In addition, it was shown in [5] that the condensation of carbon plasma flows in vacuum was accompanied by the formation of a phase characterized by the bcc cell with the lattice parameter that I estimated as $a = 4.28$ Å ($k = 30.1$). Heating transforms this phase to hexagonal graphite.

The X-ray diffraction spectra of the PAN-C_{60} crystalline composite (after its heating by IR radiation up to 1073 K) exhibit three pronounced reflections [6]. Carbon vapors formed from C_{60} fullerene at 773 K are probably crystallized into new crystalline forms.

Thus, one can conclude that a disperse crystalline carbonic material is formed in the supersonic recondensation of carbon-containing high-temperature flows. The analysis of the experimental data indicates that the structure of the electron shell of carbon is highly variable. This property is responsible for the variety of crystalline forms of carbon formed in a plasmatron during the pyrolysis of hydrocarbons due to structural modification and dehydrogenization. These carbon forms have unique structural parameters and morphology.

Table 1. X-ray diffraction characteristics of the carbon products obtained by plasma pyrolysis

Speci-men no.	Phase composition				Cell parameters	K^*
	Nph	Gph	fcc	monoclinic structures		
3	+	+	+	+	$a = 4.045$ Å; $b = 5.61$ Å; $c = 8.40$ Å; $\beta = 104.7°$; $V = 184.3$ Å^3	55.9
5	+	+	+		$a^{**} = 4.257$ Å, $V = 77.2$ Å^3	43.3
7	+	+	+			
8	+	+		+	$a = 6.11$ Å; $b = 5.60$ Å; $c = 3.44$ Å; $\beta = 102.4°$; $V = 111.0$ Å^3	58.4
10	+	+	+			
12			+			
13			+			
14	+	+	+			
16	+	+				
17	+	+	+			
18	+	+	+			
22	+	+	+			
23	+	+		+	$a = 7.35$ Å; $b = 3.03$ Å; $c = 4.97$ Å; $\beta = 94.0°$; $V = 110.5$ Å^3	49.8
24	+	+		+	$a = 7.69$ Å; $b = 4.03$ Å; $c = 6.08$ Å; $\beta = 95.2°$; $V = 187.4$ Å^3	45.5
26	+	+		+	$a = 8.84$ Å; $b = 3.34$ Å; $c = 3.03$ Å; $\beta = 110.7°$; $V = 83.7$ Å^3	68.7

 * "Reliability" criterion of the structure.
** The fcc cell parameters are stable in all specimens.

Table 2. X-ray diffraction characteristics of the crystalline structures

θ, deg	d, Å	hkl	θ, deg	d, Å	hkl
Specimen 5, cubical			Specimen 23, monoclinic		
16.28	2.458	111	6.02	7.35	100
21.22	2.130	200	8.94	4.96	001
30.77	1.507	220	10.46	4.26	−101
36.90	1.284	311	14.64	3.050	−201
38.81	1.230	222	15.64	2.855	201
46.37	1.065	400	15.97	2.802	110
Specimen 3, monoclinic			18.11	2.480	002
13.90	3.210	110	19.52	2.300	102
15.95	2.805	020	23.68	1.920	012
16.19	2.652	021	24.20	1.881	−112
17.84	2.516	102	30.56	1.516	020
19.51	2.308	022	Specimen 24, monoclinic		
24.35	1.870	030	12.62	3.830	200
26.73	1.714	211	13.30	3.351	011
27.19	1.687	130	14.75	3.028	002
27.76	1.657	−105	15.39	2.905	−102
28.61	1.610	202	17.33	2.588	−211
34.16	1.373	−231	18.25	2.462	211
Specimen 8, monoclinic			23.80	1.910	103
14.98	2.982	200	30.51	1.517	−501
16.64	2.693	101	Specimen 26, monoclinic		
17.70	2.535	120	10.75	4.135	200
20.99	2.152	021	13.35	3.34	010
22.19	2.041	220	14.74	3.030	−101
26.68	1.717	−102	15.67	2.854	−201
27.30	1.681	002	18.28	2.457	−301
28.47	1.617	−131	26.17	1.748	−411
30.95	1.499	−231	26.97	1.700	301
31.39	1.480	112	31.20	1.488	−102
			43.84	1.113	030
			44.29	1.105	−801

Thus, the crystalline forms of carbon discussed in this study are new and have not yet been described. The investigation shows that a developing technology based on a dc plasmatron with a supersonic Laval nozzle will make it possible to obtain numerous disperse crystalline carbon materials from hydrocarbons of virtually any series. This will be a great advance in the physics, chemistry, and crystal chemistry of carbon.

REFERENCES

1. Yu. A. Moiseev, Candidate's Dissertation (Inst. Org. Katal. Élektrokhim. Akad. Nauk Kaz. SSR, Alma-Ata, 1986), p. 22.
2. Yu. A. Moiseev, Yu. M. Korolev, V. T. Popov, and V. F. Fedorov, in *Abstracts of the 1st All-Russian Conference on Physics and Chemistry of Ultra-Disperse Systems, Zvenigorod, 1984*, pp. 112–113.
3. Yu. M. Korolev, Dokl. Akad. Nauk **382**, 221 (2002).
4. V. E. Strel'nitskiĭ, V. G. Padalka, and S. I. Vakula, Zh. Tekh. Fiz. **48**, 377 (1978) [Sov. Phys. Tech. Phys. **23**, 222 (1978)].
5. N. N. Matyushenko, V. E. Strel'nitskiĭ, and V. A. Gusev, Kristallografiya **26**, 484 (1981) [Sov. Phys. Crystallogr. **26**, 274 (1981)].
6. V. V. Kozlov, Yu. M. Korolev, and G. P. Karpacheva, Vysokomol. Soedin., Ser. A **41**, 836 (1999).

Translated by Yu. Vishnyakov

=========== **PHYSICS** ===========

Phase Diagrams for an Associated Solution

K. Yu. Shunyaev*, Academician N. A. Vatolin, and V. L. Lisin**

Received July 15, 2003

The model of an ideal associated solution is widely used in current practice for calculating the thermodynamic characteristics of liquid multicomponent systems [1–3]. Over the course of many years, we developed a version of the associated-solution model allowing us to take into account the existence of associates of various compositions, sizes, and shapes [4–7]. It was shown that the model parameters could be estimated from the melting points of individual substances by calculating the energy of an associate in the pair nearest neighbor approximation under the assumption that the infinite associate was a crystal. In addition, such an approach enables us to calculate not only the thermodynamic mixing characteristics, but also the phase diagrams for solutions. It turned out that a quite realistic hierarchy of phase diagrams can be obtained for systems that are mutually soluble only in the liquid phase and are not soluble in the solid phase. This pertains to eutectic systems and to systems that form a stable solid compound. We established the determining role of associates composed of identical atoms (self-associates) for the properties of simple eutectics. Further development of the model enabled us to include into investigation associates with arbitrary stoichiometry [8]. In this case, the problem is solved with a single fitting parameter such as the exchange energy for a regular solution [9]. Inclusion of associates arbitrary stoichiometry into investigation makes it possible to describe various concentration dependences of the thermodynamic mixing characteristics for liquid alloys and to expand the range of systems to which this model is applicable. This primarily pertains to alloys with unlimited solubility near the melting point in the solid and liquid phases.

We consider the A_cB_{1-c} binary system, whose components form a solution with full mutual dissolution in both the liquid and solid phases. Let the solution in the liquid phase be the ideal solution of the $A_n(i)$, $B_n(j)$, and $A_nB_m(i, j, q)$ associates. Here, n and m are the number of the corresponding atoms in the complex and i, j, and q are the numbers of the nearest neighbor pairs AA, BB, and AB, respectively. If the energy of the complex is determined by the sum of energies of the nearest neighbor pairs and only configurational contributions to the entropy are taken into account, the mole fractions of the complexes are interrelated as [4, 5, 8]

$$x_{A_{n,i}} = K_{A_{n,i}} x_{A_1}^n = \exp\left(\frac{\alpha_A i}{kT}\right) x_{A_1}^n = t_A^i x_{A_1}^n,$$

$$x_{B_{n,j}} = K_{B_{n,j}} x_{B_1}^n = \exp\left(\frac{\alpha_B j}{kT}\right) x_{B_1}^n = t_B^j x_{B_1}^n,$$

$$x_{A_nB_m(i, j, q)} = K_{A_nB_m} x_{A_1}^n x_{B_1}^m \tag{1}$$

$$= \exp\left(\frac{\alpha_A i + \alpha_B j + \alpha_{AB} q}{kT}\right) x_{A_1}^n x_{B_1}^m = t_A^i t_B^j t_{AB}^q x_{A_1}^n x_{B_1}^m.$$

Here, $x_{A_{n,i}}$, $x_{B_{n,j}}$, and $x_{A_nB_m}$ are the mole fractions of the , and A_nB_m complexes, respectively; x_{A_1} and x_{B_1} are the mole fractions of A_1 and B_1 solitary atoms, respectively; α_A, α_B, and α_{AB} are the binding energies for the AA, BB, and AB nearest neighbor pairs taken with the opposite sign, respectively; and $K_{A_{n,i}}$, $K_{B_{n,i}}$, and $K_{A_nB_m}$ are the constants of the corresponding equilibria.

The set of the material balance equations for determination of solitary-atom concentrations in solution has the form

$$\sum_n \sum_i x_{A_{n,i}} + \sum_n \sum_j x_{B_{n,j}} + \sum_{n,m} \sum_{i,j,q} x_{A_nB_m} = 1,$$

$$c_A = \frac{\displaystyle\sum_n \sum_i n x_{A_{n,i}} + \sum_{n,m} \sum_{i,j,q} n x_{A_nB_m}}{\displaystyle\sum_n \sum_i n x_{A_{n,i}} + \sum_n \sum_j n x_{B_{n,j}} + \sum_{n,m} \sum_{i,j,q} (n+m) x_{A_nB_m}}. \tag{2}$$

Here, c_A is the mole fraction of the A component. Solving the set of Eqs. (2) and taking into account Eqs. (1),

---
Institute of Metallurgy, Ural Division,
Russian Academy of Sciences,
ul. Amundsena 101, Yekaterinburg, 620016 Russia
 * e-mail: shun@ural.ru
** e-mail: admin@ural.ru

one can find the mole fractions of solitary atoms in the solution in terms of which the thermodynamic characteristics of the system are expressed [10].

To perform these calculations, it is necessary to know the α_A, α_B, and α_{AB} energy parameters, as well as the number of various nearest neighbor pairs in the associates. The α_A and α_B energy parameters can be estimated from the melting points of the pure components [4, 5]. In this case, only the α_{AB} parameter is variable. The total number of pairs in an associate can be calculated under the assumption that the local structure of the corresponding crystal is conserved in the liquid phase [4, 5]. However, this is insufficient for performing summation in Eqs. (2) because it is also necessary to know the distribution of these pairs over the types (AA, BB, and AB). This difficulty can be resolved by

assuming that the associate has the shape of a closed linear chain. In this case, the summation in Eqs. (2) can be performed analytically and the set of Eqs. (2) takes the form

$$
\begin{aligned}
& x_{A_1} + t_A x_{A_1}^2 + S_{1A} + x_{B_1} + t_B x_{B_1}^2 \\
& \quad + S_{1B} + x_{A_1} x_{B_1} t_{AB} + S_{1AB} = 1, \\
& x_{A_1} + 2 t_A x_{A_1}^2 + S_{2A} + x_{A_1} x_{B_1} t_{AB} + S_{2AAB} \\
& \quad = c(x_{A_1} + 2 t_A x_{A_1}^2 + S_{2A} + x_{B_1} + 2 t_B x_{B_1}^2 \\
& \quad + S_{2B} + 2 x_{A_1} x_{B_1} t_{AB} + S_{2AAB} + S_{2AAB}),
\end{aligned} \tag{3}
$$

where

$$
S_{1A} = \frac{x_{A_1}^3 t_A^3}{1 - x_{A_1} t_A}, \quad S_{1B} = \frac{x_{B_1}^3 t_B^3}{1 - x_{B_1} t_B}, \quad S_{2A} = \frac{x_{A_1}^3 t_A^3 (3 - 2 x_{A_1} t_A)}{(1 - x_{A_1} t_A)^2}, \quad S_{2B} = \frac{x_{B_1}^3 t_B^3 (3 - 2 x_{B_1} t_B)}{(1 - x_{B_1} t_B)^2},
$$

$$
S_{1AB} = \frac{x_{A_1} x_{B_1} t_{AB}^2 \left(x_{A_1} t_A + x_{B_1} t_B - x_{A_1} x_{B_1} t_A t_B + x_{A_1} x_{B_1} \dfrac{t_{AB}^2}{1 - x_{A_1} x_{B_1} t_{AB}^2} \right)}{(1 - x_{A_1} t_A)(1 - x_{B_1} t_B)},
$$

$$
S_{2AAB} = \frac{x_{A_1} x_{B_1} t_{AB}^2 \left[x_{A_1} t_A (2 - x_{A_1} t_A)(1 - x_{B_1} t_B) + x_{B_1} t_B + \dfrac{x_{A_1} x_{B_1} t_{AB}^2 (1 - x_{A_1} t_A)}{(1 - x_{A_1} x_{B_1} t_{AB}^2)^2} + \dfrac{x_{A_1} x_{B_1} t_{AB}^2}{1 - x_{A_1} x_{B_1} t_{AB}^2} \right]}{(1 - x_{A_1} t_A)^2 (1 - x_{B_1} t_B)},
$$

$$
S_{2ABB} = \frac{x_{A_1} x_{B_1} t_{AB}^2 \left[x_{B_1} t_B (2 - x_{B_1} t_B)(1 - x_{A_1} t_A) + x_{A_1} t_A + \dfrac{x_{A_1} x_{B_1} t_{AB}^2 (1 - x_{B_1} t_B)}{(1 - x_{A_1} x_{B_1} t_{AB}^2)^2} + \dfrac{x_{A_1} x_{B_1} t_{AB}^2}{1 - x_{A_1} x_{B_1} t_{AB}^2} \right]}{(1 - x_{A_1} t_A)(1 - x_{B_1} t_B)^2}.
$$

We emphasize that the linear chain structure of associates is not our idea of the possible structure of associates and is only an approximation for simplifying the calculations. Such a simplification enables us to easily perform the summation in Eqs. (2) and to derive the set of balance equations in the form of Eqs. (3). This set can be readily solved numerically. In this case, according to the analysis carried out, for instance, in [11], the loss in accuracy of the calculated properties is no more than 10%. The behavior of the thermodynamic characteristics for mixing binary liquid solutions was ana-

lyzed in this model in [8]. This study is devoted to investigating the possibility of calculating phase diagrams.

In [5], we showed that the equilibrium conditions

$$
\frac{-\alpha_A z}{2} = R T_A \ln x_{A_{10}}, \quad \frac{-\alpha_B z}{2} = R T_B \ln x_{B_{10}} \tag{4}
$$

at the melting points of the components made it possible to calculate the α_A and α_B energy parameters (T_A

and T_B are the melting points of the A and B components, respectively, and $x_{A_{10}}$ and $x_{B_{10}}$ are the mole fractions of solitary atoms in the melts of the corresponding components).

We consider only the case where a solid solution is regular and assume that the exchange energy does not change in the process of melting. In this case, it turns out to be the only parameter of the model. We denote

$$W = 2\alpha_{AB} - \alpha_A - \alpha_B. \tag{5}$$

The chemical potentials of mixing the regular-solution components [9] are as follows:

$$
\begin{aligned}
\mu_A &= \mu_{A_0} + RT\ln c_A - (1 - c_A)^2 \frac{zW}{2}, \\
\mu_B &= \mu_{B_0} + RT\ln(1 - c_A) - c_A^2 \frac{zW}{2},
\end{aligned}
\tag{6}
$$

where z is the coordination number. The equality of chemical potentials of the components in the solid and liquid phases is represented in the form of the set of equations

$$
\begin{aligned}
RT\ln x_{A_1}(c_A) &= -\frac{\alpha_A z}{2} + RT\ln C_A - (1 - C_A)^2 \frac{zW}{2}, \\
RT\ln x_{B_1}(c_A) &= -\frac{\alpha_B z}{2} + RT\ln(1 - C_A) - C_A^2 \frac{zW}{2},
\end{aligned}
\tag{7}
$$

where c_A and C_A are the mole fractions of the A component on the liquidus and solidus lines at the temperature under consideration. Solving this set together with balance equations (3), one can calculate the position of the liquidus and solidus lines for a given parameter W and temperature T.

Figure 1 shows the possible types of phase diagrams for various exchange energies. The components were assumed to have the melting points equal to 700 and 1000 K and to form the fcc solid solution. It is seen that the model with only one parameter makes it possible to obtain various phase diagrams including the eutectic and "cigar-type" diagrams and the diagrams with the upper and lower azeotropic points. All these types of diagrams can be realized when the exchange-energy sign provides positive mixing heat in both the solid and liquid phases. When deviations of mixing heat from the ideal value are negative, only the diagrams with the upper azeotropic point are realized. Such a situation is often met in practice. Eutectic systems usually have positive deviations of thermodynamic mixing characteristics from the ideal values [12]. Systems with the lower azeotropic point (e.g., K–Rb and Cs–K), as well as systems with the cigar-type diagram (Bi–Sb), can also exhibit positive deviations from ideal systems [12].
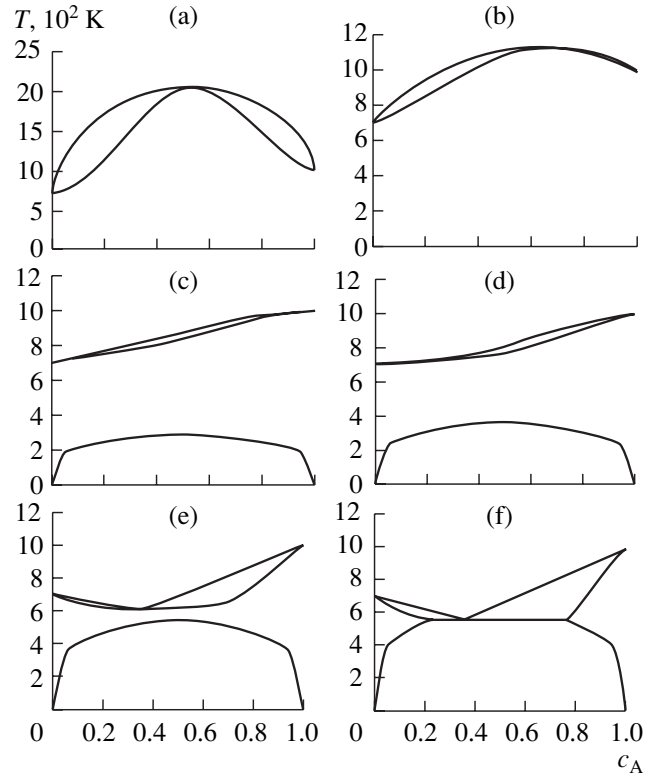
Fig. 1. Phase diagrams for a regular solution for the exchange energy $W =$ (a) 3000, (b) 0, (c) –800, (d) –1000, (e) –1500, and (f) –1700 J/mol.

Certainly, the real relationship between a phase-diagram type and concentration dependences of the thermodynamic mixing characteristics is much more diversified. We note that the analysis performed by D.S. Kamenetskaya (see [13]) for phase diagrams of solutions that are regular in both the solid and liquid phases and have different exchange energies reveals a much poorer picture. In this case, the four variable parameters provide only the cigar-type diagram and the diagram with the azeotropic point.

ACKNOWLEDGMENTS

REFERENCES

1. K. Wasai and K. Mukai, J. Inst. Met. Jpn. **46**, 266 (1982).

2. F. Sommer, Z. Metallkd. **73** (2), 72 (1982).

3. N. E. Shelkova, A. I. Zaĭtsev, and B. M. Mogutnov, Rasplavy, No. 3, 35 (1999).

4. K. Yu. Shunyaev and N. A. Vatolin, Dokl. Akad. Nauk **332**, 167 (1993) [Phys. Dokl. **38**, 391 (1993)].

5. K. Yu. Shunyaev and N. A. Vatolin, Metally, No. 5, 96 (1995).

6. K. Yu. Shunyaev, N. C. Tkachev, and N. A. Vatolin, Thermochim. Acta **314**, 299 (1998).

7. K. Yu. Shunyaev and V. L. Lisin, J. Therm. Anal. Calorimetry **60**, 851 (2000).

8. K. Yu. Shunyaev, N. A. Vatolin, and V. L. Lisin, Dokl. Akad. Nauk **386**, 190 (2002) [Dokl. Phys. **47**, 657 (2002)].

9. V. A. Kozheurov, *Statistical Thermodynamics* (Metallurgiya, Moscow, 1975).

10. I. Prigogine and R. Defay, *Chemical Thermodynamics* (Longmans Green, London, 1954; Nauka, Novosibirsk, 1966).

11. K. Yu. Shunyaev, N. K. Tkachev, and A. N. Men', Rasplavy **2** (5), 11 (1988).

12. R. Hultgren, P. Desai, D. Hawkins, M. Glieser, and K. Kelley, *Selected Values of the Thermodynamic Properties of Binary Alloys* (ASM, Ohio, 1973).

13. Yu. I. Paskal', *Thermodynamic Analysis of Binary Phase Diagrams* (Tomsk. Gos. Univ., Tomsk, 1979).

Translated by V. Bukhanov

=========== **PHYSICS** ===========

On the Mechanism of Formation of Incipient-Phase Nuclei in the Strong-Metastability Region

V. G. Baĭdakov

Presented by Academician V.P. Skripov June 30, 2003

Received July 11, 2003

The conventional nucleation theory describes evolution of incipient-phase fragments as a random sequence of events characterized by the association and consequent dissociation of separate molecules [1, 2]. This conception of the nucleation mechanism, known as the Szilard scheme, was introduced by Farkas [3]. The Szilard scheme was first used to describe the condensation of supersaturated vapor. In this case, it seems evident that the nucleation is the result of elementary acts of evaporation and condensation. Such a nucleation mechanism seems to be adequate for superheated liquids in a weak-metastability region at temperatures not far from the critical temperature. However, for both cavitation in liquids under large tension and tensile fracture of crystals, this mechanism is less evident. In this case, the originating cavities serve as critical nuclei and use of the conventional scheme requires introducing the concept of a virtual particle–hole pair.

Together with the Gibbs thermodynamic considerations [4], the Szilard scheme leads to the conception of homogeneous nucleation as a diffusion process of growing an incipient-phase nucleus in the field of thermodynamic forces. The characteristic size of incipient-phase nuclei serves as a diffusion (the most slowly relaxing) variable. In this case, the nucleus size distribution function $f(R, t)$ satisfies the equation [2]

$$\frac{\partial f(R, t)}{\partial t} = \frac{\partial}{\partial R}\left\{ D(R)\left[\frac{\partial}{\partial R} + \frac{1}{kT}\frac{dW}{dR} \right] \right\} f(R, t), \quad (1)$$

where $D(R)$ is the diffusion coefficient for incipient-phase nuclei, and $W(R)$ is the potential nucleation barrier.

In order to adequately describe the nucleation by Eq. (1), it is necessary and sufficient that the characteristic time τ_* of passage through the nucleation barrier

for incipient-phase fragments be much greater than the relaxation time τ_γ related to the fragment–medium interaction dynamics, i.e., $\tau_* \gg \tau_\gamma$ (in the regime of large friction forces). Such a regime is equivalent to ignoring the inertia of a nucleus. The growth rate of fragments relaxes very fast, and their diffusion through the potential barrier ensures the equilibrium of the fragments whose radii are smaller than the critical radius R_*.

The traditional scenario for the formation of an incipient-phase nucleus is most evident but not the sole possibility. If a system is so strongly supersaturated to be in the vicinity of a spinodal (strong-metastability region), then no sequence of events of molecular association and dissociation can precede the origination of a nucleus. In this case, nucleation can arise as a result of cooperative processes. The possibility of such a mechanism was first pointed out by Skripov [5], who supposed that "if a local extension due to density fluctuations in a liquid attains a value sufficiently large for the volume element to overcome the stability boundary (spinodal), then, at the next moment of time, liquid disintegration will take place and a bubble will originate."

In the present paper, we consider this aspect of nucleation on the basis of our computer simulation of nucleation in a liquid under tension in the vicinity of the spinodal. The principal characteristics of the model and the results obtained were discussed in [6]. The system under investigation contains 2048 Lennard-Jones particles. The calculations were performed by the molecular-dynamics methods for the reduced temperature $T^* = 0.70$. Hereinafter, the intermolecular-interaction parameters, the Boltzmann constant, and the particle mass are taken as scale parameters. The region of states in which the disintegration of a homogeneous liquid under tension proceeds via stages of nucleation and nucleus growth was determined in [7]. The system under consideration was brought to the equilibrium state close to the spontaneous-cavitation region boundary so that the metastable-phase lifetime significantly exceeded the characteristic computer-simulation time. Then, we scaled all particle coordinates and cell sizes in order to diminish the particle density in the system

Institute of Thermal Physics, Ural Division,
Russian Academy of Sciences,
ul. Amundsena 106, Yekaterinburg, 620016 Russia
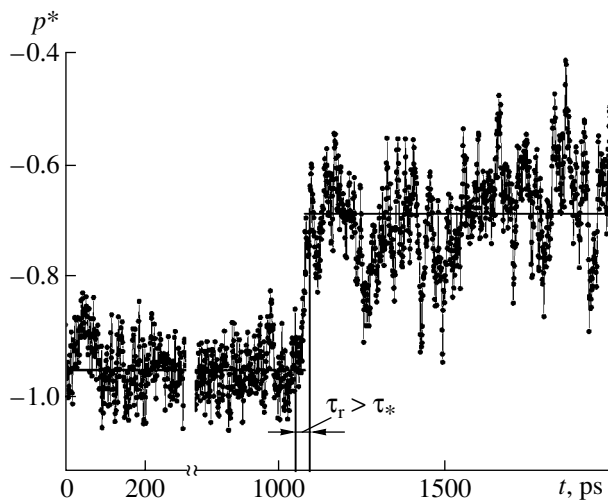*e-mail: bai@itp.uran.ru*

Fig. 1. Instantaneous pressure in a metastable Lennard-Jones system for $T^* = 0.7$ and $\rho^* = 0.7275$.

Fig. 2. Work of incipient phase formation in a system with a constant particle number, volume, and energy.

down to the value $\rho^* = 0.7275$. Next, by registering the pressure jump, we fixed the time for the origination of a stable incipient-phase nucleus. Simultaneously, a special program analyzed the configuration of the particles in the system and registered the presence of incipient-phase fragments and their characteristic sizes. The pressure averaged over time intervals of 1 ps is shown as a function of time in Fig. 1 for a state close to the spinodal. The left section of the curve characterized by lower pressures corresponds to a homogeneous metastable state. Both the number of particles and their sizes are bounded, and the model system is closed. Therefore, after a critical nucleus has originated, the system passes to an equilibrium two-phase state with the liquid containing a stable vapor cavity with the characteristic size R_0 (Fig. 2). The cavity formation is accompanied by a rise of the effective pressure in the system. After averaging 72 realizations of the nucleation process, we have found that the characteristic time of the cavity size to pass through the critical value R_* and to attain the value R_0 is equal to $\tau_r \simeq 25$ ps. This time greatly exceeds the time τ_* of passage of incipient-phase fragments through the critical region of the potential barrier; the latter time cannot be found by the computer simulation. The time τ_r was taken as an upper bound for the value of τ_*.

The characteristic time τ_γ can be estimated according to the correlation time of the random process in an early stage of nucleation. The pressure correlation function is shown in Fig. 2; whence it is seen that $\tau_\gamma \simeq \tau_c \simeq 20$ ps and, therefore, $\tau_r \simeq \tau_\gamma$. This testifies to the fact that nuclei are formed in the regime of intermediate or even weak friction forces ($\tau_* \gg \tau_\gamma$) rather than in the strong-friction regime ($\tau_* \ll \tau_\gamma$), as is postulated in the conventional nucleation theory. Visualization of the
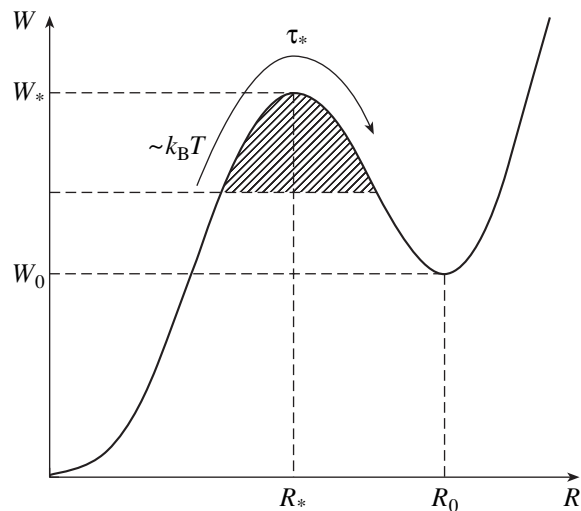
origination and growth of incipient-phase fragments on the computer display screen has shown no processes that could be associated with the Szilard scheme. The simulations most likely prove that the nucleation is a result of collective molecular rearrangements.

We now estimate the characteristic times of the processes under consideration assuming that the nucleation is initiated by the decay of labile pieces formed as a result of chaotic thermal motion. Following from Zel'dovich and Todes [8], we assume that in a one-component system the decay rate of a labile piece is determined only by the heat exchange between expanding and contracting volume elements. In this case, the decrement of rise of density inhomogeneities (the quantity inversely proportional to τ_γ) is determined by the thermal diffusivity α of the medium. A perturbation is unstable if its wavelength is longer than a certain critical value λ_c. The value of λ_c is related to the isothermal compressibility: $\lambda_c \sim |\beta_T|^{1/2}$ [9]. When a labile piece decays, the origination of a nucleus is possible provided that $\lambda_c \geq R_*$. In the linear approximation, $\tau_\gamma \sim \dfrac{\lambda_c^2}{a}$. Near the spinodal, $\beta_T \sim (\rho - \rho_{sp})^{-1}$. If the thermal conductivity is finite on the spinodal, then $a \sim (\rho - \rho_{sp})$ and $\tau_\gamma \sim (\rho - \rho_{sp})^{-2}$. For a quadratic potential barrier, the time τ_* can be expressed in terms of the effective mass of a nucleus and the surface tension. In this case, it weakly depends on the distance to the spinodal. Therefore, in the vicinity of the spinodal, the condition $\tau_\gamma \gg \tau_*$ can be satisfied and corresponds to the nucleation in the weak-friction regime. In this case, the energy of an incipient-phase fragment, which is the most slowly varying variable, serves as the diffusion variable rather than the fragment size [10]. If the energy released in the decay of a labile piece is insufficient for a viable incip-

ient-phase fragment to be formed, then the inhomogeneity that has originated disperses. During the subsequent fluctuation origination of a labile piece and its decay, the system attempts to overcome the barrier with its new energy content. Thus, under weak friction the kinetics of the process is governed by the energy diffusion from the potential well up to the value W_* equal to the barrier height. In this case, the heat equilibrium for subcritical fragments is absent, and the kinetic equation describing the nucleation as energy diffusion follows from the Fokker–Planck equation. This equation should be transformed to pass from the variables corresponding to the coordinate R and velocity $\dot{R}$ to the total energy

$$E = \frac{m_{\mathrm{eff}}\dot{R}^2}{2} + W \qquad (2)$$

or the action

$$I = \oint 2m_{\mathrm{eff}}[E - W(R)]^{1/2}dR. \qquad (3)$$

Here, m_{eff} is the effective mass of an incipient-phase fragment. The kinetic equation in the action has the form [10]

$$\frac{\partial f(R,t)}{\partial t} = \frac{\partial}{\partial I}\left\{D(I)\left[\frac{\partial}{\partial I} + \frac{1}{kT}\frac{dE}{dI}\right]\right\}f(I,t), \qquad (4)$$

where $D(I)$ is the diffusion coefficient for the coordinate I, and $f(I, t)$ is the action distribution function for incipient-phase fragments.

In the steady-state case, the flux J of nuclei is independent of I and determines the number of viable nuclei formed within a unit volume of the metastable phase per unit time, i.e., the nucleation rate. We then integrate Eq. (4) between the points I_0 (at which the excess energy of the system does not exceed kT) and $I_*(W_*)$. We also assume that the nucleus leaves the well freely provided that its energy attains the value W_*. As a result, we arrive at

$$J = C\left[\int_{I_0}^{I_*}\frac{1}{D}\exp\frac{E}{kT}dI\right]^{-1}, \qquad (5)$$

where C is the normalization constant. For $\dfrac{W_*}{kT} \gg 1$ and
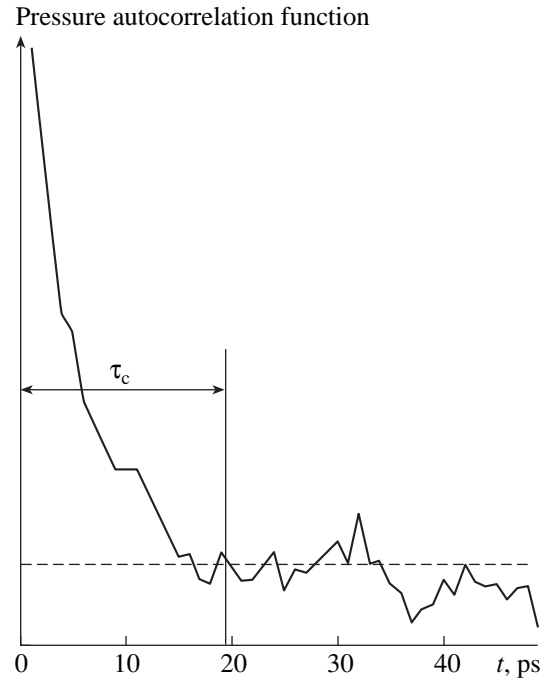
Pressure autocorrelation function

Fig. 3. Pressure autocorrelation function in a metastable system for $T^* = 0.7$ and $\rho^* = 0.7275$.

$I_0 \ll I_*$, the asymptotic estimation of integral (5) yields

$$J = \frac{C}{kT}\left(\frac{dE}{dI}\right)_0 D(I_*)\exp\left(-\frac{W_*}{kT}\right). \qquad (6)$$

In the conventional theory of homogeneous nucleation, the expression for the steady-state nucleation rate has a form similar to Eq. (6). Differences concern the magnitude of the preexponential factor and its temperature dependence. The problem of determining the diffusion coefficient $D(I_*)$ in the weak-friction regime is more complicated because the distribution of subcritical fragments is nonequilibrium. This does not allow us to use the method developed by Zel'dovich [2] in the conventional nucleation theory.

In contrast to the Szilard scheme of separate events, cooperative nucleation processes can involve no labile phase. Local inhomogeneities having properties of a competing phase originate as fluctuations in the process of chaotic thermal motion. This process can also occur in the weak-metastability region in an early stage of nucleation. The further growth of near-critical nuclei follows the conventional scheme. In this case, nuclei pass slowly through the critical region of the potential barrier, Eq. (1) is applicable, and the experiments are closely consistent with the conventional nucleation theory [11].

REFERENCES

1. M. Vollmer, *Kinetik der Phasenbildung* (Steinkopff, Dresden, 1939; Nauka, Moscow, 1986). Translated from German.

2. Ya. B. Zel'dovich, Zh. Éksp. Teor. Fiz. **12**, 525 (1942).

3. L. Farkas, Z. Phys. Chem. (Munich) **125**, 236 (1927).

4. J. W. Gibbs, *Thermodynamics. Statistical Mechanics* (Yale Univ. Press, New Haven, 1948; Nauka, Moscow, 1982).

5. V. P. Skripov, *Metastable Liquid* (Nauka, Moscow, 1972).

6. V. G. Baĭdakov and S. P. Protsenko, Dokl. Akad. Nauk **394** (2004, in press) [Dokl. Phys. (2004, in press)].

7. V. G. Baĭdakov and S. P. Protsenko, Teplofiz. Vys. Temp. **41**, 231 (2003).

8. Ya. B. Zel'dovich and O. M. Todes, Zh. Éksp. Teor. Fiz. **10**, 1441 (1940).

9. V. P. Skripov and A. V. Skripov, Usp. Fiz. Nauk **128**, 193 (1979) [Sov. Phys. Usp. **22**, 389 (1979)].

10. N. A. Kramers, Physica **7**, 284 (1940).

11. V. G. Baĭdakov, V. P. Skripov, and A. M. Kaverin, Zh. Éksp. Teor. Fiz. **65**, 1126 (1973) [Sov. Phys. JETP **38**, 557 (1974)].

Translated by V. Chechin

===== **PHYSICS** =====

Ion-Emission Properties of a Plasma
in a Gaseous-Ion Source with a Plasma Cathode

N. V. Gavrilov* and A. S. Kamenetskikh

Presented by Academician G.A. Mesyats July 4, 2003

Received July 18, 2003

1. A promising scheme of sources of broad gaseous-ion beams is a two-stage electrode system involving a plasma cathode, which has a long service life, and a plasma generator with desired ion-emission characteristics such as plasma-emitter size and shape, emission-current density, and an acceptable level of emission nonuniformity. Nowadays, there are ion sources with plasma cathodes based on microwave and rf discharges, where a chamber placed in a multipole magnetic field is used in the second stage [1, 2]. Cold-cathode ion sources, where ions are extracted from the anode plasma of a glow discharge in a magnetic field, have also been designed [3]. A feature of the glow-discharge ion source described in [4] is the use of a grid separating the cathode and anode stages and the absence of a magnetic field in the second stage consisting of a hollow cathode and a thin-rod anode. Between these electrodes, gas ionization induced by injected electrons gives rise to a non-self-sustained glow discharge under low gas pressures (as low as 3×10^{-3} Pa). However, since the ion current is distributed over the whole surface of the second-stage cathode, the current of ions extracted from the plasma amounts to approximately 4% of the injected-electron current.

The purpose of this study is to improve the characteristics of glow-discharge ion sources by combining a plasma cathode with a grid fixation of an emitting plasma surface and an anode chamber with a peripheral multipole magnetic field. Such a system ensures independent control of the current and energy of primary electrons, their confinement, the energy relaxation and generation of the uniform emitting plasma, and the extraction of most of the created ions from the plasma. In this study, we investigate how the current and energy of injected electrons, as well as the working-gas pressure, affect the ion current. The conditions providing an increase in the ion current up to values comparable with the plasma-cathode electron current were determined

and, for the first time, realized in a cold-cathode ion source.

2. To create the plasma cathode, we used a high-current vacuum mode of a hollow-cathode glow discharge with an anode-to-cathode area ratio of $\dfrac{S_a}{S_c} \sim \left(\dfrac{m_e}{M_i}\right)^{1/2}$, which provided a low rate of fast-electron losses [5]. Here, m_e and M_i are the electron and ion masses, respectively. The plasma-cathode electrode system (Fig. 1) is similar to that used in [4]. The glow-discharge grid anode (or the plasma-cathode emitter grid) facing the output aperture of the hollow cathode is electrically connected with the screen grid of a beam-forming system. The emitter and screen grids are installed on the ends of the second-stage hollow anode. Linear rows of permanent magnets with alternating polarity that are arranged on the anode surface form the multipole mag-
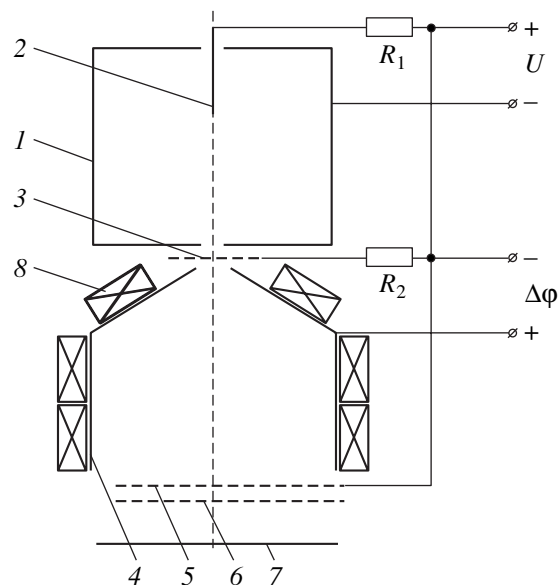

Fig. 1. Layout of the ion source: (*1*) hollow cathode, (*2*) ignition electrode, (*3*) emitter grid, (*4*) anode, (*5*) screen and (*6*) accelerating ion-optical electrodes, (*7*) beam collector, (*8*) permanent magnets, U is the output voltage of the glow-discharge power supply, and $\Delta\varphi$ is the potential difference between the grids and the anode.

Institute of Electrophysics, Ural Division,
Russian Academy of Sciences,
ul. Amundsena 106, Yekaterinburg, 620016 Russia
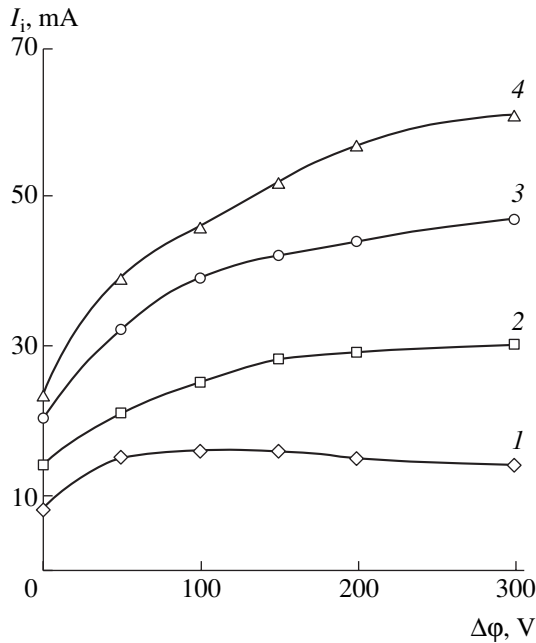* *e-mail: gavrilov@iep.uran.ru*

Fig. 2. Ion-beam current vs. the potential difference between the anode and the grids. The plasma-cathode current I_e = 200 mA. The argon pressure p = (*1*) 1.5×10^{-2}, (*2*) 1.9×10^{-2}, (*3*) 4.9×10^{-2}, and (*4*) 6.8×10^{-2} Pa.

netic field [6] with an induction of 0.09 T at the poles. The glow-discharge ignition results in the appearance of an electron current in the circuits of the emitter and screen grids. The application of a potential difference $\Delta\varphi$ between the grids and the anode has no effect on the current–voltage characteristic of the glow discharge, whose maintaining voltage amounted to 360–480 V depending on the discharge current (0.2–1 A) and argon flow (10–50 cm^3/s) leaked in the cathode hollow. An increase in $\Delta\varphi$ changes the current polarity in the screen-grid circuit, reduces the electron current to the anode grid down to several percent of the hollow-cathode current, and increases the anode current up to about the sum of the hollow-cathode and ion currents to the screen grid. The voltage $\Delta\varphi$ is predominantly localized across the space-charge layer near the grids, and the voltage drop across the layer and the plasma-cathode current can be independently controlled over a wide range.

The voltage drop across the space-charge layer, which determines the injected-electron energy, may greatly exceed the voltage across the double electric layer in constricted discharges [7], which is determined by both the gas conditions in the constriction and the discharge current and usually amounts to 20–50 V. This fact increases the ionizing effect of fast electrons but also increases the grid sputtering rate due to an increase in ion energy. For the content of metal ions in the plasma to be less than 1%, the potential difference $\Delta\varphi$ in the experiments was lower than 300 V.

Figure 2 shows the 3-keV ion current vs. the potential difference $\Delta\varphi$. We used a two-electrode ion-optical

system with an area of 50 cm^2 and an identical aperture diameter of 5 mm in the screen and accelerating grids. For low plasma-cathode currents, an increase in the ion current up to 25–30% of the plasma-cathode current is reached by increasing both the gas pressure and potential difference $\Delta\varphi$. These dependences change with increasing electron current. To exclude ion-optical effects and to expand the variation range of the plasma-cathode current, we measured the ion current from the plasma to a plate installed instead of the screen grid (Fig. 3). The measurement of the radial profiles of the ion-current density in the plate plane showed that a nearly homogeneous (10%) plasma is generated in all discharge modes in the region free of the magnetic field (~80 mm). An increase in the hollow-cathode output aperture from 5 to 20 mm approximately doubles the ion current and negligibly increases the discharge voltage (~50 V).

When discharge glows to the anode through the cathode aperture without the emitter grid, the current of ions extracted from the anode plasma of the contracted discharge turned out to be one eighth to half of the ion current extracted from the system with the plasma-cathode surface fixed by a grid for the same glow-discharge currents. The ion current increased with decreasing gas pressure.

3. If the plasma is generated only as a result of collisions of fast electrons with neutrals and neutral species, the number of ions generated by a fast electron depends on its initial energy and lifetime in the plasma. According to the model considered in [8–10], the electron-to-ion current ratio is described in this case by the expression

$$\frac{I_e}{I_i} \sim \alpha \left[W + \frac{\lambda_i}{l} \right], \qquad (1)$$

where α is the ratio of the total current of ions generated in the plasma to the current of extracted ions, l is the total electron path in the plasma before its escape to the anode, $\lambda_i = (n_0 \sigma_i)^{-1}$ is the mean ionization path of fast electrons, n_0 is the neutral-particle concentration, and σ_i is the electron-impact ionization cross section. The constant W is determined by the ratio of the total energy losses of an electron in inelastic collisions to the energy spent on gas ionization.

Thus, the ratio $\dfrac{I_e}{I_i}$, which is inversely proportional to the efficiency of ion extraction from the plasma, as a function of inverse gas pressure must be a straight line, whose slope is inversely proportional to the total path or to the electron-confinement time in the plasma, while the point of intersection between the straight line and the ordinate axis determines the ionization efficiency under infinitely high gas pressures.

Contrary to Eq. (1), the plots shown in Fig. 3 are nearly linear only for low currents and pressures. With an increase in the current, the slope of tangents to the
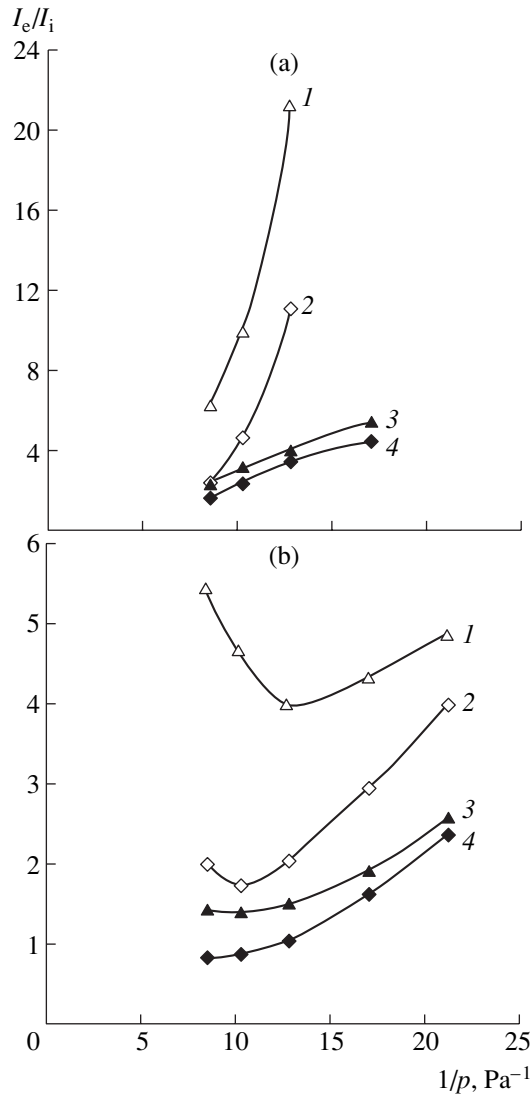
Fig. 3. Ratio of the plasma-cathode current I_e to the current I_i of ions extracted from the plasma vs. the inverse gas (argon) pressure in the ion source for the hollow-cathode output aperture with a diameter of (a) 5 and (b) 20 mm. The potential difference between the anode and the grids $\Delta\varphi =$ (1, 2) 100 and (3, 4) 300 V. The plasma-cathode current $I_e =$ (1, 3) 600 and (2, 4) 200 mA.

curves decreases (Fig. 3a), while the minimum in the plots is displaced towards lower pressures (Fig. 3b). The slope is maximal for the minimum aperture size.

The results obtained can be explained if one takes into consideration the high density and the directivity of the injected-electron flow, which reduces the plasma potential φ_p relative to the anode potential φ_a in the region free of the magnetic field. When the gas pressure increases, the positive anode drop ($\varphi_a - \varphi_p$) decreases, and the plasma potential changes sign at a certain gas pressure. A negative plasma potential rules out the possibility for ions to escape to the anode and, therefore, provides a high efficiency of ion extraction from the

plasma. However, the significant negative plasma potential reduces the energy of injected electrons, which reduces their ionizing effect, and increases the effective width of return lines of the magnetic field on the anode [8], which increases the electron-loss rate.

A positive plasma potential is beneficial to electron confinement. However, it allows the diffusion of plasma ions across the magnetic field to the anode due to collisions of ions with neutral particles under increased gas pressures, which abruptly reduces the current of extracted ions.

Thus, the investigations determined the conditions of the effective emission of ions from the plasma created by electrons injected from a glow discharge and showed that the current density of injected electrons substantially affects the efficiency of ion extraction from the plasma. The extracted-ion current and ion-beam current are increased up to ~0.6 and ~0.3 of the plasma-cathode current, respectively. The cold cathode has a service life of ~10^3 h. The small cathode-aperture size rules out the arrival of sputtered cathode-material atoms in the second stage, and the small potential difference between the second-stage electrodes reduces the cathode-sputtering rate. Both these circumstances provide a minimum contamination of the plasma by metal ions.

REFERENCES

1. Y. Oka, T. Shoji, T. Kuroda, *et al.*, Rev. Sci. Instrum. **61**, 1256 (1990).
2. Y. Hakamata, T. Iga, K. Natsui, and T. Sato, Nucl. Instrum. Methods Phys. Res. B **37–38**, 143 (1989).
3. V. Ya. Martens, S. I. Belyuk, and V. N. Posokhov, Prib. Tekh. Éksp., No. 2, 194 (1992).
4. A. V. Vizir', E. M. Oks, P. M. Shchanin, and G. Yu. Yushkov, Zh. Tekh. Fiz. **67** (6), 28 (1997) [Tech. Phys. **42**, 611 (1997)].
5. A. S. Metel', Zh. Tekh. Fiz. **54**, 241 (1984) [Sov. Phys. Tech. Phys. **29**, 141 (1984)].
6. R. Limpaecher and K. R. MacKenzie, Rev. Sci. Instrum. **44**, 726 (1973).
7. J. Kistemaker, P. K. Rol, and J. Politiek, Nucl. Instrum. Methods **38** (1–2), 1 (1965).
8. A. J. T. Holmes, Rev. Sci. Instrum. **52** (12), 1814 (1981).
9. D. Cope and J. H. Keller, J. Appl. Phys. **56**, 96 (1984).
10. K. N. Leung, R. E. Kribel, A. P. H. Goede, and T. S. Green, Phys. Lett. A **66A**, 112 (1978).

Translated by V. Bukhanov

═══════════ **PHYSICS** ═══════════

Anomalous Tracer Transport in the Stochastic Advection Model

I. L. Dranikov, P. S. Kondratenko*, and L. V. Matveev

Presented by Academician A.M. Dykhne August 11, 2003

Received August 11, 2003

INTRODUCTION

Tracer transport processes in highly disordered media often cannot be described by the classical diffusion equation [1]. Most alternative models (see [2–4]) reduce to fractional differential equations, whose solutions have two distinctive features. These are anomalous behavior of the tracer cloud size at fairly long times ($R \sim t^\gamma$ with $\gamma \neq \frac{1}{2}$) and a slow decrease (power rather than classical Gaussian) in concentration at large distances ($r \gg R$).

We note that, because the difference between the power and Gaussian decreases is immense, the problem of "heavy tails" in the tracer concentration distribution is of exceptional practical importance, for example, for estimating the reliability of radioactive waste repositories, from which even insignificant leakage of a contaminant to vital areas is impermissible. At the same time, we emphasize that the approach based on fractional differential equations is, generally speaking, formally mathematical. For this reason, its conclusions should be checked against particular physical models. One such model is the problem of stochastic advection in a fractal medium with long-range correlations of spatially fluctuating parameters. It has been already studied, under some simplifying assumptions, in [5, 6], where γ was determined and the problem of the concentration profile was considered.

In this study, we analyze this model in general form, including the solution of the problem of tails. The analysis is based on the diagram technique using notions of the scale invariance of a medium.

───────────────

Nuclear Safety Institute, Russian Academy of Sciences, ul. Bol'shaya Tul'skaya 52, Moscow, 113191 Russia
* *e-mail: kondrat@ibrae.ac.ru*

FORMULATION OF THE PROBLEM AND METHOD OF SOLUTION

The stochastic advection model is based on the following equation for the tracer concentration $c(\mathbf{r}, t)$:

$$\frac{\partial c}{\partial t} + \nabla(\mathbf{v} - D\nabla)c = 0, \tag{1}$$

including advection and molecular diffusion processes. For definitiveness, we will consider the problem with an initial tracer distribution (at $t = 0$) in the absence of a source. In the above equation, $\mathbf{v} = \mathbf{v}(\mathbf{r})$ is the velocity of the advective flow and $D(\mathbf{r})$ is the diffusivity. Both quantities are random functions of the coordinates. Assuming the medium to be statistically homogeneous, we represent $\mathbf{v}$ and D in the form of the sums

$$\mathbf{v}(\mathbf{r}) = \mathbf{u} + \mathbf{v}'(\mathbf{r}), \quad D(\mathbf{r}) = \overline{D} + D'(\mathbf{r}), \tag{2}$$

where $\mathbf{u} = \langle \mathbf{v}(\mathbf{r}) \rangle$ and $\overline{D} = \langle D(\mathbf{r}) \rangle$ are the mean values over the realization ensemble, while $\mathbf{v}'(\mathbf{r})$ and $D'(\mathbf{r})$ are the fluctuating parts; i.e., $\langle \mathbf{v}'(\mathbf{r}) \rangle = 0$ and $\langle D'(\mathbf{r}) \rangle = 0$. The velocity field satisfies the continuity equation $\text{div}\,\mathbf{v} = \text{div}\,\mathbf{v}' = 0$.

We assume that the medium has fractal properties, so that correlation functions of random values $\mathbf{v}'$ and D' decrease at large distances as power functions. In particular, the binary correlation function of velocities $K_{ij}^{(2)}(\mathbf{r}_1 - \mathbf{r}_2) \equiv \langle v_i'(\mathbf{r}_1) v_j'(\mathbf{r}_2) \rangle$ at $|\mathbf{r}_1 - \mathbf{r}_2| \gg a$ is such that

$$K_{ii}^{(2)}(\mathbf{r}_1 - \mathbf{r}_2) \simeq V^2 \left(\frac{a}{|\mathbf{r}_1 - \mathbf{r}_2|}\right)^{2h}, \tag{3}$$

where $h > 0$, a is the length parameter of short-range correlations, and V is the velocity fluctuation scale. Similarly, at $|\mathbf{r}_i - \mathbf{r}_j| \gg a$ (for all pairs $\mathbf{r}_i, \mathbf{r}_j$), the n-point correlation function defined by the formula

$$K_{i_1 i_2 \ldots i_n}^{(n)}(\mathbf{r}_1, \mathbf{r}_2, \ldots, \mathbf{r}_n) = \langle v_{i_1}'(\mathbf{r}_1) v_{i_2}'(\mathbf{r}_2) \ldots v_{i_n}'(\mathbf{r}_{i_n}) \rangle,$$

satisfies the equation

$$K^{(n)}_{i_1 i_2 \ldots i_n}(\lambda \mathbf{r}_1, \lambda \mathbf{r}_2, \ldots, \lambda \mathbf{r}_n)$$

$$= \lambda^{-nh} K^{(n)}_{i_1 i_2 \ldots i_n}(\mathbf{r}_1, \mathbf{r}_2, \ldots, \mathbf{r}_n). \tag{4}$$

By analogy with the theory of critical phenomena [7], the parameter h will be called the scaling dimension of the velocity fluctuation $\mathbf{v}'$. Relations similar to Eqs. (3) and (4) are also valid for the correlation functions of diffusivity fluctuations.

Of practical importance is the concentration distribution averaged over the medium realization ensemble $\bar{c}(\mathbf{r}, t) \equiv \langle c(\mathbf{r}, t) \rangle$. It can be related with the initial concentration distribution $c(\mathbf{r}, 0)$ by the formula

$$\bar{c}(\mathbf{r}, t) = \int d\mathbf{r}' \bar{G}(\mathbf{r} - \mathbf{r}', t) c(\mathbf{r}', 0). \tag{5}$$

Here, $\bar{G}(\mathbf{r} - \mathbf{r}', t) \equiv \langle G(\mathbf{r}, \mathbf{r}'; t) \rangle$, where $G(\mathbf{r}, \mathbf{r}'; t)$ is the Green's function satisfying Eq. (1) with the initial condition $G(\mathbf{r}, \mathbf{r}'; 0) = \delta(\mathbf{r} - \mathbf{r}')$. The averaged Green's function $\bar{G}(\mathbf{r} - \mathbf{r}', t)$ is conveniently calculated by the methods of quantum field theory on the basis of the "cross" diagram technique, which was developed in [8] and further used in the theory of transport in disordered media [9].

In the spatial Fourier and temporal Laplace representations, the function $\bar{G}(\mathbf{r} - \mathbf{r}', t)$, in view of Eqs. (1) and (2) and the initial condition $G(\mathbf{r} - \mathbf{r}'; 0) = \delta(\mathbf{r} - \mathbf{r}')$, takes the form

$$\bar{G}\{\mathbf{k}, p\} = \frac{1}{p + i\mathbf{k}\mathbf{u} + \bar{D}k^2 - M(\mathbf{k}, p)}, \tag{6}$$

where $\mathbf{k}$ and p are the Fourier and Laplace variables and $M(\mathbf{k}, p)$ is the polarization operator representing the sum of the irreducible skeleton diagrams [8]

$$\tag{7}$$

Here, horizontal lines correspond to the function $\bar{G}$, crosses represent the perturbation operator $-\mathbf{v}'\nabla + \nabla D'\nabla$, and dashed lines connect the crosses that pertain to one of the cumulants, the expansion in which constitutes the essence of averaging over the realization ensemble. Substitution of Eq. (6) into diagram expansion (7) transforms the latter to an integral equation for the function $M(\mathbf{k}, p)$.

An analysis of this equation on the basis of the structure of expansion (7) and taking scaling relations (3) and (4) into account made it possible to establish the main properties of tracer transport in the stochastic advection model in general form.

RESULTS OF THE ANALYSIS

1. Fluctuations of both the advection rate at a scaling dimension $h > 1$ and the diffusivity at an arbitrary dimension do not change the classical diffusion law and change only the mean value of the diffusivity. The results of the analysis for parameters with a dimension $h \leq 1$ depend on whether the mean advection rate $\mathbf{u}$ is nonzero.

2. At $\mathbf{u} = 0$ and $h < 1$, the inequality $\bar{D}k^2 \ll M(\mathbf{k}, p)$ holds. The polarization operator satisfies the scaling relation $M(\lambda\mathbf{k}, \lambda^{1+h}p) = \lambda^{1+h}M(\mathbf{k}, p)$ and, therefore, can be represented in the form

$$M(\mathbf{k}, p) = Va^h k^{1+h} \varphi(\xi), \tag{8}$$

where $\varphi(\xi)$ is a dimensionless function of the dimensionless self-similar variable $\xi = \dfrac{p}{Va^h k^{1+h}}$ with the following limiting expressions:

$$\varphi(0) = \text{const} \sim 1;$$

$$\varphi(\xi) = \xi \sum_{n=1}^{\infty} b_n \xi^{-\frac{2n}{1+h}} \quad \text{for} \quad \xi \gg 1. \tag{9}$$

In view of Eq. (6), properties (8) and (9) allow us to write the averaged Green's function in the form

$$\bar{G}(\mathbf{r}, t) = (Va^h t)^{-\frac{3}{1+h}} \Phi\left(\frac{r^{1+h}}{Va^h t}\right). \tag{10}$$

Here, the function $\Phi(x)$ is such that $\Phi(0) \sim 1$ and $\Phi(x)|_{x \gg 1} \sim \exp(-Bx^{\frac{1}{1+h}})$, where $B \sim 1$. From Eq. (10), it follows that the size of the tracer localization region at long times is of the order

$$R \sim (Va^h t)^{\frac{1}{1+h}} \tag{11}$$

and, at large distances $(r \gg R)$, the tracer concentration decreases exponentially:

$$\bar{c}(\mathbf{r}, t) \propto \exp\left(-B\frac{r}{(Va^h t)^{\frac{1}{1+h}}}\right). \tag{12}$$

3. At $\mathbf{u} = 0$ and $h = 1$, the tracer localization region at long times has the size

$$R \sim (Vat)^{\frac{1}{2}} \ln^{\frac{1}{4}}\left(\frac{Vt}{a}\right) \tag{13}$$

and, as at $h < 1$, the expansion of the tracer concentration distribution at large distances does not involve power terms.

4. At $\mathbf{u} \neq 0$, under the assumption that $u \ll V$, at times $t \ll t_* \equiv \dfrac{a}{u}\left(\dfrac{V}{u}\right)^{\frac{1}{h}}$, the transport process occurs similarly to the case $\mathbf{u} = 0$. At long times ($t \gg t_*$), the transport features are fundamentally different for the scaling dimensions $h > \dfrac{1}{2}$, $h < \dfrac{1}{2}$, and $h = \dfrac{1}{2}$.

For $\dfrac{1}{2} < h < 1$, the tracer transport obeys the classical diffusion laws, with the effective diffusivity $D_{\text{eff}} \sim u^2 t_*$.

For $h < \dfrac{1}{2}$, an anomalous diffusive transport regime takes place. The averaged Green's function takes the form

$$\overline{G}(\mathbf{r}, t) = \frac{1}{(ut_*)^3}\left(\frac{t_*}{t}\right)^{3(1-h)}\Psi\left(\left(\frac{r'}{ut_*}\right)^{\frac{1}{1-h}}\frac{t_*}{t}\right), \quad (14)$$

where $\mathbf{r}' = \mathbf{r} - \mathbf{u}t$, $\Psi(0) \sim 1$, $\Psi(x)|_{x \gg 1} \sim \exp(-Cx^{1-h})$, and $C \sim 1$. Correspondingly, the size of the tracer localization region at long times is of the order

$$R \sim ut_*\left(\frac{t}{t_*}\right)^{1-h}, \quad (15)$$

while the concentration decreases at $r \gg R$ as

$$\bar{c}(\mathbf{r}, t) \propto \exp\left(-C\frac{r'}{ut_*}\left(\frac{t_*}{t}\right)^{1-h}\right). \quad (16)$$

At the scaling dimension $h = \dfrac{1}{2}$, the size of the tracer localization region at times $t \gg t_*$ is given by the expression

$$R \sim u\left[tt_*\ln\left(\frac{t}{t_*}\right)\right]^{\frac{1}{2}}. \quad (17)$$

CONCLUSIONS

In this study, some fundamental results pertaining to transport processes in highly disordered media are obtained in the stochastic advection model.

The type of the laws governing the process depends appreciably on the scaling dimension of the spatial fluctuations of the advection rate, which is determined by the exponents in the correlation functions. Velocity fluctuations with scaling dimensions $h > 1$, as well as diffusivity fluctuations of any dimension, do not violate the classical diffusion regime.

In a medium where the velocity fluctuation dimension is $h < 1$, at a zero mean advection rate ($\mathbf{u} = 0$), a superdiffusion transport regime with the time dependence $R(t) \propto t^\gamma$, where $\gamma \neq \dfrac{1}{2}$, is realized, as in fractional diffusion models [2]. However, in contrast to the power decrease inherent in those models, in the stochastic advection model the tracer concentration at $r \gg R(t)$ decreases exponentially; i.e., heavy tails are absent.

In our opinion, this difference is not accidental. Being a physical model, the stochastic advection model takes into account that the tracer advection velocity is bounded from above. Therefore, a slow power decrease in concentration at large distances is impossible. Being purely mathematical, the fractional diffusion model disregards the above physical principle (see also [4]).

The conclusions made in this study for the case of a nonzero mean advection rate are qualitatively similar to those obtained for $\mathbf{u} = 0$, though the ranges of transport regimes, as well as the exponents in temporal and spatial functions, are different in this case and the system behaves differently before and after an additional characteristic time.

For both $\mathbf{u} = 0$ and $\mathbf{u} \neq 0$, the boundaries between the transport regimes with respect to the parameter h ($h = 1$ for $\mathbf{u} = 0$ and $h = \dfrac{1}{2}$ for $\mathbf{u} \neq 0$) are peculiar. In these cases, the governing laws are modified by logarithmic factors.

REFERENCES

1. M. B. Isichenko, Rev. Mod. Phys. **64**, 961 (1992).

2. A. Compte, Phys. Rev. E **53**, 4191 (1996).

3. M. M. Meerschaert, D. A. Benson, H.-P. Scheffler, and B. Baeumer, Phys. Rev. E **65**, 041103 (2002).

4. V. Yu. Zaburdaev and K. V. Chukbar, Zh. Éksp. Teor. Fiz. **121**, 299 (2002) [JETP **94**, 252 (2002)].

5. D. L. Koch and J. F. Brady, Phys. Fluids A **1**, 47 (1989).

6. D. L. Koch and J. F. Brady, Phys. Fluids **31**, 965 (1988).

7. A. Z. Patashinskiĭ and V. L. Pokrovskiĭ, *Fluctuation Theory of Phase Transitions* (Nauka, Moscow, 1975; Pergamon Press, Oxford, 1979).

8. A. A. Abrikosov, L. P. Gor'kov, and I. E. Dzyaloshinskiĭ, *Methods of Quantum Field Theory in Statistical Physics* (Fizmatgiz, Moscow, 1962; Prentice-Hall, New York, 1963).

9. Yu. A. Dreĭzin and A. M. Dykhne, Zh. Éksp. Teor. Fiz. **63**, 242 (1972) [Sov. Phys. JETP **36**, 127 (1972)].

Translated by M. Lebedev

===== **PHYSICS** =====

Analytical Expression
of the Kapitza Magnetoresistance Law

N. N. Sirota

Presented by Academician V. V. Osiko September 18, 2003

Received July 17, 2003

In this paper, the analytical expression for the empirical Kapitza law is obtained. The Kohler rule is shown to be a particular case of it. The analysis is performed as applied to quasi-isotropic metals without allowance for quantum and dimensional effects. In the case of equal transverse magnetic-field components, the magnitude of the magnetoresistive effect is shown to be proportional to the longitudinal field component, the proportionality coefficient η depending on the magnetic-field intensity.

A method of production of strong magnetic fields was proposed by Kapitza, who had performed systematic studies of the variation of magnetoresistance of metals as a function of the magnetic-field intensity. The measurements were carried out for both weak and strong (30 T) fields. Based on studying 35 different chemical elements of the periodic system, a general regularity was established for the field dependence of the specific electric resistance of metals, which was called the Kapitza law [1–5].

According to this law, the relative specific electrical resistance $\dfrac{\rho_H}{\rho_0}$ (subscripts H and 0 correspond to the presence and absence of magnetic field, respectively) in weak fields varies proportionally to its intensity squared. In strong magnetic fields, a gradual transition from a quadratic to a linear dependence is observed.

This law has been theoretically and, on the whole, qualitatively substantiated based on the fact that, in the case of a magnetic field imposed on a sample through which an electric current flows, the complication and elongation of trajectories of charge carriers (electrons) take place due to the action of the Lorentz force. This is accompanied by an increase in the resistivity of metal samples [6–10]. However, no definite quantitative confirmation of this empirical law has been obtained.

In 1938, Kohler [11] formulated a rule linking the magnetoresistance with the initial specific resistance.

Moscow State University of Environmental Engineering,
ul. Pryanishnikova 9, Moscow, 127550 Russia

In accordance with this rule, the variation of ρ_H is a function of the ratio $\dfrac{B}{\rho_0}$, i.e., the ratio of the magnetic induction B and the initial specific resistance, the function $f\left(\dfrac{B}{\rho_0}\right)$ being identical for different metals.

In this paper, we derive an exact quantitative expression for the Kapitza law under certain initial conditions, which shows that the Kohler rule is a particular case of this law.

We now restrict our analysis to consideration of quasi-isotropic metals with a closed, e.g., spherical Fermi surface that is not deformed by the action of magnetic field. We also assume that the distribution density for centers of scattering conduction electrons is independent of the external magnetic field. Under these conditions, electrons in metals move chaotically with both thermal velocities and a velocity determined by zero oscillations of the medium. We suggest that, in the case of parallel directions of magnetic field and electric current, the majority of electrons move for a time t in the direction normal to the magnetic field. The fraction of these electrons with respect to all conduction electrons is determined by the quantity β dependent on the magnetic-field intensity. Under the action of both the Lorentz force $\mathbf{F}_H$ and the Coulomb force $\mathbf{F}_e$, the electrons form spiral-shaped trajectories with the averaged length L around the magnetic-field lines shifting along the electric-current lines with a certain translational velocity. The Lorentz force $\mathbf{F}_H$ and the Coulomb force $\mathbf{F}_e$ are normal to each other. The resulting force F acting on conduction electrons and the angle between the vectors $\mathbf{F}$ and $\mathbf{F}_H$ are determined by the relationships

$$F^2 = F_e^2 + F_H^2,$$

$$\sin\varphi = \frac{F_e}{\sqrt{F_e^2 + F_H^2}}.$$

The ratio of the length L of an averaged spiral-shaped trajectory in the presence of a magnetic field to

the sample length l_0 that is the length of the trajectory in the absence of the magnetic field corresponds to the ratio of the forces F and F_e:

$$\frac{L}{l_0} = \frac{F}{F_e} = \sqrt{1 + \left(\beta\frac{F_H}{F_e}\right)^2}. \tag{1}$$

Furthermore, we assume $\beta = 1$.

The ratio $\frac{L}{l_0}$ for averaged trajectory lengths correlates with the ratio $\frac{R_H}{R_0}$ of the resistances R_H and R_0 corresponding to the existence of the imposed magnetic field H and to its absence, respectively. In this case, we also assume that the number of scattering centers per unit length of the trajectories with the lengths l_0 and L is the same, and their density distribution in metal is uniform and independent of the magnetic field. Since $\frac{F}{F_e} = \frac{L}{l_0}$ and, accordingly, $\frac{L}{l_0} = \frac{R}{R_H}$, then, relating the resistances R_H and R_0 to the length l_0 and the cross section S_0 of the sample, we find that the ratio $\frac{R_H}{R_0}$ is equal to the ratio of specific resistances $\frac{\rho_H}{\rho_0}$, which correspond to nonzero and zero magnetic fields, respectively.

$$\frac{R_H}{R_0} = \frac{\rho_H}{\rho_0}, \quad \frac{\rho_H}{\rho_0} = \sqrt{1 + \left(\beta\frac{F_H}{F_e}\right)^2}. \tag{2}$$

The Lorentz force can be expressed in terms of the electric-current intensity i, the electric-current density j, and the magnetic induction B in the form $F_H = iBl$. The Coulomb force is expressed in terms of the electric-current intensity i and the electric-field strength E: $F_e = itE$, where t is the time of the electron displacement along the sample of the length l_0.

In this case, the ratio of the Lorentz and Coulomb forces is

$$\frac{F_H}{F_e} = \frac{Bil}{itE} = \frac{Bl}{tE}.$$

With allowance for Ohm's law for the electric-current density $j = nev$, where v is the averaged transla-

tional velocity of the charge carriers (electrons), the last relationship takes the form

$$\frac{F_H}{F_e} = CB, \quad C = \frac{1}{ne\rho_0} = \frac{\gamma}{\rho_0}.$$

The quantity $\gamma = \frac{1}{ne}$ corresponds to the Hall constant, and $\gamma \approx R_H$.

Expressing $\frac{F_H}{F_e}$ in terms of CB and substituting this ratio into expression (2), we obtain

$$\frac{\rho_H}{\rho_0} = \sqrt{1 + C^2 B^2}. \tag{3}$$

Under the conditions accepted above, this relationship is the exact analytical expression of the Kapitza law.

Substituting the value of C into relationship (3), we obtain

$$\frac{\rho_H}{\rho_0} = \sqrt{1 + \gamma^2\left(\frac{B}{\rho_0}\right)^2}. \tag{3a}$$

As is seen from formula (3a), the Kohler rule is, in fact, a particular case of the Kapitza law. In strong magnetic fields, when $CB \gg 1$, the last expression can be represented in the form

$$\frac{\rho_H}{\rho_0} = \gamma\frac{B}{\rho_0}, \tag{4}$$

which corresponds to the Kohler rule in the strong-field region.

In the transverse magnetic field, a spiral-shaped trajectory is normal to the direction of the electric current. Being deformed, the trajectory is shifted at a translational velocity along this direction. In this case, the trajectory length L' becomes greater than L. We can assume that L' is proportional to L, while the proportionality factor $\eta = \frac{L'}{L}$ is dependent on the magnetic-field intensity.

Since in the absence of magnetic field ($B = 0$), $\frac{L}{l_0} = 1$ and, respectively, $\frac{L'}{l_0} = 1$ and $\frac{R_H}{R_0} = 1$, then consequently, $\eta = 1$ as $B = 0$. The value of η depends on B and has a finite value with large B:

$$\eta = 1 + \alpha(1 - e^{-kB}), \tag{5}$$
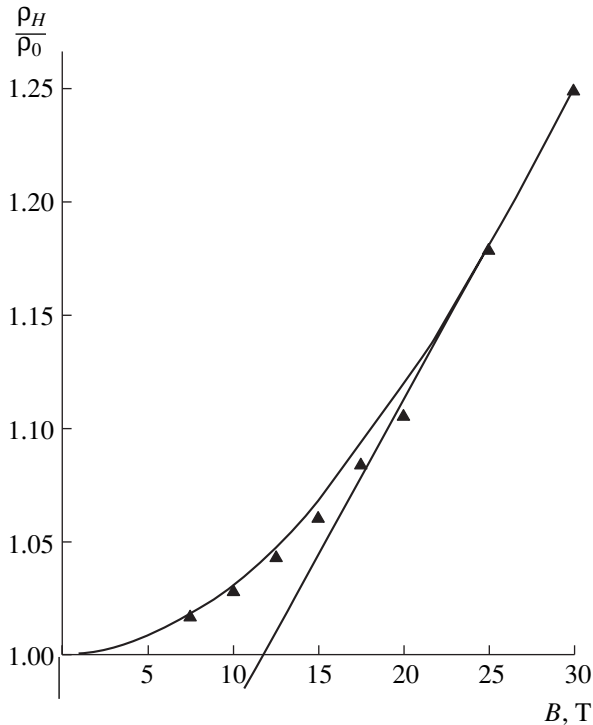
where $k \approx 10^{-2}$.

Fig. 1. Ratio $\dfrac{\rho_H}{\rho_0}$ for a Cu$_4$ sample as a function of the intensity of the longitudinal magnetic field. Calculated curves are compared with the experimental points taken from [2].

Fig. 2. Ratio $\dfrac{\rho_H}{\rho_0}$ in transverse magnetic field for Cu$_{(1)}$, Ag$_{(1)}$, Au$_{(1)}$, and Al$_{(1)}$ samples. Calculated curves are plotted together with the experimental points taken from [2]. The subscripts at the chemical elements correspond to the numbers of curves in figures of [2].

The expression for the transverse effect of the magnetoresistance can be written out in the form

$$\left(\frac{\rho_H}{\rho_0}\right)_{\perp} = \eta\sqrt{1 + C^2 B^2}, \qquad (6)$$

where $C = \dfrac{\beta\gamma}{\rho_0}$. Furthermore, we suppose $\beta \approx 1$.

Expression (6) for the transverse effect of the magnetoresistance can be considered as a generalized formulation of the Kapitza law.

The coefficient α is determined from the ratio of the quantities $\dfrac{\rho_H}{\rho_0}$ for the transverse and longitudinal effects, respectively. According to the experimental data, the coefficient α lies in the range 0.25–0.5.

In Fig. 1, the calculated curve for the ratio $\dfrac{\rho_H}{\rho_0}$ in the case of the longitudinal magnetic-field direction is shown for a sample of Cu$_4$. In the same figure, experimental points taken from [2] are plotted. It is clearly seen that, at low values of the magnetic induction B, the
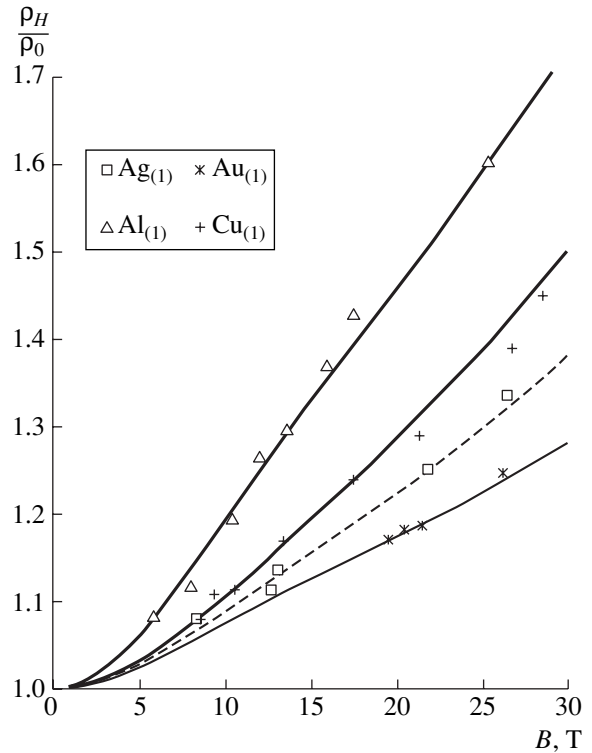
variation of the ratio $\dfrac{\rho_H}{\rho_0}$ as a function of B has a quadratic character, while at $B > 10$ T, it has almost linear dependence. The calculated curve well describes the experimental points (for $\beta = 1$, $\eta = 1$).

The variation of the ratio $\dfrac{\rho_H}{\rho_0}$ is shown in Fig. 2 as a function of the transverse magnetic induction B for the elements Ag$_{(1)}$, Au$_{(1)}$, Cu$_{(1)}$, and Al$_{(1)}$. The experimental points borrowed from [2] are compared with the calculated curves. The values of C^2 and α taken in the calculations are given in the table. As is seen in Fig. 2, the calculated curves are well consistent with the experimental points.

The variation of the specific electrical resistance ρ_H as a function of B for $C = \dfrac{\gamma}{\rho_0}$ can be represented in the form

$$\rho_H = \sqrt{\rho_0^2 + \gamma^2 B^2}. \qquad (7)$$

In accordance with the extended Matissen rule,

Ratios $\dfrac{\rho_H}{\rho_0}$ for $B = 30$ T and certain values of α, C^2, specific electrical resistance ρ, and Hall constants for Cu, Ag, Au, and Al

Chemical element	$\dfrac{\rho_H}{\rho_0}$ [2]	α	C^2, 10^{-4} SI	ρ, 10^{-8} Ω m			R_H, 10^{-11} Ω A^{-1} s^{-1} [14]
				[13]	[13]	[12]	
Cu	1.47	0.082	9.41	0.5 at 73 K	1.7 at 293 K	1.67 at 293 K	−5.3
Ag	1.38	0.082	6.97	0.5 at 53 K	1.62 at 273 K	1.59 at 293 K	−8.98
Au	1.28	0.082	4.444	0.6 at 73 K	2.3 at 293 K	2.35 at 293 K	−7.3
Al	1.73	0.2	12.0	0.33 at 80 K	2.62 at 273 K	2.6545 at 293 K	−2.9

two components, namely non-thermal ρ_a (virtually independent of temperature) and temperature-dependent ρ_T contribute to the specific resistance $\rho_0 = \rho_a + \rho_T$.

Thus,

$$\rho_H = \sqrt{(\rho_a + \rho_T)^2 + \gamma^2 B^2}. \tag{7a}$$

Figure 3 presents the variation of ρ_H at different values of ρ_a. At low temperatures, the value of ρ_T can be ignored, and, in this case, the defining quantity is the non-thermal component ρ_a. As ρ_a (and hence, ρ_0) increases, the curve $\rho_H(B)$ at higher values of B approaches the tangent to the curve describing the linear Kapitza law. This completely corresponds to the observation results presented by Kapitza. The purer a metal sample, the lower values of the magnetic induction B for which the curves ρ_H approach the tangent corresponding to the linear dependence of $\rho_H(B)$.

We should note that, in contrast to the widely held opinion, the specific resistance of a perfectly pure defect-free metal is nonzero ($\rho_{0,\,T \to 0} \ne 0$) as $T \to 0$, since there exists a scattering of charge carriers on zero atomic oscillations in a solid (to say nothing of the fact that a perfectly pure and defect-free solid cannot exist). As $T \to 0$, a perfectly pure defect-free metal is not a superconductor. The transition to the superconducting state as $T \to 0$ is possible as a result of an electron phase transition. As $T \to 0$, the magnetoresistance ρ_H of a perfect metal also is a function of B and increases with the magnetic-field intensity, which does not contradict the third law of thermodynamics.

In its quantitative formulation, the Kapitza law can undoubtedly serve as a basis for understanding the nature of anomalous magnetoresistive effects, including giant ones.
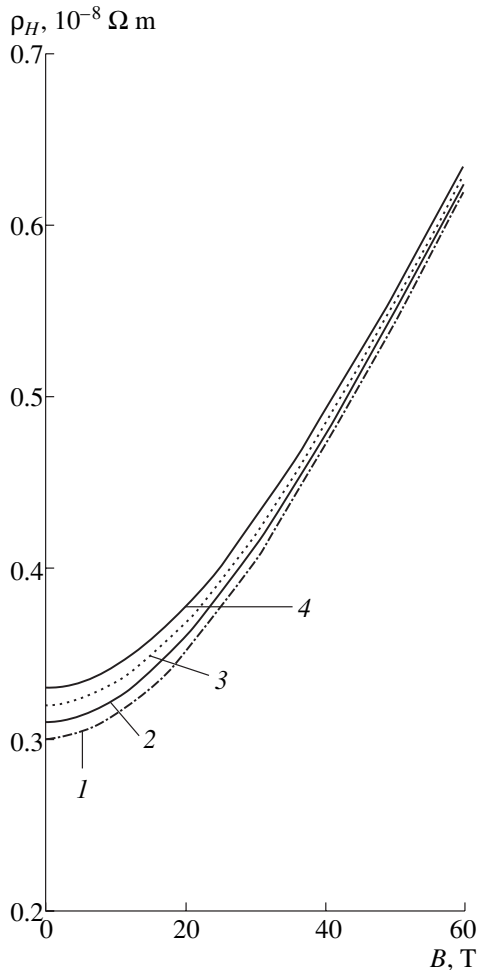

Fig. 3. Variation of the specific electrical resistance ρ_H as a function of the magnetic-field intensity for different initial specific resistances and $\gamma = 9 \times 10^{-11}$ m^3 A^{-1} s^{-1}, $\eta = 1$, $\beta = 1$; (*1*) $\rho_{01} = 0.30 \times 10^{-8}$ Ω m^{-1}; (*2*) $\rho_{02} = 0.31 \times 10^{-8}$; (*3*) $\rho_{03} = 0.32 \times 10^{-8}$; and (*4*) $\rho_{04} = 0.33 \times 10^{-8}$.

REFERENCES

1. P. L. Kapitza, *Strong Magnetic Fields* (Nauka, Moscow, 1988), pp. 174–242; Proc. R. Soc. London, Ser. A **119**, 358 (1928).

2. P. L. Kapitza, *Strong Magnetic Fields* (Nauka, Moscow, 1988), pp. 243–301; Proc. R. Soc. London, Ser. A **123**, 292 (1929).

3. P. L. Kapitza, *Strong Magnetic Fields* (Nauka, Moscow, 1988), pp. 313–318; Metallwirtschube **19**, 443 (1929).

4. P. L. Kapitza, *Strong Magnetic Fields* (Nauka, Moscow, 1988), pp. 322–332; Proc. R. Soc. London, Ser. A **126**, 683 (1930).

5. P. L. Kapitza, *Strong Magnetic Fields* (Nauka, Moscow, 1988), pp. 435–440; *Leipziger Vortrage. Magnetismus* (Hirsel, Leipzig, 1933), p. 1.

6. A. Sommerfeld, Z. Phys. **47**, 43 (1928).

7. J. M. Ziman, *Electrons and Phonons* (Clarendon Press, Oxford, 1960; Inostrannaya Literatura, Moscow, 1962).

8. S. V. Vonsovskiĭ, *Magnetism* (Nauka, Moscow, 1971; Wiley, New York, 1974).

9. N. B. Brandt and S. M. Chudinov, *Electronic Structures of Metals* (Mosk. Gos. Univ., Moscow, 1973), p. 332.

10. Yu. P. Gaĭdukov, Yu. M. Gal'perin, and M. I. Kaganov, in *Encyclopedia of Physics* (Sov. Éntsiklopediya, Moscow, 1988), Vol. 1, pp. 393–398.

11. M. Kohler, Ann. Phys. (Paris) **32**, 211 (1938).

12. J. Emsley, *The Elements* (Clarendon Press, Oxford, 1989; Mir, Moscow, 1993), p. 256.

13. *Properties of Elements: A Reference Book*, Ed. by G. V. Samsonov (Metallurgiya, Moscow, 1976).

14. *Physical Quantities: A Handbook*, Ed. by I. S. Grigor'ev and E. Z. Meĭlikhov (Énergoatomizdat, Moscow, 1991).

Translated by G. Merzon

================ **PHYSICS** ================

Empirical Properties of the Cross Sections for Dissociative Excitation of Cadmium in e–CdX₂ (X = Cl, Br, I) Collisions
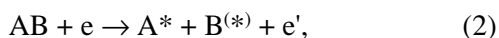
Yu. M. Smirnov

Presented by Academician A.I. Leont'ev June 30, 2003

Received July 8, 2003

**1.** Excited atoms can be formed in single collisions of electrons with atoms and molecules through direct excitation

$$A + e \rightarrow A^* + e' \qquad (1)$$

and dissociative excitation

$$AB + e \rightarrow A^* + B^{(*)} + e', \qquad (2)$$

respectively. Here, A is an atom, A* is the excited atom, B is either an atom coupled with atom A in the molecule or a more complex heavy particle consisting of several atoms, $B^{(*)}$ can be either an atom in the ground or excited state or an unexcited or excited radical, and e and e' are incident and scattered electrons, respectively.

More complex processes of dissociative excitation of atom A in which particle B is ionized are also possible:

$$AB + e \rightarrow A^* + B^+ + e' + e'', \qquad (3)$$
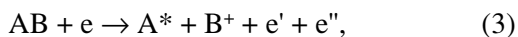
where e'' is an electron knocked out of particle B during its ionization. When the energy of the incident electron is sufficiently high, a single collision can be accompanied by the formation of doubly charged B^{++} or multiply charged B^{N+} ions, where N is the ion charge number. In turn, these ions can be either in the ground or in an excited state. Thus, the number of competitive channels of dissociative excitation can be very large even for comparatively low electron energies in electron–molecule collisions.

The probability of realizing each competitive reaction is characterized by the cross section for dissociative excitation. The presence of a chemical bond between atom A and particle B in molecule AB must undoubtedly give rise to a certain difference of the cross sections for dissociative excitation from the cross sec-

tions for direct excitation. Moreover, the dependences of cross sections on the energy of incident electrons (optical excitation function, OEF) can also be considerably different for dissociative and direct excitations, which is one more manifestation of the chemical bond of atom A in molecule AB.

It is hardly reasonable to doubt that the behavior of the cross sections for dissociative excitation is related to the structure of the electron shell of atom A, structure of molecule AB, and type of the chemical bond between particles A and B in the molecule. At the same time, the behavior of the cross sections for dissociative excitation is almost unstudied experimentally. Moreover, I could not find any theoretical work devoted to the behavior of the cross sections for dissociative excitation.

At present, certain empirical properties have been established only for molecules of alkali metal halides [1–4]. In addition, individual data for a number of halide molecules (other than fluorides) which contain atoms of other metals (Groups II, IV, VII, and VIII) have been reported. However, they have not yet been systematized and are not analyzed for revealing the empirical properties of cross sections. At the same time, the cross sections for dissociative excitation of Cd atoms were measured in collisions of electrons with $CdCl_2$, $CdBr_2$, and CdI_2 molecules [5–7]. Analysis of these results in this work makes it possible to reveal the basic features of dissociative excitation of the Cd atom in comparison with its direct excitation.

2. All experimental results on the cross sections for dissociative excitation of atoms in collisions of electrons with molecules of metal halides were obtained by the method of extended crossing beams. Since the foundations of this method and its engineering realization were previously discussed in detail [8], only the basic conditions of experiments with molecules of cadmium dihalides will be presented.

Beams of cadmium dihalides were obtained by evaporation of the substances under investigation from a tantalum crucible heated by an electron beam. The evaporation temperature for $CdCl_2$, $CdBr_2$, and CdI_2

Moscow Power Engineering Institute (Technical University),
ul. Krasnokazarmennaya 14, Moscow, 111250 Russia
*e-mail: SmirnovYM@mpei.ru*

Table 1. Ratios of dissociative-to-direct excitation cross sections Q_{30} and Q_{max} for CdI and CdII at an incident-electron energy of 30 eV and the maximum of the optical excitation functions, respectively, in e–CdX$_2$ (X = Cl, Br, I) and e–Cd collisions

Upper level	λ, nm	Q_{30} $\dfrac{CdCl_2}{Cd}$	$\dfrac{CdBr_2}{Cd}$	$\dfrac{CdI_2}{Cd}$	Q_{max} $\dfrac{CdCl_2}{Cd}$	$\dfrac{CdBr_2}{Cd}$	$\dfrac{CdI_2}{Cd}$
I $9s^1S_0$	398.193	0.291	0.258	0.654			
$8s^1S_0$	430.667	0.158	0.229	0.475	0.229		
$7s^1S_0$	515.466	0.0813	0.154	0.251	0.155	0.209	
$5p^1P_1^\circ$	228.802	0.0555	0.0977	0.167			
$6d^1D_2$	466.235	0.0994	0.209	0.157	0.144	0.264	0.187
$5d^1D_2$	643.847	0.0330	0.192	0.158		0.212	
$7s^3S_1$	325.252		1.98	2.70			0.838
$6s^3S_1$	467.815	0.500	2.46	3.60	0.141	0.633	0.763
$6s^3S_1$	479.991	0.499	2.71	3.44	0.141	0.698	0.732
$6s^3S_1$	508.582	0.478	2.44	3.18	0.135	0.632	0.677
$5p^3P_1^\circ$	326.105	0.753	1.37	2.16	0.278	0.445	0.566
$7d^3D_{1,2}$	267.759/75			3.04			
$7d^3D_{2,3}$	276.3/4			2.95			
$6d^3D_{1,2}$	288.0/1	0.783	0.647	3.01			
$6d^3D_{2,3}$	298.0/1	0.732	0.665	2.84			
$5d^3D_1$	340.365	0.569	0.663	2.74	0.333		1.19
$5d^3D_{1,2}$	346.6/7	0.364	0.712	2.71	0.267	0.438	1.35
$5d^3D_{2,3}$	361.0/2	0.324	0.587	2.49	0.169	0.283	0.997
II $5p^2P_{1/2}^\circ$	226.502	0.143	0.294	0.813			
$6s^2S_{1/2}$	274.858	0.205					
$a^2D_{3/2}$	325.033	0.0930	0.127	0.199	0.204		
$a^2D_{3/2}$	353.569	0.0946	0.107	0.199	0.217		
$a^2D_{5/2}$	441.563	0.0975	0.159	0.195	0.205	0.407	0.370

was equal to 850, 700, and 600 K, respectively, and the density of molecules in the beam crossing area was equal to 1.7×10^{10}, 7.4×10^9, and 3.1×10^{10} cm^{-3}, respectively. All three molecules have the same point symmetry group $D_{\infty h}$, and the distances between Cd and halogen atoms $r_{Cd–Cl} = (2.21 \pm 0.02) \times 10^{10}$ m, $r_{Cd–Br} = (2.37 \pm 0.02) \times 10^{10}$ m, and $r_{Cd–I} = (2.55 \pm 0.02) \times 10^{10}$ m are accordingly close [9]. The normal vibrations with the hardest bond ν_3 have fundamental frequencies 409, 315, and 265 cm^{-1} [9, p. 89], respectively, and correspond to the same symmetry Σ_u^+ for all three molecules. Under the conditions of this work, the ratios $\dfrac{h\nu}{kT}$

for these vibrations differ by less than 8% for three molecules. Thus, the structure of these molecules and conditions of experiments studying their dissociative excitation can be considered identical.

3. The dissociative excitation of intense spectral lines of the Cd atom and singly charged ion is studied for three molecules under investigation. Atomic lines are excited in processes (1) and (2), and the spectral lines of the singly charged ion are excited in the similar processes
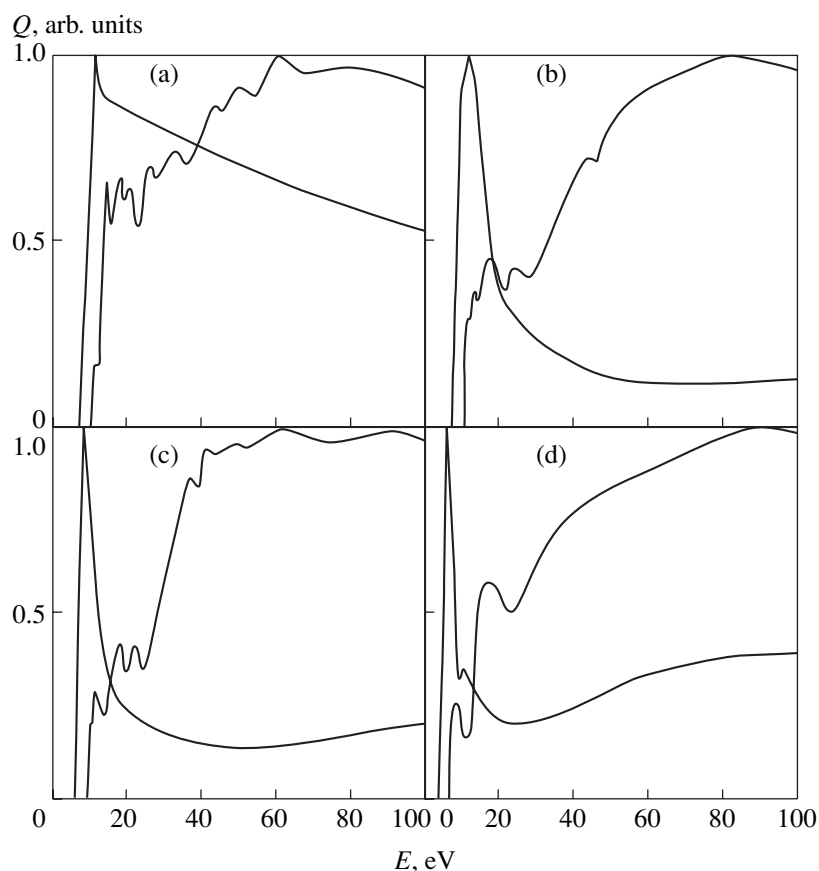
$$A + e \rightarrow A^{+*} + e' + e'', \qquad (4)$$

$$AB + e \rightarrow A^{+*} + B^{(*)} + e' + e''. \qquad (5)$$

Q, arb. units
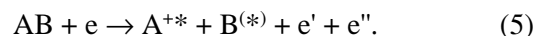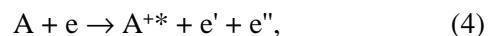
Fig. 1. Optical excitation functions of (solid lines) dissociative and (dashed lines) direct excitation for transitions from the following Cd atomic levels: (a) $5d^1D_2$, (b) $5d^3D_{2,3}$, (c) $6s^3S_1$, and (d) $5p^3P_1^\circ$.

The magnitudes of the cross sections for dissociative excitation were measured for an electron energy of 30 eV. In addition, OEFs for most spectral lines under study were measured in the electron-energy range 0–100 eV.

The measured cross sections for dissociative excitation of the same spectral line can be compared both between three molecules and between each molecule and Cd atom (for its direct excitation in e–Cd collisions). The dissociative excitation of the Cd atom by an electron impact has been studied in a number of works. The most complete uniform data were reported in [10]. However, different experimental groups clearly obtain different results for the same object even when applying similar procedures. Therefore, comparison is more correct for data obtained by the same experimental group on the same setup with maximum maintenance of the procedure and experimental conditions. For this reason, the dissociative excitation of the Cd atom was studied in this cycle of works. Comparison of the corresponding results with data from [10] shows that the magnitudes of cross sections measured in [10] are systematically several times smaller than those obtained in this work. The corresponding ratio is equal to 8.85 in average over all data and is equal to 5.86 when four

extreme values are excluded (this point was discussed in more detail in [6]). Moreover, OEFs were measured in [10] up to electron energy 14–17 eV, and their extrapolation to an energy of 30 eV can be responsible for considerable errors.

Table 1 presents the ratios of dissociative-to-direct excitation cross sections Q_{30} and Q_{max} for the spectral lines of the Cd atom and singly charged ion for an incident-electron energy of 30 eV and in the maximum of the OEF, respectively. The upper levels and wavelengths of the transitions under investigation are also given in Table 1. It should be noted that, according to current concepts, the branching ratios for free atoms are independent of the excitation method. This means that the ratio of intensities of competitive spontaneous transitions from a certain level is determined by the ratio of the Einstein transition probabilities rather than by a particular mechanism of the population of this level.

All spectral lines of the Cd atom in Table 1 are associated with allowed transitions without a change in the multipole order. The only exclusion is the 326.105-nm resonance line from the $5s^2\ ^1S_0 - 5p^3P_1^\circ$ intercombination transition. The upper level of this transition is metastable. Therefore, the correct excitation cross sec-

Table 2. Ratios of cross sections Q_{30} and Q_{max} for dissociative excitation of CdI and CdII for an incident-electron energy of 30 eV and the maximum of the optical excitation functions, respectively, in e–CdX_2 (X = Cl, Br, I) and e–Cd collisions

Upper level	λ, nm	Q_{30} $\dfrac{CdBr_2}{CdCl_2}$	$\dfrac{CdI_2}{CdCl_2}$	$\dfrac{CdI_2}{CdBr_2}$	Q_{max} $\dfrac{CdBr_2}{CdCl_2}$	$\dfrac{CdI_2}{CdCl_2}$	$\dfrac{CdI_2}{CdBr_2}$
I $9s^1S_0$	398.193	0.887	2.24	2.52			
$8s^1S_0$	430.667	1.45	3.01	2.08			
$7s^1S_0$	515.466	1.89	3.08	1.63	1.34		
$5p^1P_1^\circ$	228.802	1.76	3.07	1.75			
$6d^1D_2$	466.235	2.10	1.57	0.747	1.84	1.30	0.707
$5d^1D_2$	643.847	5.81	4.79	0.823			
$7s^3S_1$	325.252			1.37			
$6s^3S_1$	467.815	4.93	7.21	1.46	4.49	5.41	1.20
$6s^3S_1$	479.991	5.41	6.87	1.27	4.96	5.20	1.05
$6s^3S_1$	508.582	5.08	6.62	1.30	4.66	4.99	1.07
$5p^3P_1^\circ$	326.105	1.81	2.86	1.58	1.60	2.04	1.27
$6d^3D_{1,2}$	288.0/1	0.825	3.85	4.66			
$6d^3D_{2,3}$	298.0/1	0.907	3.87	4.27			
$5d^3D_1$	340.365	1.17	4.81	4.13		3.56	
$5d^3D_{1,2}$	346.6/7	1.96	7.41	3.79	1.64	5.05	3.08
$5d^3D_{2,3}$	361.0/2	1.81	7.67	4.23	1.67	5.89	3.52
II $5p^2P_{1/2}^\circ$	226.502	2.05	5.68	2.76			
$a^2D_{3/2}$	325.033	1.37	2.14	1.56			
$a^2D_{3/2}$	353.569	1.13	2.09	1.85			
$a^2D_{5/2}$	441.563	1.63	2.00	1.23	1.99	1.81	0.913

tion of this transition must be determined with a correction for the possibility that excited atoms leave from the field of view of the optical system [11]. However, according to [12], the lifetime of the $5p^3P_1^\circ$ metastable level of the Cd atom is as short as 2.4 μs, which is almost an order of magnitude smaller than the time-of-flight of excited atoms through the collision area under the conditions of this work. This correction is equal to about 5 and 3% for the Cd atom and three molecules under consideration, respectively. Thus, it is negligibly small and is ignored in Table 1.

As is seen in Table 1, the cross sections for dissociative excitation of transitions from singlet levels are several times smaller than the cross sections for direct excitation both at an electron energy of 30 eV and at the maximum of the OEF for all three molecules under study. The corresponding ratio for Q_{30} is less than one-tenth for four low-lying levels of CdI for the CdCl$_2$ molecule as well as for the $a^2D_{3/2, 5/2}$ levels of the singly

charged Cd ion. In contrast, the cross sections Q_{30} for dissociative excitation of transitions from triplet levels are less than the cross sections for direct excitation only for the CdCl$_2$ molecule, as well as for ^3D levels of CdI for the CdBr$_2$ molecule. All cross sections Q_{30} for the dissociative excitation of triplet levels in collisions of electrons with CdI$_2$ molecules are larger than the cross sections for direct excitation by factors 2.16–3.60. The same is true for ^3S and $^3P^\circ$ levels of CdI for the CdBr$_2$ molecule.

However, this is not the case for cross sections Q_{max} for dissociative excitation, which are usually smaller than those for direct excitation. Exclusion is presented by $5d^3D$ levels for the case of the CdI$_2$ molecule, where the cross sections Q_{max} for dissociative and direct excitations virtually coincide with each other. The difference in the behaviors of the ratios for Q_{30} and Q_{max} is attributed to the substantially different shapes of the

OEFs for singlet and triplet transitions for both dissociative and direct excitations. These differences are seen in Fig. 1, where the OEFs for dissociative and direct excitations are shown for transitions from four low-lying levels of the Cd atom (OEFs for dissociative excitation are shown for the $CdBr_2$ molecule; however, their variations for the three molecules under investigation are small). As is seen, the difference between Q_{max} and Q_{30} for the singlet transition in direct excitation is much less than that for triplet transitions. With an increase in the electron energy, the OEFs for triplet transitions decrease rapidly after the maximum by almost an order of magnitude at an energy of 30 eV.

Table 2 presents the ratios of the cross sections for dissociative excitations for three molecules under investigation. As is seen both at an energy of 30 eV and the maximum of the OEFs, the maximum and minimum cross sections correspond in most cases to e–CdI_2 and e–$CdCl_2$ collisions, respectively. Exclusions are presented by the $5,6d^1D_2$ and $6d^3D_J$ levels. More detailed analysis of the revealed properties and determination of their causes are impossible without fundamental theoretical consideration of dissociative excitation.

4. Empirical properties of the cross sections for the dissociative excitation of the Cd atom and singly charged ion are analyzed for collisions of slow monoenergetic electrons with Cd halide molecules. Comparison shows that the cross sections for dissociative excitation at an electron energy of 30 eV are much larger than those for direct excitation for all transitions in CdI and CdII for the $CdCl_2$ molecule. For the CdI_2 molecule, the same behavior is observed for the cross sections for singlet and ionic transitions and the cross

sections for dissociative excitation of triplet transitions are larger than those for direct excitation by factors 2.16–3.60. At the maximum of the OEFs for the molecules under consideration, almost all cross sections for dissociative excitation are less than those for direct excitation.

REFERENCES

1. Yu. M. Smirnov, Dokl. Akad. Nauk **350**, 364 (1996).
2. Yu. M. Smirnov, Dokl. Akad. Nauk **363**, 757 (1998) [Dokl. Phys. **43**, 756 (1998)].
3. Yu. M. Smirnov, Opt. Spektrosk. **87**, 274 (1999) [Opt. Spectrosc. **87**, 255 (1999)].
4. Yu. M. Smirnov, Izv. Vyssh. Uchebn. Zaved. Fiz. (Tomsk) **43** (10), 36 (2000).
5. Yu. M. Smirnov, Khim. Fiz. **19** (4), 44 (2000).
6. Yu. M. Smirnov, Khim. Vys. Énerg. **34**, 405 (2000).
7. Yu. M. Smirnov, Khim. Fiz. **21** (10), 8 (2002).
8. Yu. M. Smirnov, J. Phys. II **4**, 23 (1994).
9. K. S. Krasnov, N. V. Filippenko, V. A. Bobkov, *et al.*, in *Molecular Constants of Inorganic Compounds*, Ed. by K. S. Krasnov (Khimiya, Leningrad, 1979), p. 88.
10. V. V. Sovter, I. P. Zapesochnyǐ, and O. B. Shpenik, Opt. Spektrosk. **36**, 826 (1974).
11. Yu. M. Smirnov, Pis'ma Zh. Tekh. Fiz. **11**, 689 (1985) [Sov. Tech. Phys. Lett. **11**, 287 (1985)].
12. A. A. Radtsig and B. M. Smirnov, *Parameters of Atoms and Atomic Ions: A Handbook* (Énergoatomizdat, Moscow, 1986; Springer-Verlag, Berlin, 1985), p. 257.

Translated by R. Tyapaev

=== **PHYSICS** ===

Characteristics of a Relativistic Electron Avalanche in Air

L. P. Babich*, E. N. Donskoy*, I. M. Kutsyk*, and R. A. Roussel-Dupre**

Presented by Academician R.I. Il'kaev June 19, 2003

Received August 25, 2003

1. The process of generating relativistic runaway electron avalanches (RREAs) is fundamental in the mechanism underlying upward atmospheric discharges [1–6]. A basic characteristic of any avalanche process is the time t_e required for amplifying the particle number by a factor of e. This time was calculated for three chosen overvoltage values $\delta = \dfrac{eE}{F_{min}} P = 2, 5$, and 8 relative to the relativistic minimum of the friction force $F_{min} = 2.18$ keV cm^{-1} atm^{-1} [7–9]. The results obtained by solving the master equation and by direct Monte Carlo simulation turned out to be very consistent with each other, except the Monte Carlo simulation by the ELISA code. This code most completely includes processes of interactions of electrons, positrons, and photons with atomic particles [7–9]. The subsequent analysis demonstrated that the divergence is caused by the incorrect inclusion of the electric field in the ELISA code. For numerical simulation of upward atmospheric discharges, it is necessary to know the dependence $t_e(\delta)$ in a wide range of δ values, realized in the process of the development of upward atmospheric discharges, as well as the energy and angular distributions of avalanche electrons as functions of the overvoltage δ.

In this study, the most important results of corresponding calculations are presented. These calculations are performed by the ELISA code with correct inclusion of an electric field.

2. The calculations were fulfilled for air at atmospheric pressure. We assumed that at the initial time $t = 0$, a monoenergetic beam containing $N(0)$ electrons with kinetic energy ε_0 was injected in the direction of the electric force $-e\mathbf{E}$. The calculations were carried out for two strongly different values $\varepsilon_0 = 2$ and 10 MeV. The statistical error of the calculations did not exceed 1–2%. The electron trajectories were traced down to an energy of $\varepsilon = 1$ keV. Although a large number of electrons with energies lower than the runaway threshold ε_{th}, which is defined as the second root of the equation $F(\varepsilon) = eE$ [10], are generated, these electrons rapidly relax to thermal energies and negligibly contribute to the RREA. As a result, we calculated the number $N(t)$ of runaway electrons as a function of time, as well as the energy and angular distributions of electrons for different δ values. The scale quantity t_e was determined by the linear segment of the function $\ln \dfrac{N(t)}{N(0)}$.

3. In the table, t_e values calculated for three different δ values are given in comparison with previously published results [7–9, 11]. As is seen, the strong divergence of the results obtained by the ELISA code and other codes that either realize the Monte Carlo method or are based on solving the master equation is eliminated. Figure 1 exhibits the dependence $t_e(\delta)$ calculated for the interval $\delta \in [1.3; 14]$, which is of practical interest. We remind that for $\delta \approx 14$, the usual breakdown by electrons having energies close to the ionization threshold of air molecules develops. The sharp increase in t_e up to 8905 ns at $\delta = 1.3$ testifies to approaching a certain critical value of δ below which electrons cannot be involved in the runaway mode. By virtue of this fact, this value of t_e can be rather uncertain. Within an accuracy of 5%, the dependence $t_e(\delta)$ plotted in Fig. 1 can be approximated by the expression

$$ t_e(\text{ns}) = \exp\left(\frac{7.11}{\delta^{0.441}}\right), \quad \delta \in [2, 10]. \qquad (1) $$

We also studied the effect of varying ε_0 on the dynamics of RREAs. For the values of ε_0 under consideration, differences are manifested at $\delta \leq 2$. In this case, the time required for attaining the exponential mode of the RREA decreases with increasing ε_0. In the region $\delta < 2$, this time increases with decreasing δ, and only electrons with high values of ε_0 can be involved in the runaway mode.

---

* *Russian Federal Nuclear Center VNIIEF,*
  pr. Mira 37, Sarov, Nizhegorodskaya oblast,
  607180 Russia
  e-mail: kay@sar.ru

** *Los Alamos National Laboratory,*
  P.O. Box 1663, Mail Stop F569, Los Alamos,
  New Mexico NM 87545, USA
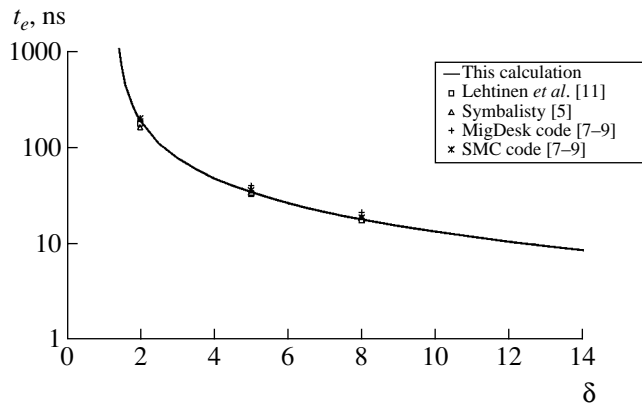 *e-mail: rroussel-dupre@lanf.gov*

Fig. 1. Time of avalanche amplification by a factor of e as a function of the overvoltage. Air, $P = 1$ atm.

The time for settling the steady-state energy distribution of the RREA does not coincide with that required for the avalanche to attain the exponential mode of development. This fact is indirectly confirmed by the calculation results for the time dependence of the mean electron energy $\langle \varepsilon(t) \rangle$ shown in Fig. 2. The mean energy in the steady-state mode weakly varies in the range $\delta = 2$–14, the steady-state mode being attained in $\sim(4$–$6)t_e$. The mean energy monotonically depends on δ and weakly decreases with δ, which is caused by involving electrons of progressively lower energies in the runaway mode.

The weak dependence of $\langle \varepsilon \rangle$ on δ in a wide range of its values can be explained using the expression

$$\langle \varepsilon \rangle_{approx} \approx (\delta - 1) F_{min} c t_e(\delta). \qquad (2)$$

In accordance with this formula, the quantity $\langle \varepsilon \rangle$ is estimated as the energy accumulated by a runaway electron in the path length $c t_e(\delta)$ in which it produces another runaway electron. The weak dependence of $\langle \varepsilon \rangle$ on δ is explained by the dynamic equilibrium of the processes of energy accumulation in the electric field [the multiplier $(\delta - 1)$] and of the generation of secondary elec-

trons [the multiplier $t_e(\delta)$] overwhelming majority of which have the energy much lower than $\langle \varepsilon \rangle$.

In the range $\delta = 2$–8, the stead-state electron energy distributions (normalized to an energy of 1 MeV) in the RREA differ weakly from one another. The maximum difference realized in the energy interval 0.01–40 MeV does not exceed 15%. This universal distribution can be approximated by the function

$$f_1(\varepsilon) = \exp(-0.00108u^6 - 0.004235u^5 + 0.009757u^4)$$
$$\times \exp(0.012652u^3 - 0.056372u^2 - 0.43325u - 2.1185), \qquad (3)$$

where $u = \ln \varepsilon$ (1 MeV).

After integrating over all the energies, we arrive at the angular distributions of electrons, which can be approximated by the function

$$g(\mu, b) = \frac{1 - b^2}{2\pi(1 - b\mu)^2}, \qquad (4)$$

where $b = 0.91$ for $\delta = 2$ and $b = 0.97$ for $\delta = 8$. Here, μ is the cosine of the angle between the electron momentum and electric field force $-e\mathbf{E}$ and the usual normalization

$$2\pi \int_0^1 g(\mu, b) d\mu = 1$$

is accepted. The maximum error of approximation (4) is attained at μ values close to unity and is equal to 12 and 34% for $\delta = 2$ and 8, respectively. In contrast to the energy distributions, the steady-state angular distributions essentially depend on the quantity δ becoming prolated with increasing δ. In other words, the progressively larger part of electrons is carried away by the field as its intensity increases.

Characteristic amplification time t_e, ns, for an avalanche in air at atmospheric pressure

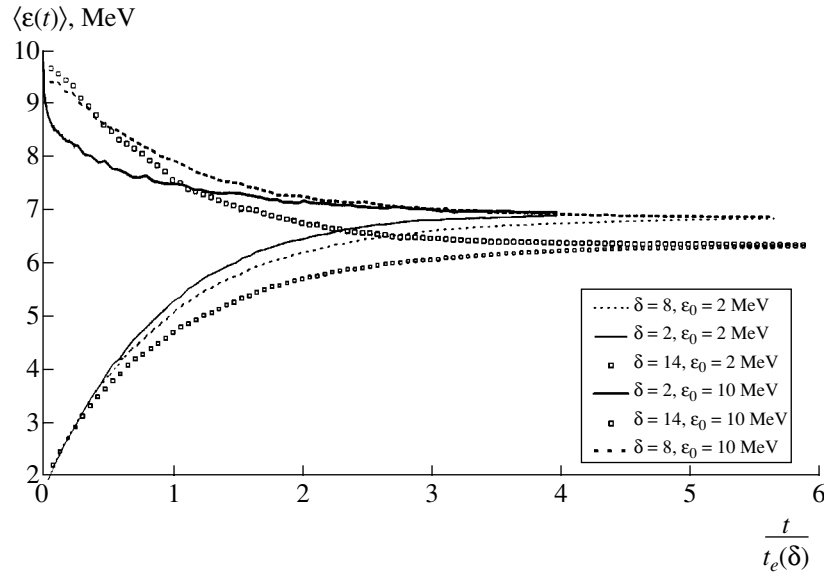| $\delta = \dfrac{E}{2.18 \text{ kV m}^{-1}}$	Master equation		Monte Carlo calculations			
	[5]	MigDesk code [7–9]	[11]	SMC code [7–9]	ELISA code	
					[7–9]	new results
2	161	197	174.4	200	440	189.7
5	34.4	39.9	33.2	35.6	54	34.3
8	18.9	21.2	17.3	18.6	27.5	17.8

Fig. 2. Mean electron energy as a function of time for different values of the initial electron energy ε_0 and overvoltages δ. Air, $P = 1$ atm.

The normalized steady-state angular and energy distributions of runaway electrons can be represented in the form

$$f(\varepsilon, \mu) = f_1(\varepsilon)f_2(\mu|\varepsilon),$$

where $f_1(\varepsilon)$ is the steady-state electron energy distribution approximated by formula (3) and $f_2(\mu|\varepsilon)$ is the normalized steady-state angular distribution of electrons with energy ε. The latter may be approximated by the expression

$$\ln f_2(\mu|\varepsilon) = \begin{cases} y_1(\varepsilon) - k_1(\varepsilon)(1-\mu), & \mu \geq 0 \\ y_2(\varepsilon) + k_2(\varepsilon)(\mu+1), & \mu < 0. \end{cases}$$

Here,

$$y_1(\varepsilon) = 0.5756\ln(0.9\varepsilon) - 0.46,$$

$$k_1(\varepsilon) = 1.24(14\varepsilon)^{0.5} - 0.92,$$

$$y_2(\varepsilon) = -2.76(2.3\varepsilon)^{0.48} - 2.53,$$

$$k_2(\varepsilon) = 0.557\ln(\varepsilon) + 2.91 \quad \text{for} \quad \delta = 2.$$

and

$$y_1(\varepsilon) = 0.6178\ln(\varepsilon) + 0.4145,$$

$$k_1(\varepsilon) = 3.224(5\varepsilon - 0.07)^{0.57},$$

$$y_2(\varepsilon) = -7.6(4\varepsilon)^{0.31} - 0.6,$$

$$k_2(\varepsilon) = 0.8858\ln(\varepsilon) + 5.142 \quad \text{for} \quad \delta = 8.$$

4. The basic result of the present study is the dependence of the characteristic RREA amplification time t_e on the electric field intensity. This time determines the relativistic analog of the Townsend ionization coefficient $\frac{1}{ct_e}$. The passage from the time values at atmospheric pressure to those at the pressure P is executed according to the formula

$$t_e(P) = \frac{t_e(1\ \text{atm})}{P(\text{atm})}.$$

In the range of overvoltages $\delta = 2$–8, a universal energy distribution of runaway electrons is virtually independent of δ. An analytical approximation of this distribution has been proposed. For $\delta = 2$ and 8, the angular distributions of runaway electrons of all energies, as well as angular distributions in separate energy groups, have been calculated, for which approximating formulas have also been obtained. As should be expected, with increasing δ and electron energy, the runaway-electron beam becomes more highly directed along the electric force $-e\mathbf{E}$. The results obtained are recommended for use in modeling upward atmospheric discharges above thunderstorm clouds.

A.V. Gurevich for the many years of cooperation in this field.

REFERENCES

1. A. V. Gurevich, G. M. Milikh, and R. A. Roussel-Dupre, Phys. Lett. A **165**, 463 (1992).

2. R. A. Roussel-Dupre, A. V. Gurevich, T. Tunnel, and G. M. Milikh, Los Alamos Technical Report LA-12601-MS (Los Alamos Natl. Lab., Los Alamos, 1993).

3. R. A. Roussel-Dupre, A. V. Gurevich, T. Tunnel, and G. M. Milikh, Phys. Rev. E **49**, 2257 (1994).

4. E. M. D. Symbalisty, R. A. Roussel-Dupre, L. P. Babich, *et al.*, EOS Trans. Am. Geophys. Union **78**, 4760 (1997).

5. E. M. D. Symbalisty, R. A. Roussel-Dupre, and V. Yukhimuk, IEEE Trans. Plasma Sci. **26**, 1575 (1998).

6. A. V. Gurevich and K. P. Zybin, Usp. Fiz. Nauk **171**, 1177 (2001) [Phys. Usp. **44**, 1119 (2001)].

7. L. P. Babich, E. N. Donskoy, R. I. Il'kaev, *et al.*, Dokl. Akad. Nauk **379**, 606 (2001) [Dokl. Phys. **46**, 536 (2001)].

8. L. P. Babich, E. N. Donskoy, I. M. Kutsyk, *et al.*, IEEE Trans. Plasma Sci. **29**, 430 (2001).

9. L. P. Babich, E. N. Donskoy, A. Yu. Kudryavtsev, *et al.*, Tr. Ros. Feder. Yad. Tsentra VNIIÉF **1**, 432 (2001).

10. L. P. Babich, Teplofiz. Vys. Temp. **33**, 659 (1995).

11. N. G. Lehtinen, T. F. Bell, and U. S. Inan, J. Geophys. Res. **104**, 24699 (1999).

Translated by G. Merzon

<center>══════════ **PHYSICS** ══════════</center>

Regular and Stochastic Nonlinear Dynamics of Magnetization in an Exchange-Coupled Multilayer Structure

D. I. Sementsov* and A. M. Shutyǐ**

Presented by Academician V.V. Osiko October 13, 2003

Received September 19, 2003

Various oscillating systems with both stochastic and regular dynamical regimes have attracted wide attention in recent years [1]. Among the most studied of such systems are magnetically ordered structures whose dynamics is associated with the precession motion of magnetization and is generally described by the Landau–Lifshitz nonlinear equations [2, 3]. Of great interest today are multilayer exchange-coupled structures, where giant magnetoresistive and magnetooptical effects have been discovered [4–6]. The existence of static and dynamical bistable states characteristic of a magnetic subsystem is substantial for the practical use of such structures [7, 8]. The behavior of the magnetic subsystem near these states determines the features of the self-organization of magnetization, which proceeds in external magnetic fields [9]. In this work, we analyze dynamical regimes of the magnetization of a multilayer nanostructure with an antiferromagnetic interlayer exchange coupling that permits the realization of various equilibrium states [10]. We show that there are narrow frequency bands where self-sustained oscillations transform to stochastic oscillations of magnetization.

1. We consider a structure consisting of a large number ($n \gg 1$) of identical layers of magnetic metal that are separated by nonmagnetic layers, ensuring antiferromagnetic ordering of the magnetic moments of neighboring layers in the initial state. In this case, the entire set of magnetic layers is divided into two subsystems ($j = 1, 2$), where the magnetic moments of layers behave identically in each subsystem. For such structures, magnetic anisotropy includes induced easy-axis anisotropy and cubic crystallographic anisotropy. In this case, the [100] and [010] crystallographic axes lie in the layer plane, and the easy-magnetization axis of induced anisotropy is perpendicular to the layers.

The free energy of the system per unit area is determined by the expression

$$E = d\frac{n}{2} \sum_{j=1,2} \left[-\mathbf{H}\mathbf{M}_j + \frac{K_1}{4}(\sin^2 2\psi_j + \cos^4 \psi_j \sin^2 2\varphi_j) \right.$$
$$\left. + (K_u - 2\pi M^2)\cos^2 \psi_j \right] + Jn\frac{\mathbf{M}_1\mathbf{M}_2}{M^2}, \quad (1)$$

where d is the thickness of magnetic layers, $\mathbf{M}_j$ is the magnetization of the layers of the jth subsystem, J is the bilinear exchange coupling constant of the magnetic moments of the nearest layers, K_1 and K_u are the constants of cubic and growth anisotropy, $\mathbf{H}$ is the static magnetizing field, φ_j is the azimuth angle that is measured from the [100] axis and determines the plane orientation of the magnetic moment, and ψ_j is the exit angle of the vector $\mathbf{M}_j$ from the film plane.

In the spherical coordinate system, the equations of motion of the magnetization vectors of each layer are represented in the form

$$\dot{\varphi}_j M d \cos \psi_j = \gamma\frac{\partial E}{\partial \psi_j} + \frac{\lambda}{M}\frac{1}{\cos\psi_j}\frac{\partial E}{\partial \varphi_j},$$
$$\dot{\psi}_j M d = \frac{\lambda}{M}\frac{\partial E}{\partial \psi_j} - \gamma\frac{1}{\cos\psi_j}\frac{\partial E}{\partial \varphi_j}, \quad (2)$$

where γ is the gyromagnetic ratio and λ is the damping parameter. The parameters corresponding to the real $(\text{Fe/Cr})_n$ structure are used in numerical analysis. We take $M = 1620$ G, $K_1 = 4.6 \times 10^5$ erg/cm^3, $K_u = 2.06 \times 10^6$ erg/cm^3, $\lambda = 5 \times 10^7$ s^{-1}, $\gamma = 1.76 \times 10^7$ (Oe s)$^{-1}$, and $d = 21.2 \times 10^{-8}$ cm for iron layers. The parameters of chromium layers do not enter into Eq. (1), but they determine the coupling constant J [11].

2. Since demagnetizing fields are strong ($4\pi M \gg 2K_u/M, JM$) for an in-plane magnetizing field, magnetic moments also lie in the layer plane; i.e., equilibrium angles are equal to zero ($\psi_{0j} = 0$). The equilibrium azi-

_____
Ul'yanovsk State University, ul. L'va Tolstogo 42,
Ul'yanovsk, 432700 Russia
* *e-mail: sementsovdi@ulsu.ru*
** *e-mail: shuty@mail.ru*

muth angles $\varphi_{0j}(H)$ are determined by the relations $\dfrac{\partial E}{\partial \varphi_j} = 0$ and $\dfrac{\partial^2 E}{\partial \varphi_j^2} > 0$. Analysis of these conditions shows that, when the coupling constant J in the systems under consideration is sufficiently small, change in the magnetizing field intensity is accompanied by the appearance of orientational hysteresis loops and corresponding bistability states. Therefore, for the initial orientation of magnetic moments $\varphi_{0j} = \pm\dfrac{\pi}{2}$ and magnetizing-field orientation $\varphi_H = 0$, i.e., for $\mathbf{M}_{0j} \perp \mathbf{H}$, noncollinear symmetric orientation ($\varphi_{02} = -\varphi_{01}$) of the magnetic moments of neighboring layers has an equilibrium in the interval $0 < H \le H_a$. The angle between the magnetic moments of neighboring films $\Delta\varphi_0 = \varphi_{01} - \varphi_{02}$ decreases with an increase in the field in this interval. When the field reaches the critical value H_a, the angle $\Delta\varphi_0$ reaches a minimum (which decreases with an increase in the coupling constant). Then a phase transition occurs and the collinear field-aligned orientation of the magnetic moments is established. When the magnetizing field decreases from $H > H_a$, the state with the field-aligned orientation of the magnetic moments of films retains the field intensity H_b. For $H = H_b < H_a$, the inverse phase transition occurs with an orientational divergence of the vectors $\mathbf{M}_1$ and $\mathbf{M}_2$ that instantaneously reach the angles $\pm\varphi_0(H_b)$. With a further decrease in the magnetizing field, $\Delta\varphi_0$ increases and $\Delta\varphi_0 = \pi$ for $H = 0$. The critical fields that are edges of the orientational hysteresis loop are given by the expressions

$$H_b = \frac{2}{M}\left(\frac{2J}{d} - K_1\right),$$

$$H_a = \frac{4}{3M}\sqrt{\frac{J}{3dK_1} + \frac{1}{6}}\left(\frac{2J}{d} + K_1\right). \tag{3}$$

With an increase in the coupling constant, the hysteresis loop is contracted and disappears for $J \ge J_{ab}$, where J_{ab} is determined from the equality $H_b = H_a$.

Systems with narrow hysteresis loops are of particular interest for implementation of various dynamical regimes. For H values corresponding to the middle of the hysteresis loop, a longitudinal microwave field ($\mathbf{h} \parallel \mathbf{H}$) with an amplitude close to the loop width ($h \ge H_a - H_b$) induces various large-amplitude self-sustained oscillations and stochastic regimes in the system of magnetic moments. In addition to wide frequency bands corresponding to stochastic oscillations, there are narrow frequency bands ($\Delta\omega \sim 10^7$ s^{-1}) where stochastic regimes exist and beyond which regular large-amplitude regimes are realized.

3. Figure 1 shows the phase trajectories $\dot{\varphi}_1(\varphi_1)$ of the magnetic moments of the first subsystem of layers for various frequencies of the alternating field. Frequencies $\omega = (7.9, 8.7) \times 10^8$ and $(9.9, 10.2) \times 10^8$ s^{-1} (Figs. 1a, 1c, dashed and solid lines) correspond to regular regimes, whereas frequencies $\omega = (8.0, 9.95) \times 10^8$ s^{-1} (Figs. 1b, 1d) correspond to stochastic oscillations. The inserts show the corresponding time dependences $\varphi_1(t)$. Calculations were carried out with the exchange coupling constant $J = 0.24$ erg/cm^2 close to $J_{ab} \approx 0.244$ erg/cm^2; the magnetizing field $H = 2227.4$ Oe, for which the collinear equilibrium state with the angles $\varphi_{0j} = 0$ is realized; and alternating-field amplitude $h = 0.2$ Oe exceeding $H_a - H_b \approx 0.144$ Oe. Oscillations of the magnetic moments of the second subsystem are always in opposite phase with the first system. In this case, the equality $\varphi_2(t) = -\varphi_1(t)$ is quite accurately satisfied for both regular and stochastic regimes. For films under investigation, the amplitude of polar-angle oscillations is always much smaller than the amplitude for the azimuth angle, i.e., $\psi_j \ll \varphi_j$. Analysis of the dynamics of the magnetization of each subsystem of layers shows that with a decrease in frequency stochastic regimes are established after a bifurcation cascade of period doubling. At the same time, self-sustained oscillations with the alternating-field period are again realized after one bifurcation. Regular regimes at a frequency above the stochastic-dynamics interval, i.e., at a larger frequency (solid lines), and at a frequency below the indicated interval (dashed lines) can both be very close (Fig. 1c) and very different in phase trajectories (Fig. 1a). However, oscillations have high amplitudes in both cases. The amplitude of stochastic oscillations differs slightly from the amplitude of self-sustained oscillations. Stochasticity is primarily manifested in smearing of the boundary of the phase trajectory of the limit cycle.

Strange attractors (Figs. 1b, 1d) corresponding to stochastic dynamics have sections of strong compression or folds and sections of extension. This shape is responsible for sensitivity of phase trajectories to the initial conditions. The distance between two close phase trajectories first increases exponentially as $\delta = \delta_0 \exp(\zeta t)$, where ζ is the maximum Lyapunov coefficient (which is equal to the slope of the straight line approximating the divergence of phase transitions). For the cases under consideration, $\zeta \approx 1.1 \times 10^8$ and 4.1×10^7 s^{-1} for $\omega = 8 \times 10^8$ and 9.95×10^8 s^{-1}, respectively. After divergence to the attractor scale, the distance between phase trajectories oscillates around the value determined by the attractor size.

The regimes discussed above are sensitive to the magnetizing field. Figure 2 shows the bifurcation diagram for the parameters indicated above and alternating-field frequency $\omega = 8 \times 10^8$ s^{-1} corresponding to stochastic oscillations of magnetization for $H =$

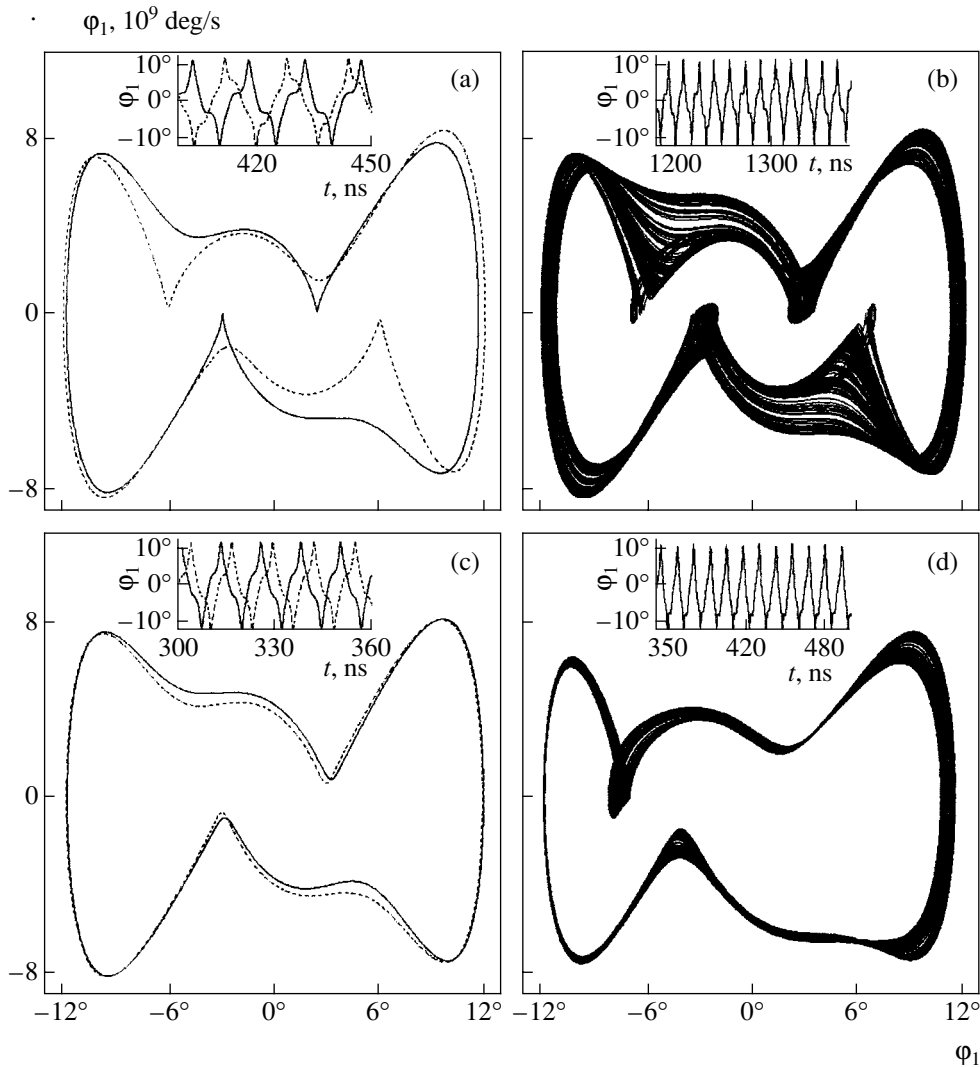$\dot{\varphi}_1$, 10^9 deg/s

Fig. 1. Phase trajectories of (a, c) regular and (b, d) stochastic oscillations of the magnetizations of layers. The inserts show $\varphi_1(t)$.

2227.4 Oe (Fig. 1b). In this diagram, the maximum and minimum angles of the magnetic moment of the first subsystem of layers are shown for the given interval of the magnetizing field. For a given H value, a single point with zero angle φ_{1m} corresponds to the absence of oscillations, two points correspond to the oscillation regime with one maximum φ_{1max} and one minimum φ_{1min}, a larger countable set of points corresponds to more complex oscillations, and a set of close points corresponds to the stochastic dynamics of magnetic moments. It is seen that a decrease in H by only 0.01 Oe from the earlier accepted value converts the system from the stochastic regime to one of self-sustained oscillations. However, this regime is realized only in a very narrow interval of the magnetizing field ($\Delta H \approx$ 0.02 Oe), and then stochasticity is again developed and covers the entire range of oscillations of the magnetic moment. When the magnetizing field approaches the boundary value of the hysteresis loop, small-amplitude

regular oscillations corresponding to the noncollinear equilibrium orientation of the magnetic moments of the system settle. With an increase in H, stochasticity first increases, then the system becomes insensitive to perturbation by the alternating field, because the alternating field goes beyond the hysteresis loop and corresponds to the collinear field-aligned orientation of the magnetic moments. For other frequencies close to that which is chosen, the bifurcation diagram has similar basic features.

Analysis shows that oscillation regimes of a multilayer structure with an antiferromagnetic exchange coupling are characterized by quite narrow frequency bands, where the longitudinal alternating magnetic field excites stochastic oscillations of the magnetic moments of the system. Large-amplitude self-sustained oscillations are realized at frequencies adjacent to these bands. Such structures are also characterized by a high
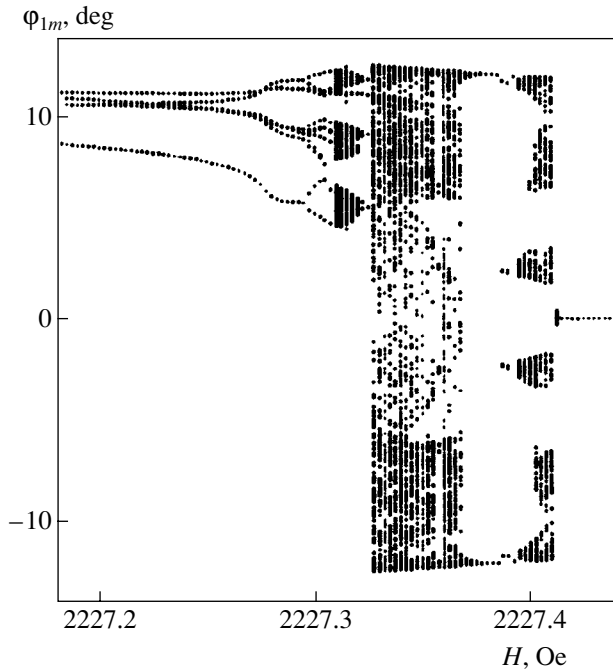
φ_{1m}, deg

Fig. 2. Bifurcation diagram of the field dependence of the maximum and minimum of the angle φ_1.

sensitivity of these dynamical regimes to variation in the magnetizing field.

ACKNOWLEDGMENTS

REFERENCES

1. G. G. Malinetskiĭ and A. B. Potapov, *Modern Problems of Nonlinear Dynamics* (Editorial URSS, Moscow, 2002).

2. S. M. Rezende and F. M. de Aguiar, Proc. IEEE **78**, 893 (1990).

3. A. G. Gurevich and G. A. Melkov, *Magnetic Oscillations and Waves* (Nauka, Moscow, 1994).

4. V. V. Ustinov, M. M. Kirillova, I. D. Lobov, *et al.*, Zh. Éksp. Teor. Fiz. **109**, 477 (1996) [JETP **82**, 253 (1996)].

5. V. V. Kostyuchenko and A. K. Zvezdin, Phys. Rev. B **57**, 5951 (1998).

6. G. S. Patrin, N. V. Volkov, and V. P. Kononov, Pis'ma Zh. Éksp. Teor. Fiz. **68**, 287 (1998) [JETP Lett. **68**, 307 (1998)].

7. D. I. Sementsov and A. M. Shutyĭ, Dokl. Akad. Nauk **387** (1), 51 (2002) [Dokl. Phys. **47**, 788 (2002)].

8. D. I. Sementsov and A. M. Shutyĭ, Pis'ma Zh. Éksp. Teor. Fiz. **74**, 339 (2001) [JETP Lett. **74**, 306 (2001)].

9. F. V. Lisovskiĭ and O. P. Polyakov, Pis'ma Zh. Éksp. Teor. Fiz. **73**, 546 (2001) [JETP Lett. **73**, 483 (2001)].

10. D. I. Sementsov and A. M. Shutyĭ, Pis'ma Zh. Éksp. Teor. Fiz. **75**, 287 (2002) [JETP Lett. **75**, 242 (2002)].

11. N. G. Bebenin and V. V. Ustinov, Fiz. Met. Metalloved. **84** (2), 29 (1997).

Translated by R. Tyapaev

====== TECHNICAL ======
====== PHYSICS ======

Optimizing the Reception of Signals Emitted by Ultrashort-Pulse Antennas

Corresponding Member of the RAS L. D. Bakhrakh* and M. Ya. Izrailovich**

INTRODUCTION

In the case of irradiating an object to be identified by ultrashort-pulse antennas, the goal of the most efficient reception of reflected signals arises. In this case, it is necessary to provide the most consistent time diagrams for both the signal being reflected from the object and the signal at the input of a receiver. It is well known that the characteristics of a receiver can be described in terms of a linear stationary dynamic transformation linking input and output signals. Therefore, we need to find the functional description of the corresponding pulsed transition function that ensures the minimal divergence of the signal being reflected from that at the receiver output. In addition, it is desirable to provide operation conditions for the receiver that correspond to the minimization of residual radiation. This radiation arises by virtue of both a certain time stretching of a signal emitted by the antenna and dynamic distortions occurring while the signal propagates through the medium prior to reaching the object, as well as after the reflection. To this aim, it is rather reasonable to apply a supplementary correcting signal to the input of the receiver along with the signal reflected from the object under study. This correcting signal provides partially or complete quenching of a signal at the receiver output at a prescribed moment of time.

In this paper, we describe procedures for the solution of the aforementioned problem on the basis of employing variational methods.

CONSTRUCTING THE OPTIMAL PULSED TRANSITION FUNCTION OF A RECEIVER

The functional diagram of a signal-emitting and signal-receiving system based on an ultrashort-pulse antenna is presented in the figure.

It is assumed that each element of the system transforms a signal $x(t)$ applied to the input of the ultrashort-pulse antenna into a consequent signal. This occurs by means of a linear dynamic transformation determined by the corresponding pulsed transition function. By virtue of this fact, a signal at the antenna's output can be written in the form

$$y_0(t) = \int_0^t h_0(t - \tau)x(\tau)d\tau. \qquad (1)$$

In the general case, the input signal $x(t)$ of the antenna consists of both the signal $x_0(t)$ produced by an ultrashort-pulse generator and a correcting signal [1] or a dynamically transformed signal together with a supplementary correcting signal [2, 3]. It is worth noting that such a correction of the signal $y_0(t)$ emitted by the antenna has the following goals:

(i) the correspondence to a certain perfect (desirable) shape $y_*(t)$ (in particular, a triangular or trapezoidal shape) of the time diagram for the signal $y_0(t)$;

(ii) lowering the intensity of the residual radiation at a certain specified moment of time or the complete elimination of this radiation.

Both these goals can be attained only in part because the true signal $x_0(t)$ has a short duration and a high intensity, whereas the correcting action is more strongly stretched in time and has a lower peak intensity.

While passing through the medium, the signal $y_0(t)$ emitted by the antenna is subject to the linear dynamic transformation

$$y_1(t) = \int_0^t h_1(t - \tau)y_0(\tau)d\tau, \qquad (2)$$

after which the signal is reflected from the object in the

----

* *Moscow Scientific Research Institute*
  of Instrument Engineering,
  Kutuzovskiĭ pr. 34, Moscow, 121170 Russia
** *Blagonravov Institute of Engineering Science,*
  Russian Academy of Sciences,
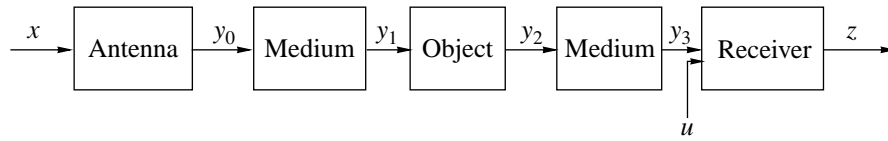 *ul. Bardina 4, Moscow, 117334 Russia*

Figure.

transformed form

$$y_2(t) = \int_0^t g(t - \tau) y_1(\tau) d\tau. \qquad (3)$$

Here, $h_1(t - \tau)$ and $q(t - \tau)$ are pulsed transition functions describing dynamic properties of the medium and the object, respectively. A signal reflected from the object and, furthermore, passing through the medium arrives at the input of the object in the form

$$y_3(t) = \int_0^t h(t - \tau) y_2(\tau) d\tau. \qquad (4)$$

The receiver also realizes dynamic transformation of the signal $y_3(t)$ arriving at its input. As a result, the signal

$$z(t) = \int_0^t v(t - \tau) y_3(\tau) d\tau = \int_0^t y_3(t - \tau) v(\tau) d\tau \quad (5)$$

is formed at the receiver output, where $v(t - \tau)$ is the receiver pulsed transition function to be determined.

The perfect situation would correspond to the exact reproduction of the signal $y_2(t)$ reflected from the object. In this case, in accordance with expressions (3), (5), the function $v(t)$ must satisfy the equation

$$z(t) = \int_0^t y_3(t - \tau) v(\tau) d\tau = y_2(t). \qquad (6)$$

However, according to [4], the problem of solving Eq. (6) belonging to Volterra integral equations of the first kind is related to ill-posed problems.

In accordance with [4], in order to regularize this problem it is necessary to minimize the functional

$$J(v) = \int_0^T \{ [z(t) - y_2(t)]^2 + \gamma_1 v^2(t) \} dt, \qquad (7)$$

where γ_1 is the regularization parameter and T is a certain fixed time corresponding to the end of the signal reception.

The first term of functional (7) is an integral quadratic deviation of the signals $z(t)$ and $y_2(t)$. The second term is the integral intensity squared of the desired function $v(t)$.

The most efficient method for solving the problem of the minimization of functional (7) is the use of a variational method based on abstract linear operators acting in the $L^2(0; T)$ space [5]. In this case, expression (5) and functional (7) are written out as $z = Y_3 v$ and

$$J(v) = (Y_3 v - y_2, Y_3 v - y_2) + \gamma_1 (v, v), \qquad (8)$$

respectively.

Furthermore, in accordance with [5], the derivative of the Gateaux functional $J(v)$ (8) is calculated. From the condition requiring this derivative to be zero, the condition of the stationary behavior

$$(Y_3 v - y_2, Y_3 \tilde{v}) + \gamma_1 (v; \tilde{v}) = 0 \qquad (9)$$

is determined. Here, $\tilde{v}$ is an arbitrary function (the increment of the function v). It follows from condition (9) that

$$(Y_3^* Y_3 - Y_3^* y_2, \tilde{v}) + \gamma_1 (v, \tilde{v}) = 0, \qquad (10)$$

where Y_3^* is an operator conjugate to the operator Y_3. As long as the function $\tilde{v}$ is an arbitrary function, we can determine from Eq. (10) the equation with respect to the quantity v:

$$(Y_3^* Y_3 + \gamma_1) v = Y_3^* y_2. \qquad (11)$$

It follows from Eq. (11) that

$$v_* = (Y_3^* Y_3 + \gamma)^{-1} Y_3^* y_2, \qquad (12)$$

where $(Y_3^* Y_3 + \gamma)^{-1}$ is the operator inverse to the operator $Y_3^* Y_3 + \gamma_1$.

According to relationship (5), the operator Y_3^* conjugate to the operator Y_3 is determined by the following relationship:

$$Y_3^* f = \int_t^T y_3(s-t)f(s)ds.$$

Therefore, Eq. (11) in the nonabstract form can be written out as

$$\int_t^T y_3(s-t)\int_0^s y_3(s-\tau)v(\tau)d\tau ds + \gamma v$$
$$= \int_t^T y_3(s-t)y_2(s)ds. \qquad (13)$$

Equation (13) is a Volterra integral equation of the second kind. Hence, it follows that the operator $(Y_3^* Y_3 + \gamma)^{-1}$ entering into the expression of the function v_* (12) is the resolvent of Eq. (13).

CONSTRUCTION
OF AN ADDITIVE CORRECTING SIGNAL

After determination of the optimal pulsed transition function $v_*(t)$ of the receiver, the problem of an additive correcting signal applied to the input of this device is solved in accordance with definition (12) by the following method.

Since the function $v_*(t-\tau)$ is now known, the signal at the receiver output in the case of adding a supplementary signal $u(t)$ to the signal $y_3(t)$ is determined in the form[1]

$$z(t) = \int_0^t v_*(t-\tau)[y_3(\tau) + u(\tau)]d\tau. \qquad (14)$$

As was indicated above, the main goal of introducing the correcting signal $u(t)$ is to minimize the intensity of the residual radiation caused by the additional dynamic distortion of the reflected signal $y_2(t)$ while it is passing through the medium from the object to the receiver. However, the signal $u(t)$ can also be employed to solve the problem of improving the similarity of the signals $z(t)$ and $y_2(t)$. Acting in this direction, we can attain a smaller divergence of the signals $z(t)$ and $y_2(t)$ than that obtained by the optimization of the pulsed transition function of the receiver. In this case, we

---

[1] It should be noted that the signal $u(t)$ can be switched on only in cases where the existence of the basic signal $y_3(t)$ is fixed. In other words, in real situations the signal $u(t)$ begins to act with a certain delay. Here, we assume this delay to be short so that it can be ignored.

should take into account the fact that the intensity of the signal $u(t)$ must be limited. In accordance with the aforementioned arguments, the determination of the optimal variation law for the signal $u_*(t)$ is associated with solving the problem of minimization of the functional

$$J(u) = \int_0^T \{[z(t) - y_2(t)]^2 + \gamma_2 u^2(t)\}dt + \lambda z(T), \quad (15)$$

where γ_2 is the weight coefficient and λ is the Lagrange multiplier being introduced to provide the given (minimal) amplitude of the signal $z(t)$ at a finite moment of time.

With allowance for expression (14), the functional (15) can be written out in the abstract form

$$J(u) = (V_* u + V_* y_3 - y_2, V_* u + V_* y_3 - y_2)$$
$$+ \gamma_2(u, u) + \lambda V_*(T)(y_3 + u). \qquad (16)$$

Here, V_* corresponds to the operator determined in accordance with relationship (14), whereas $V_*(T)$ is the same operator for the moment of time $t = T$.

As a result of applying the procedure described in [5] to functional (16) and in accordance with the scheme discussed above, the operator equation

$$V_*^* V_* u + \gamma_2 u = V_*^* y_2 - V_*^* V_* y_3 - \lambda V_*(T) \quad (17)$$

is defined, where V_*^* is the operator conjugate to the operator V_* and $V_*(T) = v_*(T-t)$.

It follows from Eq. (17) that

$$u = (V_*^* V_* + \gamma_2)^{-1}[V_*^* y_2 - V_*^* V_* y_3 - \lambda v_*(T-t)], \qquad (18)$$

where $(V_*^* V_* + \gamma_2)^{-1}$ is the operator inverse to the operator $V_*^* V_* + \gamma_2$. As long as operator equation (17) written out in the nonabstract form represents the Volterra integral equation of the second kind, namely,

$$\int_t^T \int_0^s v_*(s-t)v_*(s-\tau)u(\tau)ds d\tau + \gamma_2 u$$
$$= \int_t^T v_*(s-t)y_2(s)ds$$
$$- \int_t^T \int_0^s v_*(s-t)v_*(s-\tau)y_3(s)ds d\tau - \lambda v_*(T-t), \quad (19)$$

the operator $(V_*^* V_* + \gamma_2)^{-1}$ is the resolvent of Eq. (19).

Let $z(T) = z'$ be a given and reasonably small intensity of the output signal of the receiver at the moment of time $t = T$ (in particular, $z' = 0$). In this case, as a result of substituting expression (18) into the condition $z(T) = z'$, we arrive at the linear algebraic equation with respect to λ:

$$\int_0^T v_*(T-t)y_3(t)dt$$

$$+ \int_0^T v_*(T-t)(V_*^*V_* + \gamma_2)^{-1}u_1(t)dt - z'$$

$$= \lambda \int_0^T (V_*^*V_* + \gamma_2)^{-1}v^2(T-t)dt. \tag{20}$$

Here, $u_1(t) = V_*^* y_2 - V_*^* V_* y_3$.

Equation (20) makes it possible to determine λ:

$$\lambda = \frac{\alpha - z'}{\beta}, \tag{21}$$

where

$$\alpha = \int_0^T v_*(T-t)y_3(t)dt$$

$$+ \int_0^T v_*(T-t)(V_*^*V_* + \gamma_2)^{-1}u_1(t)dt,$$

$$\beta = \int_0^T (V_*^*V_* + \gamma_2)^{-1}v_*^2(T-t)dt.$$

After substituting λ obtained from relationship (21) into formula (18), we arrive at the final expression for the optimal signal $u_*(t)$:

$$u_*(t) = (V_*^*V_* + \gamma_2)^{-1}\left[u_1 + \frac{z'-\alpha}{\beta}v_*(T-t)\right].$$

REFERENCES

1. L. D. Bakhrakh and M. Ya. Izrailovich, Dokl. Akad. Nauk **379**, 325 (2001) [Dokl. Phys. **46**, 491 (2001)].

2. L. D. Bakhrakh and M. Ya. Izrailovich, Dokl. Akad. Nauk **380**, 338 (2001) [Dokl. Phys. **46**, 647 (2001)].

3. L. D. Bakhrakh and M. Ya. Izrailovich, Antenny **5**, 26 (2002).

4. A. N. Tikhonov and V. A. Morozov, *Methods of Regularization of Ill-Posed Problems* (Nauka, Moscow, 1981).

5. R. Bellman, I. Glicksberg, and O. Gross, *Certain Aspects of Mathematical Theory of Control Processes* (RAND Rep. R-313, 1958; Inostrannaya Literatura, Moscow, 1962).

Translated by G. Merzon

=== TECHNICAL ===
PHYSICS

Shape Memory Effects
in FeNiCoTi Single Crystals
Undergoing γ ↔ α' Thermoelastic Martensitic Transformations

Yu. I. Chumlyakov[1,*], I. V. Kireeva[1], E. Yu. Panchenko[1],
E. G. Zakharova[1], V. A. Kirillov[1],
Corresponding Member of the RAS S. P. Efimenko[2], and H. Sehitoglu[3]

In Fe–Ni alloys undergoing γ ↔ α' martensitic transformations (MTs), where γ is the high-temperature fcc phase (austenite) and α' is the low-temperature bcc phase (martensite), temperature hysteresis $\Delta T \sim 300$–350 K is observed and such transformations are not thermoelastic [1–9]. A γ ↔ α' MT is nonthermoelastic due to large volume changes $\Delta V_{\gamma-\alpha'}$ responsible for the generation of crystal-structure defects, namely, dislocations arising during MTs [2–4, 9]. Precipitation of γ'-disperse $(CoNi)_3Ti$ particles in FeNiCoTi alloys, first, strengthens the γ phase and, consequently, suppresses plastic-flow processes during γ ↔ α' MTs. Second, γ'-disperse particles do not undergo MTs, they favor the accumulation of the elastic energy in martensite crystals, and modify the degree of tetragonality in α' martensite, and volume changes $\Delta V_{\gamma-\alpha'}$ become ≤1% [1–7].

As a result, γ ↔ α' MTs become thermoelastic, the shape memory effect and superelasticity are observed, and temperature hysteresis decreases down to 30–50 K [1–7, 9].

The aim of this study is to investigate the shape memory effect, superelasticity and the mechanical properties of Fe–Ni(29%)–Co(18%)–Ti(4%) (wt %) single crystals. First, it was expected that experiments with single crystals make it possible to avoid the influence of grains on γ → α' → γ MTs. Discontinuous decomposition processes at the final aging stages can be suppressed in single crystals. Therefore, MTs can be investigated in the absence of structural inhomogeneities associated with continuous decomposition inside the grain body and discontinuous decomposition at the grain boundaries [1–4]. Second, experiments with single crystals make it possible to check theoretical estimates of deformation during γ → α' MTs [5, 7].

The investigations were performed with single crystals with a [–111] tension axis and polycrystals with a grain size $d = 200$ μm in the Fe–Ni(29%)–Co(18%)–Ti(4%) (wt %) alloys. The crystals were grown in a helium atmosphere by the Bridgman method in MgO crucibles with the use of seeds. For tension experiments, the samples with a given orientation and $18 \times 3 \times 1.5$-mm working parts were cut out using an electrospark machine. After cutting, the damaged layer was removed by mechanical grinding and chemical etching in aqua regia. The dendritic structure of the samples was destroyed by homogenization at $T = 1473$ K for 24 h. The single-phase state was obtained by water quenching from 1423 K for one hour. All thermal treatments were performed in the helium atmosphere. The experimental details were described in [5, 7].

Figure 1a shows σ_{cr} as a function of aging time at $T = 823$–973 K for the single crystals with the [–111] tension axis under testing at room temperature. The start temperature M_s of the MT as a function of aging time in the range $T = 823$–973 K is presented in Fig. 1b. This temperature was determined by the method of differential scanning calorimetry (DSC) and from the temperature dependence of electrical resistivity $\rho(T)$. Figure 2 shows $\sigma_{cr}(T)$ for the single crystals and $\sigma_{0.1}(T)$ for the polycrystals of the Fe–Ni(29%)–Co(18%)–Ti(4%) alloy for three structural states. In Fig. 3, the results of investigating the shape memory effect in the single crystals are presented. As is seen in Fig. 1, the precipitation of disperse $(CoNi)_3Ti$ particles gives rise to an increase in σ_{cr} with aging time t. At $T = 823$ K, σ_{cr} increases considerably when $0 < t < 4$ h and, then, increases slowly when $t > 4$ h. At $T = 923$–973 K, $\sigma_{cr}(t)$

---

[1] *Siberian Physical Technical Institute,*
  Tomsk State University,
  pl. Novosobornaya 1, Tomsk, 634050 Russia

*e-mail: chum@phys.tsu.ru

[2] *Baĭkov Institute of Metallurgy,*
  Russian Academy of Sciences,
  Leninskiĭ pr. 49, Moscow, 117911 Russia

[3] *144 Mechanical Engineering Building,*
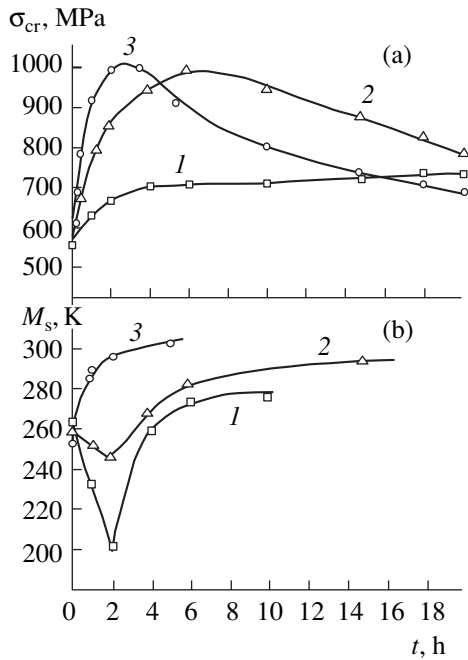 *1206 West Green Street, Urbana, IL 61801, USA*

Fig. 1. (a) σ_{cr} and (b) M_s as functions of aging time for the [–111] Fe–Ni(29%)–Co(18%)–Ti(4%) (wt %) single crystals that were aged at temperatures (*1*) 823, (*2*) 923, and (*3*) 973 K and were deformed at $T = 300$ K.

has a maximum. For slip deformation, the stage of increase in $\sigma_{cr}(t)$ is usually caused by the precipitation and growth of coherent particles that are cut out by slip
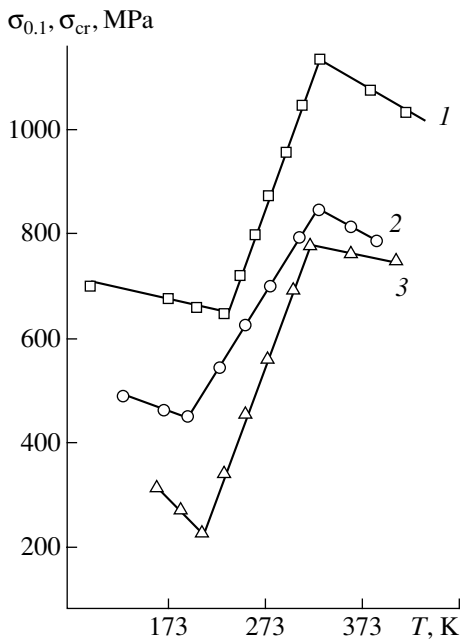
dislocations. A decrease in $\sigma_{cr}(t)$ is associated with overaging [8] and is usually explained by changing the deformation mechanism: instead of cutting disperse particles, dislocations begin to pass over them according to the Orowan mechanism.

In the FeNiCoTi single crystals undergoing MTs under loading, the dependence $\sigma_{cr}(t)$ at $T = 300$ K is determined by the development of the $\gamma \to \alpha'$ MT under loading rather than by the strength properties of austenite. Actually, it is seen in Figs. 1 and 2 that $T_{test} = 300$ K is below M_d for all structural states investigated in this study.

The temperature dependences of σ_{cr} and $\sigma_{0.1}$ consist of three physically different sections (Fig. 2). Of greatest interest is the section with the anomalous temperature dependence of deforming stresses, where σ_{cr} and $\sigma_{0.1}$ increase with T_{test} and which is associated with developing the $\gamma \to \alpha'$ MT under loading [9].

The minimum deforming stresses correspond to M_s found by the DSC method and from the $\rho(T)$ dependence (Fig. 2), while the maximum values are attained at the temperature M_d. At $T = M_d$, the stresses required to form martensite under loads σ_{cr} and $\sigma_{0.1}$ ($\gamma \to \alpha'$) are equal to the respective plastic-flow stresses σ_{cr}^{γ} and $\sigma_{0.1}^{\gamma}$. Consequently, at $T > M_d$, the temperature dependences $\sigma_{cr}^{\gamma}(T)$ and $\sigma_{0.1}^{\gamma}(T)$ of the onset of plastic flow are determined by the temperature dependence of
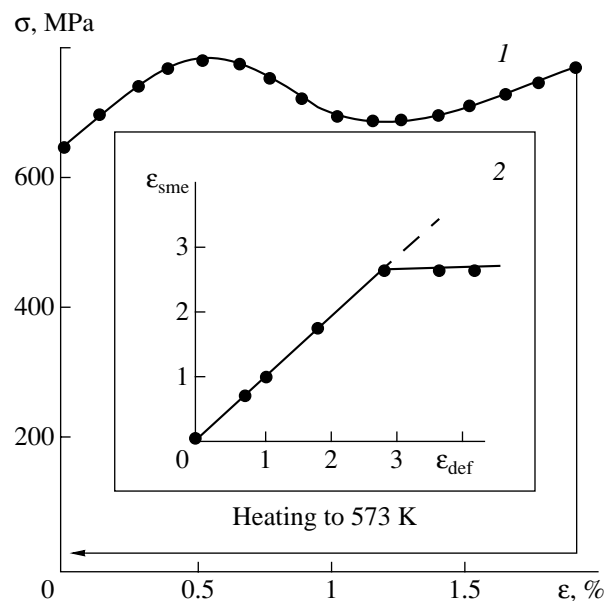

Fig. 2. Plots $\sigma_{cr}(T)$ for the single crystals and $\sigma_{0.1}(T)$ for the Fe–Ni(29%)–Co(18%)–Ti(4%) (wt %) polycrystals: (*1*) [–111] single crystals after annealing at 873 K for 4 h, (*2*) polycrystals after annealing at 873 K for 2 h, and (*3*) polycrystals after annealing at 823 K for 3 h.

Fig. 3. (*1*) The shape memory effect in the [–111] crystals of the Fe–Ni(29%)–Co(18%)–Ti(4%) (wt %) alloy; aging at 873 K for 4 h, deformation at $T = 233$ K, and annealing at 573 K for 0.5 h. (*2*) The shape memory effect ε_{sme} as a function of a given strain ε_{def} at 233 K; annealing at 573 K for 0.5 h.

dislocation motion in a structurally inhomogeneous alloy containing disperse particles of the γ' phase [1, 9]. Finally, under loading at $T < M_s$, cooling martensite is reoriented due to the motion of interfaces between α' martensite and twins in α'-martensite crystals [9].

From the aforesaid, it follows that the yield stress at $T = 300$ K cannot be used as a measure of the strength properties of the γ phase after aging, because the onset of plastic flow at such temperatures is associated with the formation of α'martensite rather than with the plastic deformation of the γ phase.

The yield stresses at $T = M_d$ for polycrystals and single crystals are shown in Fig. 2. Figure 1b shows M_s as a function of temperature and aging time. It is seen that, with an increase in aging time, $M_s(t)$ varies nonmonotonically at $T = 823–873$ K and increases at $T = 973$ K. The most considerable variations in $M_s(t)$, which are a decrease at $823–873$ K and an increase at $T = 973$ K, are observed for $t \leq 3$ when $\sigma_{cr}(T = 300$ K) and $\sigma_{cr}(M_d)$ increase significantly.

Such peculiar behavior of $M_s(t)$ and $\sigma_{cr}^{\gamma}(t)$ was previously observed in the experiments with polycrystals and single crystals of Ti–51 at. % Ni and in the polycrystals of aged Fe alloys [1–4, 9]. This behavior is associated with the influence of disperse particles on MTs in structurally inhomogeneous alloys. First, when $(CoNi)_3Ti$ particles precipitate, the concentrations of Ni and Co in the matrix decrease, which must give rise to an increase in M_s [1–4].

If only this fact determined the $M_s(t)$ dependence, M_s would always increase with t. Such behavior of $M_s(t)$ is observed only at $T = 923$ K and, consequently, the role of disperse particles at this temperature is reduced to decreasing the Ni and Co concentrations in the matrix. Second, the precipitation of disperse particles improves the strength properties of the matrix due to the effects of dispersion hardening (Figs. 1 and 2). This must provide additional resistance not only to the motion of slip dislocations but also to the motion of martensite–matrix interfaces, as well as to twinning dislocations in α'-martensite crystals [3]. Therefore, at the early aging stages for $T = 823–923$ K, M_s decreases because of significant dispersion hardening effects. The complex $M_s(t)$ dependence at $T = 823–923$ K is determined by competition between these two factors [1–4, 9].

Another important effect of disperse particles on MTs is the modification of temperature hysteresis $H = M_s - A_f$ and creation of the conditions for the thermoelastic MT. For example, in the single-phase state, when the crystal contains no disperse particles after hardening from $T = 1373$ K, H is equal to 300–400 K [1, 9]. Aging at 823–923 K for $t \leq 5$ h decreases hysteresis H to 80 K. The investigations indicate that, in hard-ened crystals, the $\gamma \leftrightarrow \alpha'$ transformation is nonthermoelastic and the shape memory effects are not observed. On the contrary, crystals aged at 823–923 K for 2 h undergo thermoelastic $\gamma \leftrightarrow \alpha'$ MTs [5, 7] associated with the shape memory effect (Fig. 3). In [–111] crystals, the maximum shape memory effect is equal to 2.5%, which is close to strains calculated theoretically for $\gamma \leftrightarrow \alpha'$ MTs [5, 7].

When analyzing the conditions for superelasticity, it is necessary to take into account the following circumstances. First, the dependences $\sigma_{cr}(T)$ and $M_s(t)$ show that, for all structural states being investigated, the temperature M_d is less than A_f [5, 7]. Therefore, α' martensite thermodynamically unstable under unloading cannot be obtained in these alloys under loading. Second, stresses needed for the formation of martensite under loading for $M_s < T < M_d$, as well as stresses needed for reorientation of martensite–martensite interfaces for $77 < T < M_s$, appear to be high (Fig. 2). Consequently, the conditions for superelasticity associated with arising $\gamma \leftrightarrow \alpha'$ MTs under loading are not created. The experimental investigation corroborates these suggestions, and superelasticity in these alloys was not found.

To create the conditions for arising superelasticity associated with $\gamma \leftrightarrow \alpha'$ MTs under loading, it is necessary to decrease A_f below M_d due to decreasing temperature hysteresis H. In addition, the stresses required for the formation of martensite at $T = M_s$ should be decreased, and the phenomenological condition for

superelasticity $\dfrac{\sigma_{cr}(M_d)}{\sigma_{cr}(M_s)} \geq 5–7$ must be fulfilled [9].

This means that plastic flow in the γ phase is absent when martensite is formed under loading. Experimentally, such conditions can be reached by both increasing the volume fraction of the γ' phase and replacing nickel with cobalt [1–7].

Thus, precipitation of disperse particles in Fe–Ni(29%)–Co(18%)–Ti(4%) (wt %) single crystals modifies the kinetics of the $\gamma \leftrightarrow \alpha'$ MT from nonthermoelastic in the single phase state to thermoelastic in the aged state. The temperatures of the MT, as well as thermal hysteresis, are controlled by varying aging regimes.

Experimentally, it is shown that the dependences $\sigma_{cr}(T)$ and $\sigma_{0.1}(T)$ in the FeNiCoTi single crystals and polycrystals of the alloy are similar to those for alloys undergoing martensitic transformations under loading. The shape memory effects measured for the [−111] aged single crystals are close to those calculated theoretically.

REFERENCES

1. V. V. Kokorin, *Martensitic Transformations in Heterogeneous Solid Solutions* (Naukova Dumka, Kiev, 1987).
2. N. Jost, Mater. Sci. Forum **56**–**58**, 667 (1990).
3. E. Hornbogen, Acta Metall. **33**, 595 (1985).
4. E. Hornbogen and N. Jost, J. Phys. IV **1**, C4-199 (1991).
5. H. Sehitoglu, I. Karaman, X. Zhang, *et al.*, Scr. Mater. **44**, 778 (2001).
6. V. V. Kokorin, Y. I. Samsonov, L. F. Khshanovsky, *et al.*, Phys. Met. Metallogr. **71**, 141 (1991).
7. H. Sehitoglu, X. Zhang, T. Kotil, *et al.*, Metall. Mater. Trans. A **33**, 3661 (2002).
8. E. Nembach, *Particle Strengthening of Metals and Alloys* (Wiley, New York, 1997).
9. K. Otsuka and C. M. Wayman, *Shape Memory Materials* (Cambridge Univ. Press, Cambridge, 1998).

Translated by Yu. Vishnyakov

=========================== **PHYSICS** ===========================

Quality of Focusing Electromagnetic Radiation by a Plane-Parallel Slab with a Negative Index of Refraction

Corresponding Member of the RAS A. N. Lagarkov and V. N. Kisel'*

The quality of focusing a field by a plane-parallel slab made of a material with permittivity and permeability $\varepsilon = \mu \approx -1$ is analyzed. Fields produced by one or two current filaments that are located near the slab are considered. Causes limiting the available resolution of the system are determined.

The unique properties of materials with simultaneously negative real parts of ε and μ (including the possibility of focusing radiation from point-like sources by a plane-parallel slab) were predicted by Veselago as early as the late 1960s [1]. Various variants of the practical realization of composites (so-called metamaterials) with such effective parameters have recently been proposed [2–5], and potential fields of their application are discussed. Focusing electromagnetic field energy fluxes in the presence of left-handed materials (LHMs) is also discussed. This problem is of particular importance in view of the outstanding idea by Pendry [6] that a plane-parallel slab of an LHM under certain conditions ($\varepsilon = \mu = -1$) can serve as a superlens with unique focusing properties such that its resolution is not limited by the well-known diffraction limit involving wavelength. According to [6], for $\varepsilon = \mu = -1$ the "perfect" image of a point-like source can be obtained due to both multiple reflections of the wave between surfaces of the LHM slab and the assumed enhancement of those components (evanescent modes) of the electromagnetic radiation spectrum which decrease exponentially with the distance from the source in a convenient medium. Opponents of this statement pointed out that transmittance and reflectance for evanescent modes for $\varepsilon = \mu = -1$ are divergent, "which excludes the possibility of the transmission of a evanescent wave into such a semi-infinite LHM" [7]. Instead of evanescent oscillation, Garcia and Nieto-Vesperinas [7] analyzed the possibility of a solution in the form of a wave increasing exponentially in the LHM with the distance from a source or an interface.

For such a wave, the reflectivity and penetrability are equal to 0 and 1, respectively. However, this electromagnetic process is energetically possible only in a medium (slab) of limited thickness. As was pointed out in [7], "although evanescent waves become amplifying in an ideal lossless dispersionless LHM slab, the width of this slab is limited and the recovery of these waves is physically meaningless because it requires infinite energy." Thus, this and other conclusions of [7] call into question the results obtained in [6]. A brief review of recent works [8] shows that the possibility of overcoming the diffraction limit remains an open problem.

This work aims to determine conditions under which the resolution can be increased (as compared to traditional systems) by focusing with an LHM slab. Such focusing is achieved due to the negative index of refraction of a plane wave at the interface between convenient and LHM substances.

Our results show that the image (focusing) quality can in principle be improved in the presence of a LHM slab. Overcoming the diffraction limit in the LHM is not associated with enhancement of usually evanescent spatial harmonics as the distance from a source increases (as is commonly accepted). This effect is associated with both the accumulation of reactive energy and an increase in the field amplitude near the interface between the exterior space and LHM. From a solution to a model problem, it is easily seen that energy is also accumulated near the interface when a current filament excites the infinite planar interface between half-spaces. This effect is responsible for the divergence of expressions for the reflection and penetration coefficients of evanescent oscillations for $\varepsilon = \mu \to -1$.

We consider excitation of an infinite plane-parallel slab (Fig. 1) by an in-phase filament with a current of amplitude I_0. As usual, the field inside the slab is represented as the set of harmonics that propagate or decrease exponentially with the distance from sources, which are equivalent surface currents at interfaces. Taking into account boundary conditions, we obtain analytical expressions for the vector potential, which is proportional to the electric field amplitude. For $x > a$ (i.e.,

_____

Institute of Theoretical and Applied Electrodynamics, Institute of High Temperatures Scientific Association (IVTAN), Russian Academy of Sciences, Izhorskaya ul. 13/19, Moscow, 125412 Russia
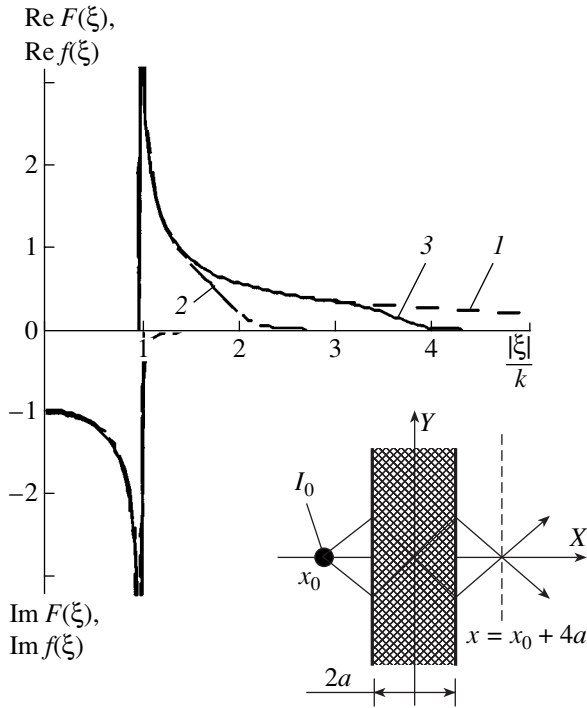* *e-mail: kis_v@mail.ru, kis@eldyn.msk.ru*

Fig. 1. Geometry of the problem of excitation of an infinite LHM slab and the spectral density of the field vector potential in the cross section passing through the focusing point.

in the half-space containing the focusing point), these expressions are written in the form

$$A = \frac{I_0}{4\pi} \int\limits_{-\infty}^{+\infty} \exp(-i\xi y) F(\xi) d\xi,$$

where

$$F(\xi) = \frac{-4\mu q \exp(q_0(x_0-x))\exp(2aq_0)}{(\mu q_0 - q)^2 \exp(-2aq) - (\mu q_0 + q)^2 \exp(2aq)},$$

$$q_0 = \begin{cases} i(k_0^2 - \xi^2)^{1/2}, & |\xi| \le \mathrm{Re}(k_0) \\ (\xi^2 - k_0^2)^{1/2}, & |\xi| > \mathrm{Re}(k_0), \end{cases}$$

$$q = \begin{cases} i(k^2 - \xi^2)^{1/2}, & |\xi| \le \mathrm{Re}(k) \\ (\xi^2 - k^2)^{1/2}, & |\xi| > \mathrm{Re}(k), \end{cases}$$

k_0 and $k = k_0\sqrt{\varepsilon}\sqrt{\mu}$ are the propagation coefficients of the exterior space and slab material, respectively; x_0 is the filament coordinate; $2a$ is the slab thickness; time-dependence is taken in the form $\exp(i\omega t)$; and principal values of radicals are used (the correct choice of branches of multivalued functions was discussed in [9]). Perfect focusing obviously means that the func-

tion $F(\xi)$ in the above Fourier integral must be equal to the spectral density of the vector potential of the linear source $f(\xi) = \dfrac{1}{q_0}$ in a certain vicinity of the focusing point (at least within the resolution area of traditional systems).

Let the source be located at the point $x_0 = -2a$ (Fig. 1). We compare the function $F(\xi)$ in the assumed focusing plane $x = 2a$ with $f(\xi) = \dfrac{1}{q_0}$ (line *1* in Fig. 1). Calculations show that $F(\xi)$ can truly be close to $f(\xi)$. Moreover, if losses in the slab are negligibly small (vanish), the direct substitution $\varepsilon = \mu \rightarrow -1$ yields $F(\xi) \rightarrow f(\xi)$, which means that a perfect image is obtained in the plane under consideration. However, further analysis shows that in the presence of even very small losses in the dielectric ($\varepsilon'' = -\mathrm{Im}(\varepsilon) > 0$, $\mu'' = -\mathrm{Im}(\mu) > 0$) only the approximate equality $F(\xi) \approx f(\xi)$ can be achieved, which is valid in a limited interval of the infinite integration range in ξ. The function $F(\xi)$ decreases rapidly with increasing $|\xi|$ above a certain value. In particular, for $\mu = -1$ and $\varepsilon = -1 - i\alpha$, where $\alpha \ll 1$, we obtain the asymptotic representation $F(\xi) \approx f(\xi)(1 + \Delta)^{-1}$, where $\Delta = \alpha^2(2q_0)^{-4}\exp(4aq_0)$. Therefore, the spectral density $F(\xi) \rightarrow 0$ vanishes exponentially for large ξ values at any $\alpha > 0$. With an increase in the slab thickness a entering into the exponent, the ξ value at which $F(\xi) \approx 0$ obviously decreases (parameters $x_0 = -2a$ and $x = 2a$ change with varying slab thickness).

Taking the closeness criterion of $F(\xi)$ to $f(\xi)$ (e.g., limiting relative error), one can determine the value ξ_0 such that $F(\xi) \approx f(\xi)$ for $|\xi| < \xi_0$ for given parameters of the problem. Since the spectral density $F(\xi)$ decreases rapidly for $|\xi| > \xi_0$, the values $-\xi_0$ and $+\xi_0$ are the limits of the spectrum of spatial harmonics forming the image. The detailing of the image is associated with the completeness of the spectrum of modes taken into account—in particular, the size of the focal spot is inversely proportional to $\tilde{\xi}_0 = \dfrac{\xi_0}{|k|}$. Therefore, the limiting resolution of the system is determined by the achieved $\tilde{\xi}_0$ value. To obtain the perfect image of a point-like source, all evanescent modes obviously must be included, which can be done only at $\tilde{\xi}_0 \rightarrow \infty$. For $\tilde{\xi}_0 = 1$, convenient quality focusing is achieved. In this case, evanescent harmonics are lost and the image is formed only by propagating oscillation modes for which $-1 < \dfrac{\xi}{k} < 1$. The common feature of all intermediate variants for $1 < \tilde{\xi}_0 < \infty$ is the improvement of focusing properties and resolution compared to the diffraction limit. These $\tilde{\xi}_0$ values are realized in a system with a plane-parallel LHM slab with small losses.
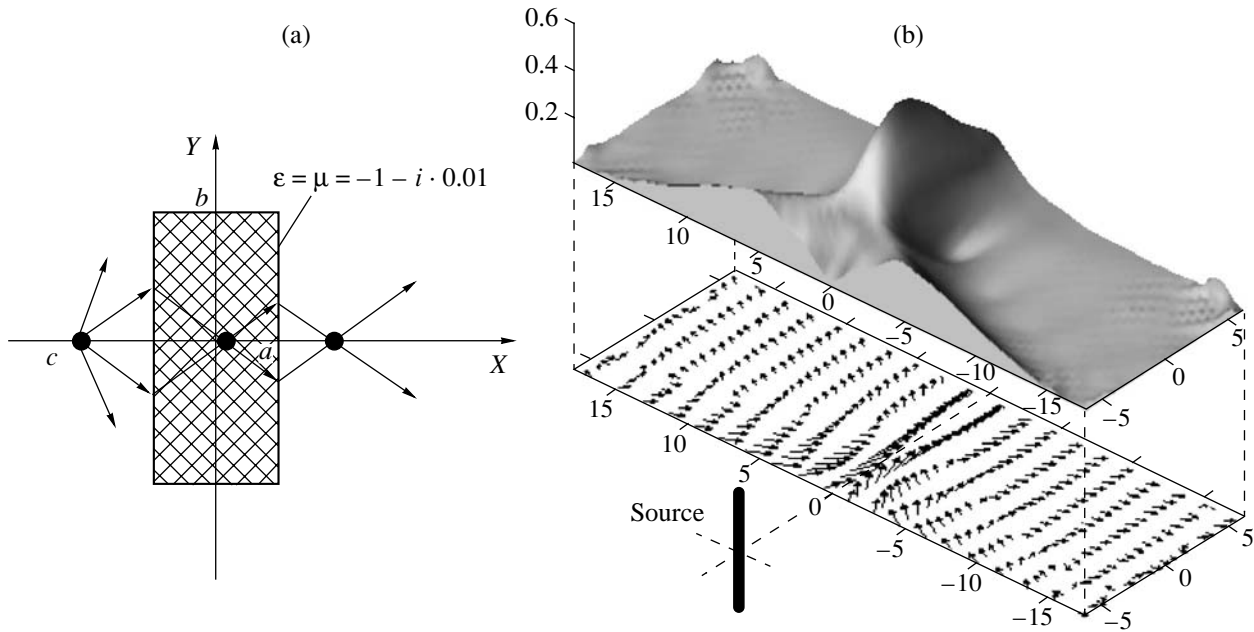
Fig. 2. (a) Cross-section of the slab with the ray scheme and (b) calculated distribution of the real part of the Poynting vector inside the slab.

However, calculations show that requirements on LHM quality are very high for slab thickness comparable with the wavelength. In particular, for $\varepsilon'' = \mu'' = 0.01$ and thickness $2k_0a = 3.0$ (about half the wavelength), $\tilde{\xi}_0$ is equal to 1.5 (line *2* in Fig. 1). To achieve $\tilde{\xi}_0 \approx 3$ for the same geometry of the problem, losses must be reduced to $\varepsilon'' = \mu'' = 0.00005$ (line *3* in Fig. 1), which is hardly achievable. For a thicker slab, $\tilde{\xi}_0$ are smaller (e.g., for figures discussed below, where $2k_0a = 13.2$ and $\tilde{\xi}_0 \approx 1$). We note that small losses in the dielectric do not catastrophically affect the amplitudes of propagating harmonics (Fig. 1, $\frac{\xi}{|k|} < 1$). Therefore, it is easier to detect normal quality focusing for the slab thickness under consideration. At the same time, the application of thin LHM slabs (with a thickness of several hundredths of the wavelength) strongly reduces requirements on losses and enables one to hope that the superresolution effect can be practically used after the corresponding advance in the technology of thin metamaterials.

The conclusions on the physical pattern and the focusing quality of the image of a point-like source were also verified by other methods. In particular, excitation of a finite-thickness slab by two parallel filaments of in-phase current was considered. The slab parameters $\varepsilon = \mu \approx -1$ are taken into account in expressions of polarization currents in the slab bulk. Then, the system of volume integral equations for field components in a dielectric is obtained by using the Green's function of the free space. This system is solved numerically. Thus, focusing, field concentration near the slab surfaces, and estimates of resolution are corroborated without the concept of the propagation coefficient of the LHM and exponentially evanescent or increasing oscillation modes (the primary field of sources was directly expressed in terms of Hankel functions). Moreover, the problem of choosing the correct sheet of the Riemann surface was overcome, because calculations of multivalued functions whose arguments involve negative ε and μ values were not necessary. Finally, the model of a finite-thickness slab is more realistic and provides an insight into the edge effects on the results.

Figures 2 and 3 show the results for the structure whose cross-section in the $z = 0$ plane is shown in the left panel of Fig. 2 ($2k_0a = 13.2$, $2k_0b = 21.6$, $k_0c = -14.0$, where k_0 is the propagation coefficient of the free space). Excitation is provided by one or two current filaments that are located symmetrically at distance d from each other and are parallel to the slab at the same distance $|c - a|$ from it. The right panel of Fig. 2 shows the relief of the absolute value of the real part of the Poynting vector inside the slab and its distribution when exciting by one current filament. It is seen that the lines of the Poynting vector are primarily directed along rays shown in the geometric optical approximation.

Figure 3 shows the relief of the absolute value of the electric field E_z inside and near the slab for various distances between two filament sources ($k_0d = 0, 4, 5$). It can be seen that the regions of the local field concentration are quite smeared and images of two spaced
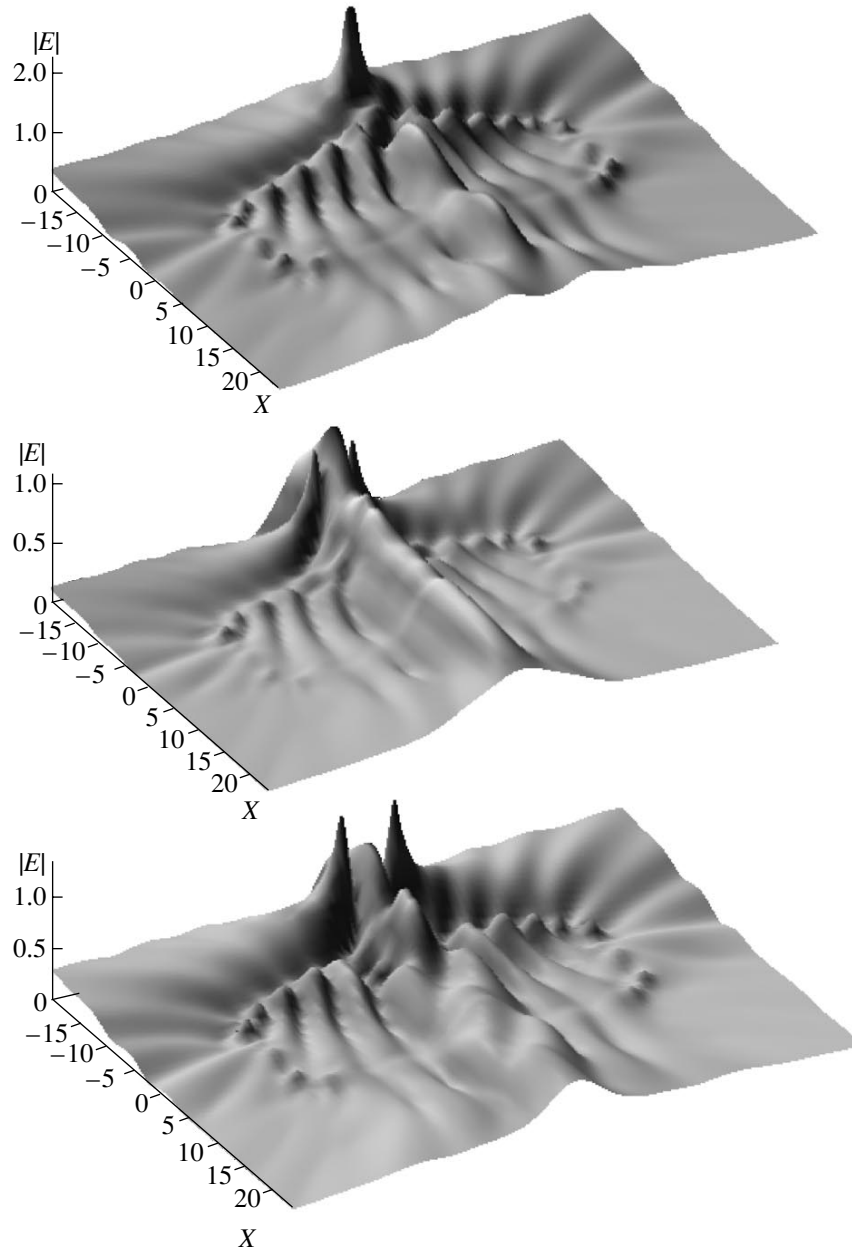
Fig. 3. Relief of the absolute value of the electric field inside and near the slab for various distances between sources.

sources are manifested separately from each other only when the distance between them slightly exceeds half the wavelength. We note that an increase in the slab length along the *Y* axis (Fig. 1) only slightly affects the results. We point out the previously mentioned feature of the diffraction pattern such as the appearance of high electromagnetic field values that are located near the interface between media traditional and LHMs and are associated with the accumulation of the energy of evanescent modes. In Fig. 3, this feature is manifested in the series of peaks with maxima on the slab surface (which are particularly pronounced for $x = \text{const} = -a$).

These peaks also arise when an infinite LHM slab or plane interface between half-spaces is excited. Thus, areas of local concentration of electromagnetic energy arise inside the plane-parallel slab and near it in the vicinity of the crossing points of refracted rays. The energy transfer direction generally corresponds to the ray representation. However, the sizes of these areas and resolution of the system (smallest distance between sources, at which their images are distinguishable) are no better than the properties of the convenient focusing systems in the presence of such a small loss ($\varepsilon'' = \mu'' = 0.01$).
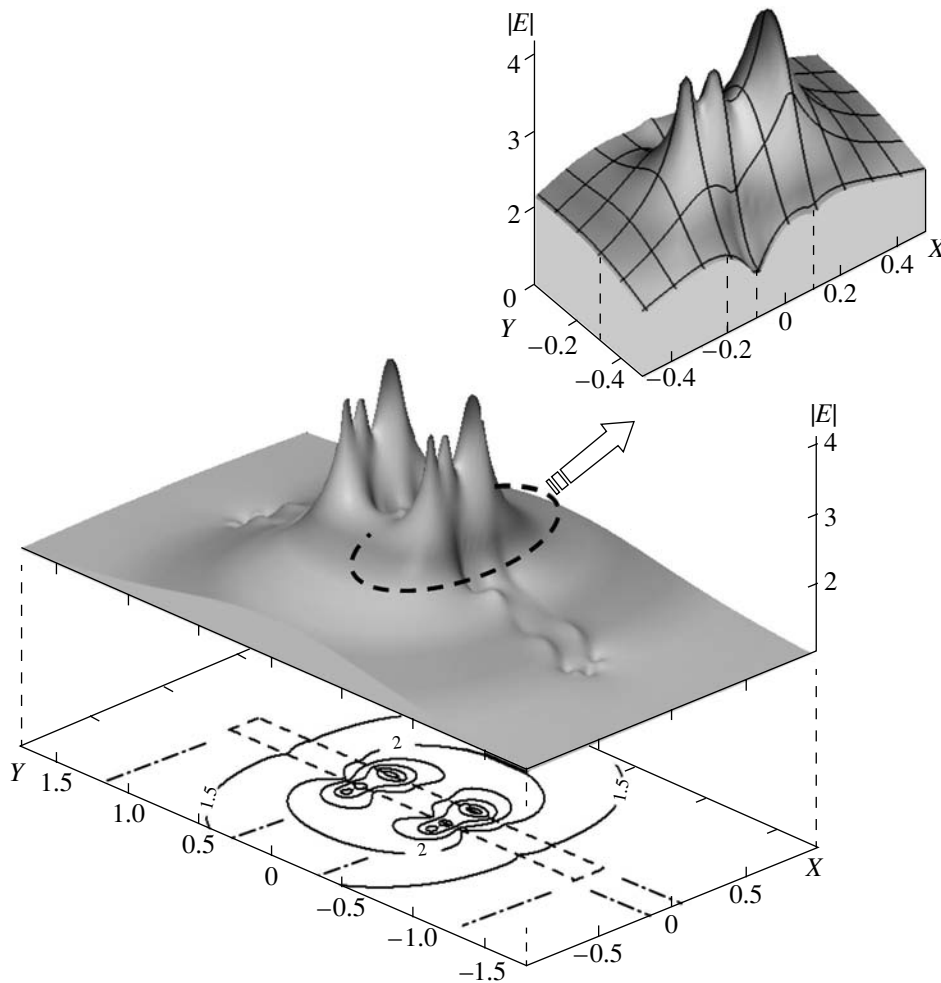
Fig. 4. Relief of the absolute value of the electric field from two sources located near the thin slab.

As was mentioned above, a system based on a thin LHM slab has much better properties. In particular, even for comparatively large losses in an LHM when $\varepsilon'' = \mu'' = 0.1$, distinct separate images of sources spaced by about one tenth (!) of the wavelength can be obtained. This conclusion is supported by calculations by the method of volume integral equations (Fig. 4) for $2k_0a = 0.2$, $2k_0b = 2.4$, $k_0c = -0.2$, and $k_0d = 0.6$. Peaks corresponding to the maximum field amplitude on the front and back surfaces of the slab are clearly visible in the figures.

Separate images of linear sources spaced by 20 or 30 mm (the radiation wavelength was equal to 175 mm) were obtained in our experiments with a 7-mm-thick slab of a composite material with the effective properties of an LHM. Thus, the above conclusions are experimentally corroborated.

In conclusion, we point out one more circumstance. The condition $F(\xi) \approx f(\xi)$ provides high resolution only when an image is detected as a cross section in an $x =$ const plane parallel to the slab. Similar results can be obtained in an orthogonal $y =$ const plane only when the spectral density of the vector potential depends correspondingly on x; i.e., at least a local maximum of the spectral density of evanescent harmonics must be located at the focusing point. However, for $x > a$ the spectral density of evanescent harmonics decreases monotonically with increasing x, which excludes perfect focusing behind the LHM slab [6]. Thus, a superlens cannot reproduce a finite-depth scene with superresolution. However, when a source (filament) is located at the point $x_0 = 3a$, its image arises directly on the unilluminated surface of the slab and special conditions for focusing appear. In this case, a sharp peak of the field-amplitude distribution along both x and y coordinates can be obtained, because, first, a local maximum of the spectral density of evanescent harmonics is achieved and, second, the phase velocity of propagating waves is directed from the focusing point over the entire angular sector. This conclusion is supported by calculations of the field near and inside the slab.

Thus, the enhancement of nonpropagating harmonics should not be treated as an increase in the amplitude of these harmonics with the distance from a source,

which seemed to be inherent in an LHM. Nevertheless, the amplitudes of evanescent modes can be high enough to overcome the diffraction limit due to accumulation of their energy near the interface between the outer space and LHM. Practical application of the effect requires LHM with small losses. Focusing is close to perfect if the focal plane coincides with the slab surface.

REFERENCES

1. V. G. Veselago, Usp. Fiz. Nauk **92**, 517 (1967).

2. D. R. Smith, W. Y. Padilla, D. C. Vier, *et al.*, Phys. Rev. Lett. **84**, 4184 (2000).

3. A. N. Lagarkov, V. N. Semenenko, V. A. Chistyaev, *et al.*, Electromagnetics **17**, 213 (1997).

4. A. N. Lagarkov, V. N. Semenenko, V. N. Kisel, *et al.*, J. Magn. Magn. Mater. **258**–**259**, 161 (2003).

5. G. V. Eleftheriades, A. K. Iyer, and P. C. Kremer, IEEE Trans. Microwave Theory Tech. **50**, 2702 (2002).

6. J. B. Pendry, Phys. Rev. Lett. **85**, 3966 (2000).

7. N. Garcia and M. Nieto-Vesperinas, Phys. Rev. Lett. **88**, 207403 (2002).

8. R. Bansal, IEEE Antennas Propag. Mag. **44** (5), 103 (2002).

9. V. N. Kisel' and A. N. Lagarkov, Élektromagn. Volny Élektron. Sist. **7**, 62 (2002).

Translated by R. Tyapaev

Distribution and Variations of Galactic Cosmic Rays in the Heliosphere According to Meteorite Data

V. A. Alexeev, V. D. Gorin, and G. K. Ustinova
Presented by Academician É.M. Galimov July 24, 2003

Investigation of heliosphere, i.e., the sphere of manifestation of solar activity, is one of the most important areas of research in modern space physics. A remarkable feature of the solar activity is its cyclicity, i.e., the quasi-periodic appearance and development of active regions. The most obvious example of manifestation of the solar cycle is a variation in the number R_i of sunspots with the average period of ~11 years (Fig. 1). A striking example of the effect of the solar activity on processes occurring in the heliosphere is the modulation of galactic cosmic rays (GCRs) by the solar wind in the vicinity of the Earth: the intensity of GCRs can decrease by an order of magnitude, remaining in anticorrelation with the solar activity (see the results of long-term probing of the stratosphere [1] presented in Fig. 1). In standard models describing the modulation of GCRs crossing the solar wind, their flux is affected by the action of various processes. These are transport processes of diffusion through turbulent magnetic fields, convective processes associated with magnetic fields frozen into the solar wind, and the cooling caused by the expansion of the solar wind volume with distance from the Sun [2, 3]. It is natural to expect that the boundary of the GCR modulation region corresponds to the dynamic boundary between the solar wind and the interstellar gas. The position of this boundary can be estimated provided that the GCR intensity gradients in the heliosphere are known. In order to separate, wherever possible, the galactic component of cosmic rays from the solar component, spacecraft, in most cases, were launched in years of minimal solar activity, when the intensity level of GCRs in the heliosphere was the highest. The results obtained invariably led to small [on the order of ~2–4% per astronomical unit (AU)] gradients of GCRs with an energy of $E \geq 100$ MeV. Under the assumption that the modulating properties of the heliosphere are practically the same at different dis-

tances from the Sun, this testifies to vast (>100 AU) sizes of the modulation region [4]. Indeed, by virtue of overlapping temporal and spatial variations of GCR, measurements of their intensity by the *Pioneer 10* and *Voyager 1* and *2* spacecrafts in remote parts of the heliosphere (~20–50 AU) resulted in small values of gradients even in years of maximum solar activity [5]. Moreover, measurements performed near the ecliptic plane in the interior heliosphere (≤ 5 AU) did not yield reliable information on the existence of latitudinal gradients of the GCR intensity.

A fundamentally new stage in studies of the heliosphere is associated with the launch in October 1990 of the *Ulysses* spacecraft in a polar orbit. It was found [6] that the radial gradients of protons with an energy $E > 2$ GeV in the interior heliosphere increase by at least several times with the growth of solar activity. By contrast, the latitude gradients turned out to be significant in the years of the minimum of the 22th solar cycle and decreased to practically zero in the southern latitudes with the development of the 23rd cycle in 1998–2001. However, in this case, the heliocentric distance of the Ulysses spacecraft also decreased from 3 to 1.5 AU [7]. Are these regularities transient or do they have a general character? The answer to this question is crucial for many conclusions concerning features of the distribution and variations of GCRs in the heliosphere, in particular, regarding properties and sizes of the modulation region. At present, the necessary information on the character of these processes in the three-dimensional heliosphere over four solar cycles can be obtained only from meteorite data.

The method of using meteorites with different inclination and extent of their orbits as probes of cosmic ray variations in the heliosphere was proposed and developed in [8]. Indeed, cosmogenic nuclides produced in meteorites and having different decay half-periods $T_{1/2}$ are natural detectors of cosmic rays along the meteorite orbits for a time of about $1.5T_{1/2}$ for a radioactive nuclide prior to the fall of the meteorite to Earth. Measuring the activity of the radioactive nuclide at the moment of the meteorite landing, we can evaluate the average intensity I_r of cosmic rays, which corresponds to the production of radioactive nuclides at the average

Vernadskiĭ Institute of Geochemistry and Analytical Chemistry, Russian Academy of Sciences, ul. Kosygina 19, Moscow, 117975 Russia
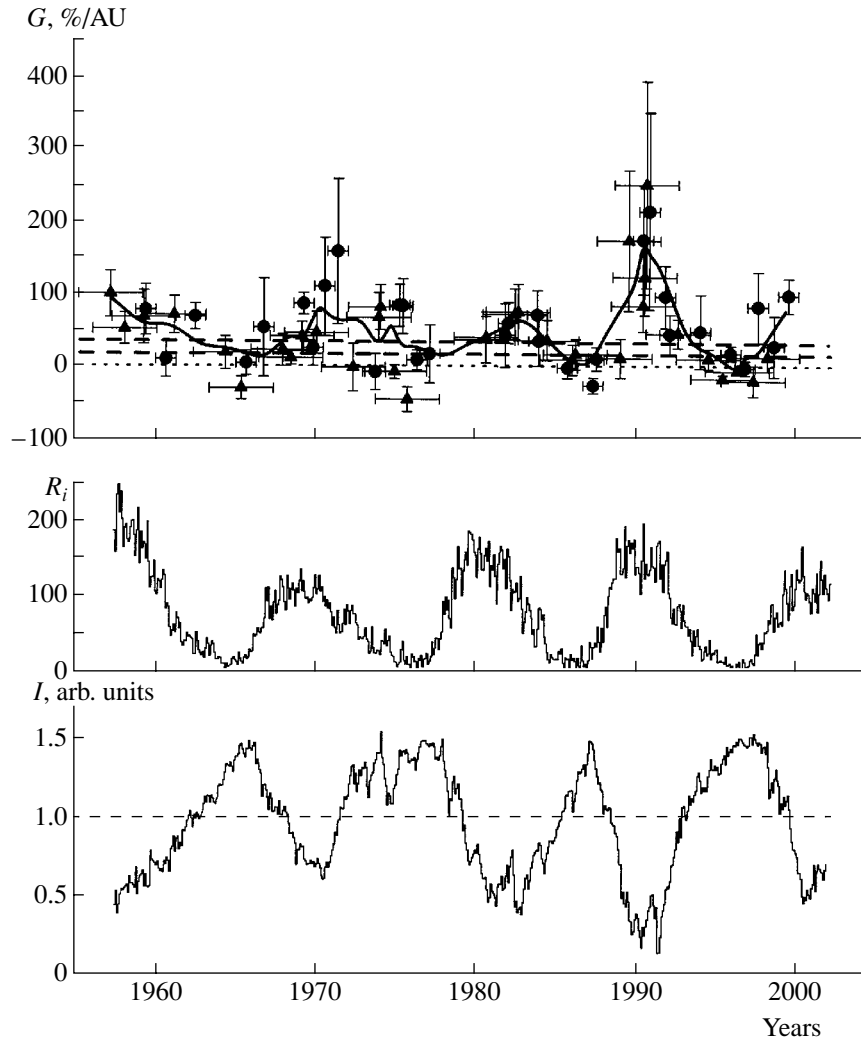*e-mail: aval@icp.ac.ru; ugeochem@geochem.home.chg.ru; ustinova@dubna.net.ru*

Fig. 1. Distribution and variation of radial gradients G_r ($R \geq 0.5$ GV) for GCRs in the heliosphere in 1955–2000 according to meteorite data and variations in the sunspot number R_i [12] and intensity I (arbitrary units) of GCRs in the stratosphere (probing measurements of [1]). The values of GCR gradients were obtained in accordance with data on the radioactivity of ^{54}Mn (circles), ^{22}Na (triangles), and ^{26}Al (dashed horizontal lines at 20–30%/AU) in 33 chondrites that fell to Earth in 1959–2000.

heliocentric distance r of the meteorite during the time $\sim 1.5 T_{1/2}$. Furthermore, comparing the quantity I_r with the measured average intensity I_1 at the distance of 1 AU in the same period of time (according to the data of [1] for the stratosphere), we can evaluate the radial gradients G_r (in percent per astronomical unit) using the formula

$$G_r(R > R_0) = \frac{\dfrac{I_r}{I_1} - 1}{r - 1} \times 100\%,$$

where R is the rigidity (expressed in GV) of cosmic ray particles. In the Earth's atmosphere, the ablation of meteorites takes place. Therefore, on the average, in stone meteorites (chondrites), only layers of radionuclides with a screening of ≥ 10 cm are available for measurements, which corresponds to the particle rigidity

$R \geq 0.5$ GV. Studying radionuclides with various decay half-periods $T_{1/2}$ in chondrites with different fall dates, as well as different extent and inclination of their orbits, we can obtain a continuous set of data related to the distribution and variations of GCRs having rigidities $R \geq 0.5$ GV in the three-dimensional heliosphere. The radionuclides most efficient for realizing this goal are ^{54}Mn ($T_{1/2}$ = 300 days), ^{22}Na ($T_{1/2}$ = 2.6 years), and ^{26}Al ($T_{1/2}$ = 7.4 × 10^5 years). They contain information on the average intensity of GCRs along the chondrite orbits (aphelion $q' \sim$ 2–4 AU [8]) over ~450 days, ~4 years, and 1 million years, respectively, prior to the fall of the chondrites to Earth.

Figure 1 shows the data we obtained on the radial gradients of GCRs having $R > 0.5$ GV along the orbits of the following chondrites (the dates of meteorite falls to Earth and the aphelion q' expressed in astronomical
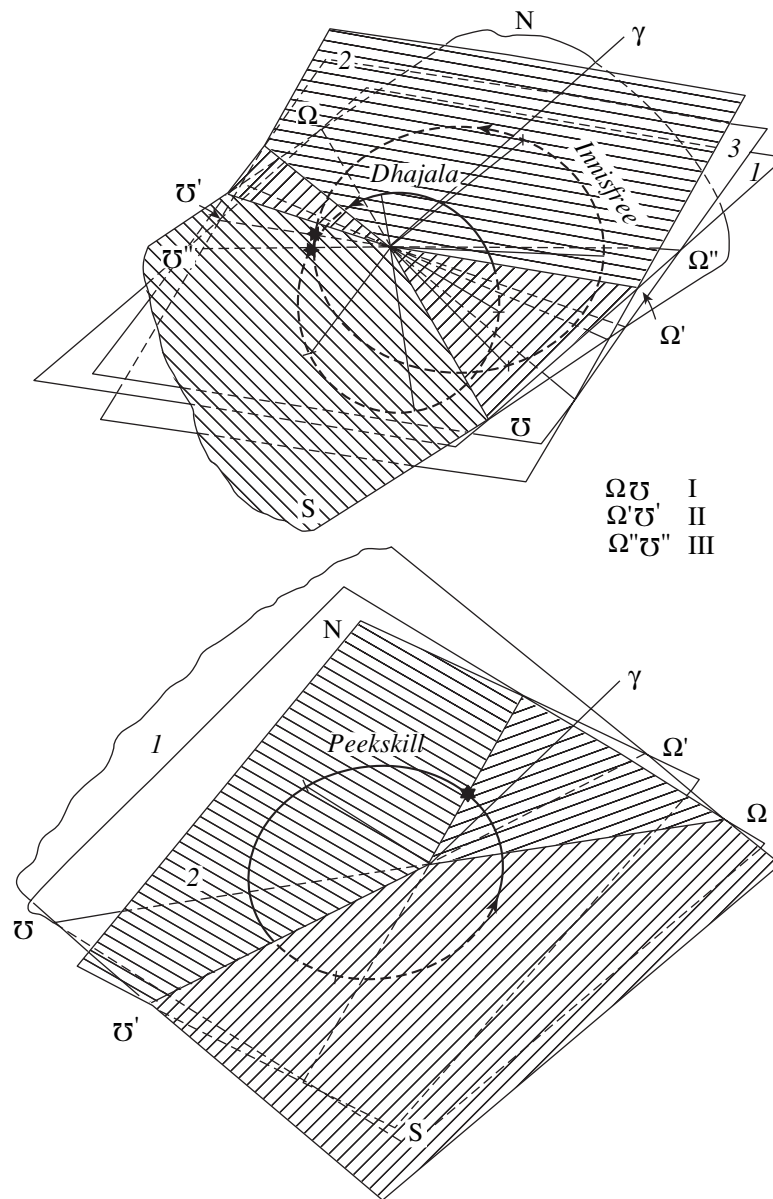
Fig. 2. The different character of the inclinations of the orbit plane for the Dhajala, Innisfree, and Peekskill chondrites to the ecliptic plane (*1*) and the helioequatorial plane (N–S); (*2*) the orbit planes for the Dhajala and Peekskill chondrites; (*3*) the orbit plane for the Innisfree chondrite. I, II, and III are the lines of solar nodes for the Dhajala, Peekskill, and Innisfree chondrites, respectively; γ is the point of the spring equinox; the dashes in the orbits mark average heliocentric distances of the chondrites.

units are indicated in parentheses): Pribram (Apr. 7, 1959; 4.05); Bruderheim (Mar. 4, 1960; 4.06); Harleton (May 30, 1961; 1.90); Peace River (Mar. 31, 1963; 2.04); St. Severin (June 27, 1966; 1.97); Denver (July 15, 1967; 2.10); Lost City (Jan. 3, 1970; 2.35); Malakal (Aug. 15, 1970; ≥4); Kabo (Apr. 25, 1971; 2.60); Guibga (Feb. 26, 1972; 2.10); Gorlovka (July 17, 1974; ~1.9); Dhajala (Jan. 28, 1976; 2.25); Jilin (Mar. 8, 1976; 2.17); Innisfree (Feb. 5, 1977; 2.76); Kutais (Nov. 28, 1977; 1.98); Gujargaon (Sept. 4, 1982; ≤1.9); Wethersfield (Nov. 8, 1982; 2.37); Tomiya (Aug. 22, 1984; 2.09); Binningup (Sept. 30, 1984; 1.81); Kokubunji (July 29, 1986; 1.93); Trebbin (Mar. 1, 1988; 1.97); Torino (May 18, 1988; 2.17); Tahara (Mar. 26, 1991; 1.92); Noblesville (Aug. 31, 1991; 1.92); Mbale (Aug. 14, 1992; 2.51); Peekskill (Oct. 9, 1992; 2.10); Mihonoseki (Dec. 10, 1992; 1.95); Coleman (Oct. 20, 1994; 3.12); Fermo (Sept. 25, 1996; 1.97); El Hammami (Aug. 10, 1997; ≥4); Kunya-Urgench (June 20, 1998; ~4); Hassilabyade (June 15, 1999; 1.90); and Moravka (May 6, 2000; 1.95). The curve in Fig. 1 is a result of smoothing the experimental data by the first-power polynomial over five points [9]. Comparing these results with the variation curve for sunspot numbers, we can clearly see that the values of the gradients strongly depend on the phase of the solar

cycle. They change from small and even negative values in the years of minimal solar activity (which is consistent with direct observations in the interplanetary space [4]) to values exceeding 100% per astronomical unit in the years of maximal activity. The average gradients (~20–30% per astronomical unit) for modern solar cycles coincide with those for the last million years, which follows from the analysis of ^{26}Al content in chondrites with known orbits [8]. This testifies to steadiness of the mechanism of the solar modulation of GCRs for at least ~1 million years.

It should be noted that gradients of GCRs, which follow from meteorite data, are related to different heliocentric distances (1.5–3.3 AU [10]) and to various heliographic latitudes (from 23° S to 16° N [8]). Therefore, the integral values of the gradients can, to a great extent, depend on the values of their latitudinal components. The latiudinal gradients of GCRs in the heliosphere were found from meteorite data for the minimum of the 20th solar cycle [8, 11]. This period is of special interest because it differs from the time of the *Ulysses* flight at the minimum of the 22nd solar cycle by exactly one complete 22-year magnetic cycle. Within this cycle, as a result of two magnetic reversals of the general solar magnetic field, the heliosphere magnetic structure was expected to return to the initial state and to be similar in both minima. The values of the latitudinal gradients of GCRs with an energy $E >$ 100 MeV obtained in 1973–1976 according to the data of the Dhajala chondrite attained $G_\theta \sim 3–5\%$ deg^{-1} for the southern latitudes. With allowance for a noticeable difference in the threshold rigidity of particles, this result correlates with the value $G_\theta \sim 0.19 \pm 0.025\%$ deg^{-1} determined in 1994–1996 for GCRs with $E > 2$ GeV [6]. The different orbit inclinations of the Dhajala and Innisfree chondrites to the ecliptic plane (the Dhajala orbit, basically, lies in southern latitudes, while the Innisfree orbit is located in northern ones; Fig. 2) made it possible to estimate the N–S asymmetry of the GCR distribution at the minimum of the 20th solar cycle. The values of G_θ in 1973–1976 for northern latitudes turned out to be small and even negative, changing from ~0.8 to −1.5% deg^{-1}. This effect of the northern–southern asymmetry at the minimum of the 20th solar cycle is explained by the more rapid penetration of GCRs into the southern heliosphere. In this part of the heliosphere, the reconstruction of solar magnetic fields as a result of the inversion of polarity of the general magnetic field of the Sun began earlier than in the northern part. GCR particles could enter into it earlier not only from the poles but also from the near-equatorial zone at latitudes ≤40° S [11]. Still, apparently, this effect is not of general character, since, at the minimum of the 22nd solar cycle, it was not manifested either according to meteorite data (Fig. 1) or in the Ulysses measurements.

Along with the well-known regularity that the even cycles are not as high as the odd ones, the meteorite data in Fig. 1 testify to the fact that the radial gradients of GCRs increase especially strongly immediately prior to the change of the complete magnetic cycle near the maxima of even solar cycles. The lateral inclination to the ecliptic plane of the orbit of the Peekskill chondrite, which fell on October 9, 1992 (Fig. 2), allows us to consider the distribution of high radial gradients of GCRs in this period to be symmetric with respect to southern and northern latitudes. Indeed, the aphelion and perihelion of the Peekskill orbit lie near the line of solar nodes. Therefore, the average heliocentric distances of this chondrite in northern and southern latitudes are practically symmetric. Correspondingly, the high values of GCR radial gradients, which follow from the content of cosmogenic ^{22}Na in this chondrite, are average ones for northern and southern latitudes.

ACKNOWLEDGMENTS

REFERENCES

1. G. A. Bazilevskaya, M. B. Krainev, Yu. I. Stozhkov, *et al.*, J. Geomagn. Geoelectr., Suppl. **43**, 893 (1991).
2. E. N. Parker, *Interplanetary Dynamic Processes* (Interscience, New York, 1963; Mir, Moscow, 1965).
3. L. I. Dorman, *Variations of Galactic Cosmic Rays* (Mosk. Gos. Univ., Moscow, 1975).
4. F. McDonald, H. Moraal, J. P. L. Reinecke, *et al.*, J. Geophys. Res. **97**, 1557 (1992).
5. D. Venkatesan, R. B. Decker, and S. M. Krimigis, in *Proceedings of the 18th International Conference on Cosmic Rays, Bangalore, 1983*, Vol. 10, pp. 156–159.
6. B. Heber, A. V. Belov, A. Raviart, *et al.*, in *Proceedings of the 25th International Conference on Cosmic Rays, Durban, 1997,* Vol. 2, pp. 85–88.
7. A. V. Belov, E. A. Eroshenko, B. Heber, *et al., in Proceedings of the 27th International Conference on Cosmic Rays, Hamburg, 2001*, pp. 3996–3999.
8. A. K. Lavrukhina and G. K. Ustinova, *Meteorites as Probes of the Cosmic-Ray Variations* (Nauka, Moscow, 1990).
9. L. Z. Rumshinskiĭ, *Mathematical Processing of Experimental Data* (Nauka, Moscow, 1971).
10. V. A. Alexeev and G. K. Ustinova, Izv. Akad. Nauk, Ser. Fiz. **63**, 1625 (1999).
11. G. K. Ustinova, in *Proceedings of the 18th International Conference on Cosmic Rays, Bangalore, 1983*, Vol. 10, pp. 71–74.
12. http://www.sunspot.net/cat3sun_r.html.

Translated by G. Merzon

===================== **MECHANICS** =====================

On Gas Flows with a "One-Dimensional" Velocity Potential

Academician L. V. Ovsyannikov

We consider isentropic irrotational gas flows with a special "one-dimensional" velocity potential. The condition of possible continuous adjacency to a rest region leads to the uniqueness theorem for such flows.

The problem of continuing the solution to the gas dynamics equations through acoustical characteristics was investigated by a number of authors [1–3]. It is well known that this continuation conserves entropy and vorticity. If the rest region Ω_0, where a velocity $\mathbf{u} = 0$ and speed of sound $c = 1$, exists on one side of the characteristics Γ specified by the equation

$$t = q(\mathbf{x}), \qquad (1)$$

where t is the time and $\mathbf{x} = (x, y, z)$ are the Cartesian coordinates, then the function q has to satisfy the equation

$$|\nabla q| = 1. \qquad (2)$$

On the other side of Γ (in the region Ω_1), the gas dynamics equations

$$D\mathbf{u} + \beta c \nabla c = 0, \quad \beta Dc + c\,\mathrm{div}\,\mathbf{u} = 0; \qquad (3)$$

$$\mathrm{curl}\,\mathbf{u} = 0, \qquad (4)$$

where $D = \partial_t + \mathbf{u} \cdot \nabla$ and $\beta = \dfrac{2}{\gamma - 1}$, must be fulfilled. We consider a polytropic gas with the equation of state $p = S\rho^\gamma$ ($\gamma > 1$) and entropy $S = \mathrm{const}$. However, the final result is valid for any "normal" gas. The necessary and sufficient conditions of the continuity of the combined solution of the set of Eqs. (3) and (4) in the region $\Omega_0 \cup \Gamma \cup \Omega_1$ on Γ have the form

$$\mathbf{u}|_\Gamma = 0, \quad c|_\Gamma = 1. \qquad (5)$$

There is also the local theorem of existence of an analytic solution to the system of Eqs. (3)–(5) in a (small) neighborhood of the surface Γ with the initial conditions

$$\mathbf{u}(t_0, \mathbf{x}) = \mathbf{u}_0(\mathbf{x}_0), \quad c(t_0, \mathbf{x}) = c_0(\mathbf{x}) \qquad (6)$$

Lavrent'ev Institute of Hydrodynamics, Siberian Division,
Russian Academy of Sciences,
pr. Akademika Lavrent'eva 15, Novosibirsk, 630090 Russia
e-mail: ovs@hydro.nsc.ru

(see, e.g., [4]), which are fitted with the values of unknown quantities ($\mathbf{u}$, c) and their first derivatives on Γ. However, this theorem is insufficient to investigate the solution in the region Ω_1 "as a whole," in particular, to satisfy some additional boundary conditions on a surface far from Γ. Therefore, the problem of constructing proper partial, but analytically simpler, solutions to the system of Eqs. (3) and (4) (e.g., by using its group property) still remains topical. This report is devoted to describing one class of such solutions leading to a peculiar uniqueness theorem.

1. CLASS OF SOLUTIONS

The idea is to find a one-dimensional velocity potential Φ depending only on time t and a certain function $\alpha = \alpha(\mathbf{x})$ i.e., $\Phi = \Phi(t, \alpha)$, where $\Phi_\alpha \neq 0$ and $\nabla\alpha \neq 0$. However, from the condition of continuous adjacency to the rest region through the characteristics Γ (1), it follows that $\Phi_\alpha(q, \alpha) = 0$. Hence, it is necessary that $\alpha = \alpha(q)$ and the one-dimensional potential must have the form $\Phi = \Phi(t, q)$. Then, $\mathbf{u} = \nabla\Phi = \Phi_q \nabla q$ and it follows from the first of Eqs. (3) that, in view of Eq. (2), the speed of sound $c = C(t, q)$. Therefore, the solution of this class can be represented in the form

$$\mathbf{u} = U(t, q)\nabla q, \quad c = C(t, q). \qquad (7)$$

Since $\mathrm{div}\,\mathbf{u} = U_q + U\Delta q$ (where Δq is the Laplacian), substitution into the second of Eqs. (3) shows that there is a certain function f such that $\Delta q = f(q)$.

Consequently, the class of solutions in the form under consideration is described by the system of equations for the function $q(\mathbf{x})$

$$|\nabla q| = 1, \quad \Delta q = f(q) \qquad (8)$$

and the system of gas dynamics equations

$$U_t + UU_q + \beta CC_q = 0,$$
$$\beta(C_t + UC_q) + CU_q + CUf(q) = 0. \qquad (9)$$

2. POSSIBLE FORMS OF $f(q)$

A solution of overdetermined system (8) exists only for certain functions $f(q)$. It is evident that system (8) admits an eight-dimensional group of transformations

G_8 of the $\mathbb{R}^5(\boldsymbol{\omega})$ space, where $\boldsymbol{\omega} = (x, y, z, q, f)$. The transformations act according to the formula

$$\boldsymbol{\omega}' = g(\boldsymbol{\omega}), \quad g \in G_8. \tag{10}$$

The G_8 group is generated by translations along the coordinates $\mathbf{x}$, rotations in $\mathbb{R}^3(\mathbf{x})$, extension with the parameter σ ($\mathbf{x}' = \sigma\mathbf{x}$, $q' = \sigma q$, $f' = \sigma^{-1}f$), and translation along the coordinate q with the parameter τ [$q' = q + \tau$, $f'(q') = f(q + \tau)$]. Such transformations will be called equivalence transformations of the solutions to system (8). The problem of seeking possible solutions to system (8) can be considered including equivalence transformations.

In what follows, we briefly outline one of the possible methods of solving system (8). To construct the general solution to the first of Eqs. (8) rewritten in the form

$$q_x^2 + q_y^2 + q_z^2 = 1, \tag{11}$$

we use the method of the "complete integral" in the form

$$q^2 = (x + a)^2 + (y + b)^2 + (z + \varphi)^2. \tag{12}$$

When a, b and φ are constant, formula (12) gives a three-parametric solution to Eq. (11). The position $\varphi = \varphi(a, b)$ with any smooth function φ defines a two-parametric family, and the general solution is constructed as its envelope. The envelope is found by equating the derivatives with respect to the parameters a and b in equality (12) to zero:

$$\begin{aligned} qq_a &\equiv x + a + (z + \varphi)\varphi_a = 0, \\ qq_b &\equiv y + b + (z + \varphi)\varphi_b = 0. \end{aligned} \tag{13}$$

The substitution of functions $a = a(x, y, z)$ and $b = b(x, y, z)$, which are obtained from system (13), into formula (12) gives the desired general solution. Indeed, in view of Eqs. (13), the relations

$$qq_x = x + a, \quad qq_y = y + b, \quad qq_z = z + \varphi \tag{14}$$

are valid. With allowance for (11), differentiating Eqs. (14), we arrive at the equation

$$q\Delta q = 2 + a_x + b_y + \varphi_a a_z + \varphi_b b_z. \tag{15}$$

Here, the derivatives of the functions a and b are calculated from system (13) if the Jacobian δ of the left-hand sides of Eqs. (13) with respect to the variables (a, b) is not equal to zero. Calculating δ with allowance for (12), we obtain

$$\delta = m^2(1 + 2qH + q^2K), \quad m = \sqrt{1 + \varphi_a^2 + \varphi_b^2},$$

where H is the mean curvature of the surface $\varphi = \varphi(a, b)$,

$$2H = m^{-3}[(1 + \varphi_a^2)\varphi_{bb} - 2\varphi_a\varphi_b\varphi_{ab} + (1 + \varphi_b^2)\varphi_{aa}],$$

and K is the Gaussian curvature of this surface,

$$K = m^{-4}(\varphi_{aa}\varphi_{bb} - \varphi_{ab}^2).$$

Since the quantities q, a, and b are functionally independent of each other in view of Eqs. (13), and the curvatures H and K depend only on (a, b), then $\delta \neq 0$. Finally, calculating the derivatives entering into Eq. (15), we arrive at the formula

$$\Delta q = \frac{2(H + qK)}{1 + 2qH + q^2K}. \tag{16}$$

The second of Eqs. (13) means that the right-hand side of Eq. (16) must depend only on q. This is possible only when both curvatures H and K of the surface $\varphi = \varphi(a, b)$ are constants. As is known from differential geometry [5], the set of such surfaces consists only of planes ($H = K = 0$), circular cylinders of radius R $\left(H = 1/2R, \ K = 0\right)$, and spheres of radius R $\left(H = \frac{1}{R}, \ K = \frac{1}{R^2}\right)$.

Substitution of the above curvatures shows that, up to equivalence transformations, the function f can take only the form

$$f(q) = \frac{\nu}{q}, \tag{17}$$

where $\nu = 0, 1$, and 2 for a plane, cylinder, and sphere, respectively.

3. RESULTS

It remains to find the function $q(\mathbf{x})$. For this purpose, the functions a and b are calculated from system (13) for each of the above cases. This stage is facilitated, because any equivalence transformation described in Section 2 (G_8 group) is continued to the corresponding transformations of the $\mathbb{R}^3(a, b, \varphi)$ space. This makes it possible to reduce the equation of each surface under consideration to the canonical form. Using relations (13) and (14), it is easy to find that, up to equivalence transformations, $q = r$, where either $r = x$ (plane), or $r =$

$\sqrt{x^2 + y^2}$ (cylinder), or $r = \sqrt{x^2 + y^2 + z^2}$ (sphere). Thus, the following theorem is valid.

Uniqueness theorem. *The class of isentropic irrotational gas flows with a one-dimensional velocity potential, where continuous adjacency to the rest region is possible, consists, up to equivalence transformations, of flows with plane, cylindrical, and spherical waves.*

Nevertheless, the problem of adjacency to the rest region remains nontrivial in the above cases, except for the case $\nu = 0$, where the simple wave is inevitably present in the region Ω_1. Sufficient conditions on initial data (6) that would ensure the existence of a continuous solution as a whole remain unknown. The solutions that are invariant with respect to one-parametric subgroups of the group admitted by system (9) in the cases $\nu = 1$ and 2, where the factor system reduces to a quite transparent system of ordinary differential equations, were described in [6, 7].

REFERENCES

1. A. F. Sidorov, Prikl. Mat. Mekh. **30**, 164 (1966).
2. A. F. Sidorov, Prikl. Mat. Mekh. **32**, 369 (1968).
3. V. M. Teshukov, *Dynamics of Continuous Medium: Collection of Works* (Inst. Gidrodin. Sib. Otd. Akad. Nauk SSSR, Novosibirsk, 1977), Issue 32, pp. 82–94.
4. S. P. Bautin, *Mathematical Theory of Non-Shock Strong Compression of Ideal Gas* (Nauka, Novosibirsk, 1997).
5. T. Levi-Civita, Atti Accad. Naz. Lincei, Cl. Sci. Fis., Mat. Nat., Rend. **26**, 355 (1937).
6. N. N. Kochina, Prikl. Mat. Mekh. **21**, 449 (1957).
7. L. I. Sedov, *Similarity and Dimensional Methods in Mechanics*, 10th ed. (Nauka, Moscow, 1987; Academic, New York, 1959).

Translated by Yu. Vishnyakov

===== **MECHANICS** =====

Averaging Algorithms for Problems of the Theory of Elasticity on Rectangular Grids Nonconforming to the Structure of a Medium

Academician V. P. Myasnikov, M. Yu. Zaslavsky*, and A. Kh. Pergament**

In this work, a method of averaging coefficients was developed for two-dimensional problems of the theory of elasticity. After averaging, an element of an initially isotropic medium that has a complex internal structure can be described by an anisotropic model. This means that the effective elastic modulus tensor is defined for each such element to obtain the exact energy functional for a certain class of functions. The tensor is defined by means of special basis functions presenting the features of the medium. As a result, using rectangular grids, we develop finite difference schemes that are better posed than schemes on grids adapted to the medium structure. Test calculations are presented.

1. The most extensively used method of solving two-dimensional problems of the theory of elasticity for media with piecewise constant coefficients is the finite element method [3, 4]. This method has obvious advantages for static problems. The primary advantage of the algorithm is its generality and convenient implementation. Fedorenko *et al.* [5, 6] proposed the generalization of the algorithm that is called the superelement method and that makes it possible to efficiently solve problems for media including regions that are structurally very different. The feature of projection methods including the superelement method is that they ensure strong convergence.

Attempts to apply the finite element method to problems of the theory of elasticity are also of interest. Algorithms for homogeneous media were constructed in [7]. The features of realization of the support operator method for inhomogeneous media on grids adapted to the medium structure were discussed in [8, 9]. The fundamental feature of these algorithms is the construction of the strain tensor. By analogy with the gradient operator, it is natural to define the distortion tensor.

Keldysh Institute of Applied Mathematics,
Russian Academy of Sciences,
Miusskaya pl. 4, Moscow, 125047 Russia
 * *e-mail: mikezaslavsky@yandex.ru*
** *e-mail: pergam@keldysh.ru*

However, to construct the difference scheme for the equations of the theory of elasticity, it is necessary to construct the strain tensor and use the tensor variant of the divergence theorem. The convergence of the method for the constant coefficients was proved both for the L_2 metric and for the uniform metric. If the coefficients are piecewise continuous functions, convergence in L_p norms can be obtained at least with the same order as convergence in flow norms due to the difference analogues of the embedding theorems. However, the use of this method for applied problems is quite difficult. It is primarily important to have an alternative to approximation methods on curvilinear grids in the presence of narrow zones with contrast parameters.

In this work, we develop an averaging algorithm for problems of the theory of elasticity that is similar to that developed by Moskow, Druskin, *et al.* [1] for a scalar elliptic equation.

2. We consider the following problem of the theory of elasticity:

$$\sigma_{ij,j} + f_i = 0, \tag{1}$$

$$\sigma_{ij} = \Lambda_{ijkl}\epsilon_{kl}, \tag{2}$$

$$\epsilon_{kl} = \frac{1}{2}(u_{k,l} + u_{l,k}) \tag{3}$$

in the two-dimensional domain $\Omega = [0; 1]^2$ with the kinematical boundary conditions $u|_{\partial\Omega} = 0$ in an isotropic inhomogeneous medium

$$\Lambda_{ijkl} = \lambda\delta_{ij}\delta_{kl} + \mu(\delta_{ik}\delta_{jl} + \delta_{il}\delta_{jk}).$$

We assume that $\mu > 0$ and $\lambda > 0$.

In this case, the fundamental feature of the averaging method is a change in the character of the medium. Indeed, the medium in each cell is isotropic, whereas a small finite element of the medium contains structural singularities and is not isotropic. In application to scalar problems, King *et al.* [2] proposed a method of calculating the effective conductivity tensor for each cell (upscaling). They applied this algorithm for the case where the two-dimensional domain consists of structur-

ally different rectangles. The algorithm developed by Moskow, Druskin, *et al.* seems to be more efficient for problems where lines separating domains with contrast coefficients are arbitrarily oriented with respect to the interfaces.

3. An algorithm for solving this problem is realized on a Lebedev grid. We consider the Cartesian uniform grid $S = \{(ih_1; jh_2)\}_{i,j=1}^N$. A subset of S with an even sum $i + j$ is called the Lebedev P grid. In what follows, we will also consider the R grid consisting of nodes of S that are not included in the P grid. We aim to generalize the approach proposed in [1] for averaging the Lamé coefficients λ and μ. We note that the cells of the P and R grids have the same structure for averaging on rectangles and are shown in Fig. 1.

We consider that lines of coefficient discontinuities are so smooth that they can be approximated by a straight line in each R cell and that the Lamé coefficients change only along one direction $\lambda = \lambda(\mathbf{nr})$, $\mu = \mu(\mathbf{nr})$. If the opening of cracks is absent in problems of the theory of elasticity, $\sigma_{ij}n_j$ and $u_{i,j}m_j$, where $\mathbf{n}$ and $\mathbf{m}$ are the normal and tangent to the interface, are continuous functions. Thus, forces applied to an area tangent to the interface, as well as displacements, are continuous. Therefore, the corresponding distortion tensor components are continuous. In what follows, we consider that these quantities are smooth enough to be approximated by constants.

Numerous investigations show that the order of convergence of the method is determined by the order of approximating flows in a problem due to the embedding theorems. Derivatives and flows can be approximated by linear functions. However, linear functions do not have the necessary properties near interfaces. For this reason, the representation of a solution of a boundary value problem for the simplest elliptic equation in the form of the linear shell of vectors 1, $\mathbf{mr}$, $\int_0^{nr} \dfrac{ds}{k}$ was proposed in [1]. Consequently, we consider functions belonging to the linear shell of vectors

$$U^1 = \mathbf{m}\int_0^{nr}\frac{ds}{\mu}, \quad U^2 = \mathbf{n}\int_0^{nr}\frac{ds}{\lambda+2\mu},$$

$$U^3 = \mathbf{m}(\mathbf{mr}) - \mathbf{n}\int_0^{nr}\frac{\lambda ds}{\lambda+2\mu}, \quad U^4 = -\mathbf{m}(\mathbf{nr})+\mathbf{n}(\mathbf{mr}),$$

$$U^5 = \mathbf{m}, \quad U^6 = \mathbf{n},$$

$$u \in L(H) = \mathrm{span}\left\{U^1 = \mathbf{m}\int_0^{nr}\frac{ds}{\mu}, \quad U^2 = \mathbf{n}\int_0^{nr}\frac{ds}{\lambda+2\mu},\right.$$

$$U^3 = \mathbf{m}(\mathbf{mr}) - \mathbf{n}\int_0^{nr}\frac{\lambda ds}{\lambda+2\mu},$$

$$\left. U^4 = -\mathbf{m}(\mathbf{nr})+\mathbf{n}(\mathbf{mr}), \quad U^5 = \mathbf{m}, \quad U^6 = \mathbf{n}\right\}.$$

We determine six components of the effective elastic modulus tensor Σ_{ijkl}^H by equating the continuous and discrete energies in each cell for vectors from $L(H)$. Since U^5 and U^6 represent motion of a body as a whole and U^4 represents its rotation about the z axis, they correspond to zero strain. Thus, we obtain six equations for six components Σ_{ijkl}^H:

$$\int_H \Lambda_{ijkl}\epsilon_{ij}^\alpha\epsilon_{kl}^\beta dV = |H|\Sigma_{ijkl}^H\epsilon_{h,ij}^\alpha\epsilon_{h,kl}^\beta, \qquad (4)$$

$$\alpha, \beta = 1, 2, 3.$$

The left-hand side of Eq. (4) for different α and β has the form of the symmetric 3×3 matrix

$$\begin{pmatrix} \displaystyle\int_H\frac{dV}{\mu} & 0 & 0 \\[2ex] 0 & \displaystyle\int_H\frac{dV}{\lambda+2\mu} & 0 \\[2ex] 0 & 0 & \displaystyle\int_H\frac{4\mu(\lambda+\mu)dV}{\lambda+2\mu} \end{pmatrix},$$

and $\epsilon_{h,ij}^\alpha$ in Eq. (4) are the simplest approximations of expressions (3) by the central differences for the vec-
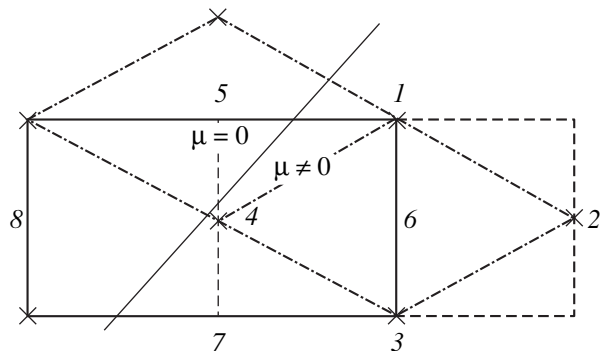

Fig. 1. Solid lines are the interface and P cell; dashed and dash–dotted lines are rectangular and rhombic R cells, respectively.

tor U^α in the cell H. For example,

$$\epsilon_{h,\,12}^{\alpha} = 0.5\left(\frac{U^\alpha(2) - U^\alpha(4)}{h_1} + \frac{U^\alpha(1) - U^\alpha(3)}{h_2}\right).$$

Thus, the stress tensor is approximated as

$$\sigma_{h,\,ij}^{H} = \Sigma_{ijkl}^{H}\epsilon_{h,\,kl}^{H}. \tag{5}$$

The stress-tensor divergence in a cell of the P grid is also approximated by the central differences:

$$\mathrm{div}_h\sigma_{h,\,ij} = \frac{\sigma_{h,\,i1}(6) - \sigma_{h,\,i1}(8)}{h_1} + \frac{\sigma_{h,\,i2}(5) - \sigma_{h,\,i2}(7)}{h_2}. \tag{6}$$

Thus, the finite-difference problem has the form

$$\mathrm{div}_h\sigma_{h,\,ij} + f_i^{P} = 0, \tag{7}$$

where $f_i^{P} = \dfrac{1}{|H|}\displaystyle\int_H f_i$.

A difference analogue of the energy norm for tensor quantities can be defined on the basis of relation (4). Then, divergence in relation (7) can be constructed by a method similar to the support operator method, i.e., on the basis of the difference analogue of the divergence theorem, in vector form:

$$(U, V)_\Lambda + (\mathrm{div}\sigma(U), V)_0 = 0, \tag{8}$$

where

$$(U, V)_\Lambda = \int_\Omega \sigma_{ij}(U)\epsilon_{ij}(V),$$

$$(\mathrm{div}\sigma(U), V)_0 = \int_\Omega \sigma_{ij,\,j}(U)v_i.$$

In this case, the strain tensor serves as a gradient.

Let the difference approximation of the first and second terms of Eq. (8) have the form

$$(U, V)_\Sigma = \frac{1}{2}\sum_{H \in R} |H|\sigma_{h,\,ij}^{H}(U)\epsilon_{h,\,ij}^{H}(V),$$

$$(\mathrm{div}\sigma(U), V)_P = \frac{1}{2}\sum_{H \in P} |H|\mathrm{div}_h\sigma_{h,\,ij}^{H}(U)v_i,$$

respectively. Then, divergence (6) satisfies the identity

$$(U, V)_\Sigma + (\mathrm{div}\sigma(U), V)_P = 0. \tag{9}$$

The resulting expression for the flow has the approximation order $O(1)$ near a discontinuity and $O(h)$ in all other cells; i.e., it has the standard properties of such schemes. However, the advantage of this scheme is that it exactly approximates the energy integral for functions from $L(H)$, which can be substantial for estimation of the accuracy and convergence rate in the energy norm.

4. The method of coefficient averaging over rectangles discussed above has one substantial demerit. The elements of the resulting tensor Σ_{ijkl}^{H} can tend to infinity if μ tends to zero in a certain corner cell of the R grid such that each of the central differences "does not include" the small μ value (Fig. 1). Thus, when μ tends to zero, the condition number of the resulting matrix of the system increases. Therefore, its inversion requires large CPU time.

If $\mu = 0$ in a certain subdomain of Ω, i.e., the domain is partially filled with water, the general problem loses uniqueness and can be solved under additional assumptions. In this case, the above algorithm has a number of difficulties for μ tending to zero.

One of the possible methods of solving this problem is to add a rectangular domain to each node of the P grid and a rhombus to each R node (Fig. 1). In this case, intersection of the interface with a cell affects at least one central difference in the R cell.

Let the interface intersect the line *2–4*. If μ tends to zero, expressions on the left-hand side of Eqs. (4) tend to infinity. We note that a solution of problem (1)–(3) remains limited when μ tends to zero; i.e., this is only a feature of the behavior of the basis functions. Displacements in the problem remain finite. The system must be normalized to obtain the tensor Σ_{ijkl}^{H}. It is appropriate first to divide both sides of Eq. (4) for $\alpha = \beta = 1$ by

$\left(\displaystyle\int_2^4 \frac{dV}{\mu}\right)^2$ and then to divide both sides of Eq. (4) for

$\alpha = 1$, $\beta = 2$ and $\alpha = 1$, $\beta = 3$ by $\displaystyle\int_2^4 \frac{dV}{\mu}$.

We note that this normalization in the method under consideration allows averaging of coefficients in a cell partially filled with water ($\mu = 0$). Any similar normalization is absent for the method of coefficient averaging on rectangles.

Similarly to the method of coefficient averaging on rectangles, the stress tensor divergence is approximated according to the difference analogue of the integral
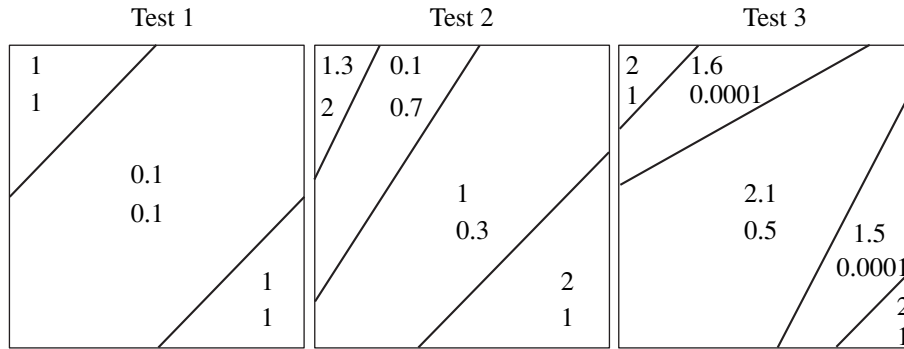
Test 1   Test 2   Test 3

Fig. 2. Parameters (upper numbers) λ and (lower numbers) μ in the (from left to right) first, second, and third tests.

identity, where its two terms are approximated as

$$(U, V)_\Sigma = \sum_{H \in R} |H| \sigma^H_{h, ij} \epsilon^H_{h, ij},$$

$$(\mathrm{div}\sigma(U), V)_P = \frac{1}{2} \sum_{H \in P} |H| \mathrm{div}_h \sigma^H_{h, ij} u_i.$$

5. We consider the convergence of the resulting algorithm. Let

$$U = (u_1, u_2) \in H^L,$$

where

$$H^L = \{U : u_i \in H^1(\Omega), \ \sigma_{ij} n_j \in H^1(\Omega), \ u_{i, j} m_j \in H^1(\Omega)\}$$

with the norm

$$\|U\|^2_{H^L} = \|U\|^2_{H^L} + |U|^2_{H^L}.$$

The space $H^1(\Omega)$ is a vector space, and the norm in this space is the sum of the norms of all components:

$$\|U\|^2_{H^L} = \int_\Omega u_1^2 + u_2^2 + \left(\frac{\partial u_1}{\partial x}\right)^2 + \left(\frac{\partial u_1}{\partial y}\right)^2$$
$$+ \left(\frac{\partial u_2}{\partial x}\right)^2 + \left(\frac{\partial u_2}{\partial y}\right)^2.$$

The seminorm in the space H^L is defined as

$$|U|^2_{H^L} = \int_\Omega \sum_i (\sigma_{ij} n_j)^2 + (u_{i, j} m_j)^2$$
$$+ \sum_{i, k} (\sigma_{ij} n_j)^2_{,k} + (u_{i, j} m_j)^2_{,k},$$

where **m** and **n** are tangents to the coordinate lines of the vector (vector **n** is perpendicular to discontinuities). Interfaces are implied to coincide with coordinate lines in the common curvilinear coordinates for the entire domain.

The following lemma will be necessary.

Lemma 1. *For* $w \in H^1(H)$, *where H is a cell of the R grid, there is a constant* C_1 *such that*

$$\|w - C_1\|_{L^2(H)} \le Ch\|w\|_{H^1(H)}.$$

This lemma follows from the standard properties of approximation of functions from H^1.

Using this lemma, one can easily prove the approximation theorem. We recall that interfaces are approximated by straight lines in each R cell.

Theorem 1. *For each cell of the R grid H and vector* $U \in H^L(H)$, *there is a vector* $d_H U \in L(H)$ *such that*

$$\|U - d_H U\|_{H^1(H)} \le Ch\|U\|_{H^L(H)}, \tag{10}$$

$$\|U - d_H U\|_{L^2(H)} \le Ch^2\|U\|_{H^L(H)}. \tag{11}$$

Then, similarly to [1], one can prove first-order weak convergence of the constructed algorithm.

Theorem 2. *For solution* $U \in H^L(\Omega)$ *of the problem specified by Eqs. (1)–(3) and solution* U_h *of the difference problem specified by Eqs. (5)–(7), there is a constant C such that*

$$|(U - U_h, V)_\Sigma| \le Ch(\|U\|_{H^L(\Omega)} + \|F\|_{L^2(\Omega)})\|V\|_{H^L(\Omega)}$$

for all $V \in H^L(\Omega)$.

6. The constructed algorithm was tested on several problems. The distribution of the Lamé coefficients for them is shown in Fig. 2. The distribution of mass forces for all tests was symmetric with respect to the $y = x$ straight line. Tables 1–3 show errors in various norms for both components of displacement in three tests. Fig-
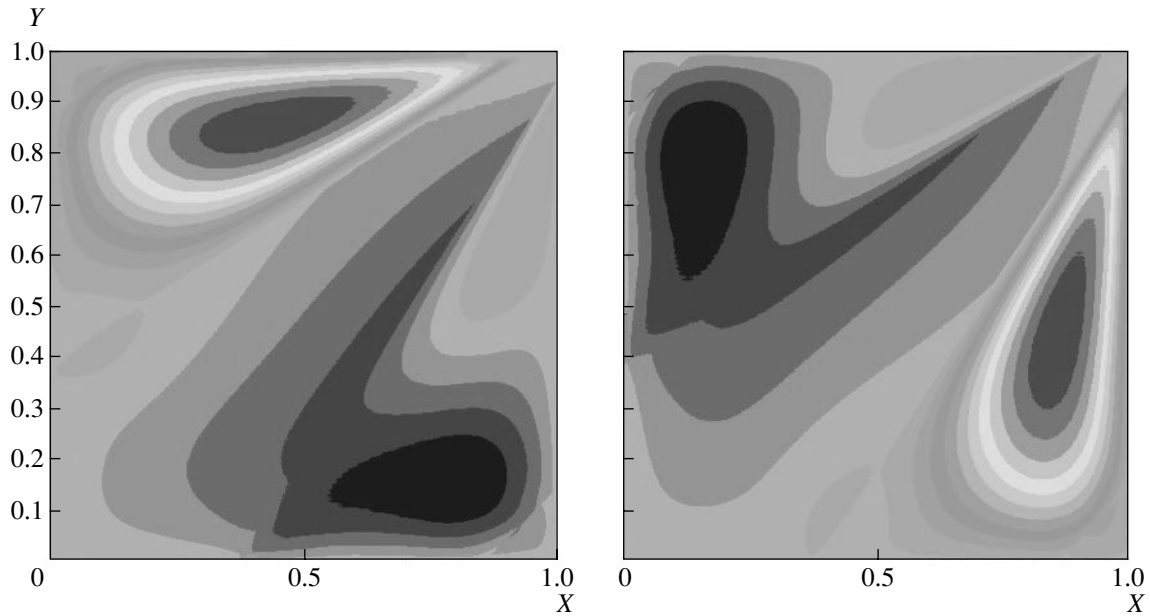
Fig. 3. Distribution of u_x and u_y in the third test.

ure 3 shows the distribution of the displacement components u_x and u_y for the third test.

According to theoretical notions, the averaging algorithm is expected to have accuracies $O(h)$ and $O(h^2)$ in the energy norm and L_2 norm, respectively. Calculations show that moderately fine grids provide convergence of the order higher than the first order both in the C norm and in L_2 norm. Second-order convergence is obtained in the second test.

Table 1. Errors for the method of coefficient averaging on rectangles in the first test

N	10	20	40	80
$\|u_1 - u_{h,1}\|_C$	0.00617955	0.00097876	0.000389107	0.000145658
$\|u_2 - u_{h,2}\|_C$	0.00617955	0.00097876	0.000389107	0.000145658
$\|u_1 - u_{h,1}\|_{L_2}$	0.00185951	0.000326695	0.000105144	3.3037×10^{-5}
$\|u_2 - u_{h,2}\|_{L_2}$	0.00185951	0.000326695	0.000105144	3.3037×10^{-5}

Table 2. The same as in Table 1 but for the second test

N	10	20	40	80
$\|u_1 - u_{h,1}\|_C$	0.00492401	0.000404645	0.000162193	6.76203×10^{-5}
$\|u_2 - u_{h,2}\|_C$	0.00194423	0.000404349	0.000245959	6.80619×10^{-5}
$\|u_1 - u_{h,1}\|_{L_2}$	0.000942086	0.000115963	3.34685×10^{-5}	8.17713×10^{-6}
$\|u_2 - u_{h,2}\|_{L_2}$	0.000532591	0.000110067	3.3949×10^{-5}	7.85302×10^{-6}

Table 3. Errors for the method of coefficient averaging on rhombuses in the third test

N	20	40	80	160	320
$\|u_1 - u_{h,1}\|_C$	0.0345951	0.00417366	0.00224269	0.00125584	0.00078656
$\|u_2 - u_{h,2}\|_C$	0.0345951	0.00417366	0.00224269	0.00125584	0.00078656
$\|u_1 - u_{h,1}\|_{L_2}$	0.0061631	0.00090232	0.000437141	0.000206399	9.50053×10^{-5}
$\|u_2 - u_{h,2}\|_{L_2}$	0.0061631	0.00090232	0.000437141	0.000206399	9.50053×10^{-5}

The support operator method on adapted grids theoretically has the same accuracy. However, when the grid is considerably deformed, the maximum principle for a difference problem can be violated for the support operator method, and, therefore, the scheme is not monotonic. This difficulty can be overcome by using rectangular grids in the averaging method. The averaging method is primarily preferable over both the support operator method and finite element method for problems where the Lamé coefficients considerably differ from each other in a narrow domain (crack).

ACKNOWLEDGMENTS

REFERENCES

1. S. Moskow, V. Druskin, T. Habashy, *et al.*, SIAM (Soc. Ind. Appl. Math.) J. Numer. Anal. **36**, 442 (1999).

2. P. R. King, A. H. Muggeridge, and W. G. Price, Transp. Porous Media **12**, 237 (1993).

3. Ph. Ciarlet, *The Finite Element Method for Elliptic Problems* (North-Holland, Amsterdam, 1977; Mir, Moscow, 1980).

4. I. Babuska, G. Caloz, and J. E. Osborn, SIAM (Soc. Ind. Appl. Math.) J. Numer. Anal. **31**, 945 (1994).

5. R. P. Fedorenko, *Introduction to Computational Physics* (Mosk. Fiz.-Tekh. Inst., Moscow, 1994).

6. V. T. Zhukov, N. D. Novikova, L. G. Strakhovskaya, *et al.*, Preprint No. 8, IPM (Russia Keldysh Institute of Applied Mathematics, Russian Academy of Sciences, Moscow, 2001).

7. A. A. Samarskiĭ, A. V. Koldoba, Yu. A. Poveshchenko, V. V. Tishkin, and A. P. Favorskiĭ, *Difference Schemes on Irregular Meshes* (Minsk, 1996).

8. A. V. Koldoba, A. Kh. Pergament, Yu. A. Poveshchenko, and N. A. Simus, Mat. Model. **11** (10), 3 (1999).

9. O. A. Dremov, A. V. Koldoba, A. Kh. Pergament, *et al.*, Preprint No. 131, IPM RAN (Keldysh Inst. of Applied Mathematics, Russian Academy of Sciences, Moscow, 1995).

Translated by R. Tyapaev

====== **MECHANICS** ======

Swing Problem

A. P. Seyranian

Presented by Academician V.F. Zhuravlev September 3, 2003

Received September 5, 2003

The swing problem is undoubtedly among the classical problems of mechanics. Practice has shown that, to set a swing into motion, one should squat when the swing is in the limit positions and stand erect in the middle vertical position, i.e., execute oscillations with double the natural frequency of the swing. To sustain the oscillations of the swing, the frequency of squatting can be halved. Nevertheless, a clear and complete, qualitative and quantitative, analysis of setting the swing into motion is absent in papers on oscillations and stability.

The simplest model of the swing [1–4] is described by oscillations of a massless rod with a concentrated mass periodically sliding without friction along the rod axis. This model also describes oscillations of a pendulum whose length varies periodically with time (Fig. 1). The mass displacement amplitude or variation in pendulum length is assumed to be small. Moreover, small viscous friction due to air resistance is taken into account in this study. The periodic excitation function may be arbitrary. Asymptotic formulas for domains of instability (parametric resonance) in the three-dimensional parameter space that correspond to setting the swing into motion are derived and analyzed. The method of solving the problem is rigorous, because it is directly based on an analysis of the behavior of Floquet multiplicators. Some examples are presented.

1. The equation of motion of a swing (variable-length pendulum) [1, 2] with allowance for viscous friction has the form

$$(ml^2\dot{\theta})^{\cdot} + \gamma l^2\dot{\theta} + mgl\sin\theta = 0, \tag{1}$$

where m is the mass, l is the length, θ is the angle of the pendulum deflection from the vertical, γ is the coefficient of viscous friction due to air resistance, and g is the gravitational acceleration. The dot refers to the derivative with respect to time t. It is assumed that the

pendulum length varies as

$$l = l_0 + a\varphi(\Omega t), \tag{2}$$

where l_0 is the mean length of the pendulum; a and Ω are the excitation amplitude and frequency, respectively; and $\varphi(\tau)$ is an arbitrary smooth periodic function with a period of 2π and zero mean value, i.e., $\int_0^{2\pi} \varphi(\tau)d\tau = 0$. The amplitude a and the friction coefficient γ are assumed to be small. It is necessary to determine the parameters at which the trivial equilibrium position $\theta = 0$ of the system becomes unstable, which leads to setting the swing into motion.

We introduce the dimensionless variables and parameters

$$\tau = \Omega t, \quad \varepsilon = \frac{a}{l_0}, \quad \beta = \frac{\gamma}{m}\sqrt{\frac{l_0}{g}}, \quad \omega = \frac{1}{\Omega}\sqrt{\frac{g}{l_0}},$$

$$x_1 = \theta, \quad x_2 = \frac{l^2\dot{\theta}}{l_0^2\Omega}. \tag{3}$$

Then, Eq. (1) can be written in the form of the system

Fig. 1. Swing.
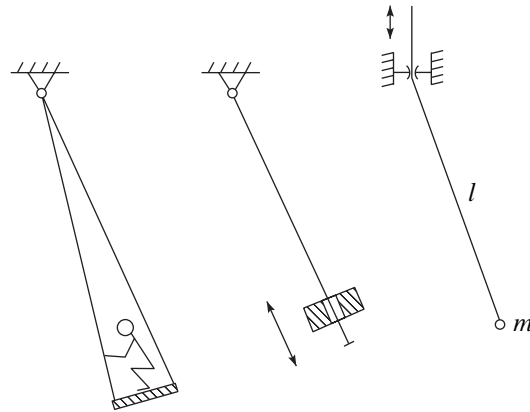
Institute of Mechanics, Moscow State University,
Michurinskiĭ pr. 1, Moscow, 117192 Russia
e-mail: seyran@imec.msu.ru

of first-order equations

$$\frac{dx_1}{d\tau} = \left(\frac{l_0}{l}\right)^2 x_2,$$

$$\frac{dx_2}{d\tau} = -\omega^2\left(\frac{l}{l_0}\right)\sin x_1 - \beta\omega x_2,$$

(4)

$$\frac{l}{l_0} = 1 + \varepsilon\varphi(\tau).$$

(5)

In these variables, the requirement of smoothness of the periodic function $\varphi(\tau)$ can be weakened and the function can be piecewise continuous.

The right-hand sides of Eqs. (4) are nonlinear functions of the vector $\mathbf{x} = (x_1, x_2)$ and periodic functions of τ with a period of 2π. Equations (4) and (5) depend explicitly on three independent parameters ω, ε, and β. The last two parameters are assumed to be small:

$$\varepsilon = \frac{a}{l_0} \ll 1, \quad \beta = \frac{\gamma}{m}\sqrt{\frac{l_0}{g}} \ll 1.$$

(6)

We will determine the domains of instability of the trivial solution $\mathbf{x} = 0$ (parametric resonance domains) in the three-dimensional space of the parameters $\mathbf{p} = (\varepsilon, \beta, \omega)$.

2. In accordance with the Lyapunov theorem, the stability and instability of the nonlinear system of Eqs. (4) and (5) can be determined from the linear approximation [5]. Linearization of system (4) results in the equations

$$\dot{\mathbf{x}} = \mathbf{G}\mathbf{x},$$

(7)

$$\mathbf{G} = \begin{bmatrix} 0 & [1 + \varepsilon\varphi(\tau)]^{-2} \\ -\omega^2[1 + \varepsilon\varphi(\tau)] & -\beta\omega \end{bmatrix}.$$

(8)

The fundamental, or evolution, matrix $\mathbf{X}(t)$ of system (7) is determined from the differential matrix equation with the initial condition

$$\dot{\mathbf{X}} = \mathbf{G}\mathbf{X}, \quad \mathbf{X}(0) = \mathbf{I},$$

(9)

where $\mathbf{I}$ is the identity matrix. The monodromy (Floquet) matrix is defined by the equality $\mathbf{F} = \mathbf{X}(T)$ [5, 6]. To study the stability of the linear system of Eqs. (7) and (8), we will use the Floquet theorem, which states that a linear system with periodic coefficients is stable if the absolute values of all eigenvalues ρ (multiplicators) of the monodromy matrix $\mathbf{F}$ are less than unity, and it is unstable if at least one multiplicator is greater than unity in absolute value.

Let the monodromy matrix $\mathbf{F}_0 = \mathbf{F}(\mathbf{p}_0)$ be known for a certain n-dimensional parameter vector $\mathbf{p}_0$. If the

parameter vector changes as $\mathbf{p} = \mathbf{p}_0 + \Delta\mathbf{p}$, the matrix $\mathbf{G}$ and, therefore, $\mathbf{X}(t)$ gain increments. Correspondingly, the monodromy matrix $\mathbf{F}$ changes. In [7, 8], the first and second derivatives of the monodromy matrix with respect to the parameters were represented in terms of integrals over the period:

$$\frac{\partial\mathbf{F}}{\partial p_k} = \mathbf{F}_0\int_0^T \mathbf{X}_0^{-1}\frac{\partial\mathbf{G}}{\partial p_k}\mathbf{X}_0 d\tau, \quad k = 1, 2, \ldots, n; \quad (10)$$

$$\frac{\partial^2\mathbf{F}}{\partial p_i\partial p_j} = \mathbf{F}_0\Bigg[\int_0^T \mathbf{X}_0^{-1}\frac{\partial^2\mathbf{G}}{\partial p_i\partial p_j}\mathbf{X}_0 d\tau$$

$$+ \int_0^T \mathbf{X}_0^{-1}\frac{\partial\mathbf{G}}{\partial p_i}\mathbf{X}_0\left(\int_0^T \mathbf{X}_0^{-1}\frac{\partial\mathbf{G}}{\partial p_j}\mathbf{X}_0 d\zeta\right)d\tau \quad (11)$$

$$+ \int_0^T \mathbf{X}_0^{-1}\frac{\partial\mathbf{G}}{\partial p_j}\mathbf{X}_0\left(\int_0^T \mathbf{X}_0^{-1}\frac{\partial\mathbf{G}}{\partial p_i}\mathbf{X}_0 d\zeta\right)d\tau\Bigg], \quad i, j = 1, 2, \ldots, n,$$

here the subscript 0 implies that the corresponding quantity is taken as $\mathbf{p} = \mathbf{p}_0$. We note that, for calculating derivatives (10) and (11), only the evolution matrix $\mathbf{X}_0(t)$ and the derivatives of the matrix $\mathbf{G}$ with respect to the parameters calculated at $\mathbf{p} = \mathbf{p}_0$ must be known. The monodromy matrix increment can be written in terms of derivatives (10) and (11):

$$\mathbf{F}(\mathbf{p}_0 + \Delta\mathbf{p}) = \mathbf{F}_0 + \sum_{k=1}^n \frac{\partial\mathbf{F}}{\partial p_k}\Delta p_k$$

$$+ \frac{1}{2}\sum_{i,j=1}^n \frac{\partial^2\mathbf{F}}{\partial p_i\partial p_j}\Delta p_i\Delta p_j + \ldots. \quad (12)$$

Knowing the derivatives of the monodromy matrix, one can calculate this matrix in the vicinity of the point $\mathbf{p}_0$ and, hence, estimate the behavior of the multiplicators (eigenvalues of the monodromy matrix $\mathbf{F}$) responsible for the stability of system (7) when the parameters are varied.

Setting $\varepsilon = 0$ and $\beta = 0$ in Eqs. (7) and (8), we can easily obtain the evolution matrix and its inverse matrix from Eqs. (9):

$$\mathbf{X}_0(t) = \begin{bmatrix} \cos\omega t & \omega^{-1}\sin\omega t \\ -\omega\sin\omega t & \cos\omega t \end{bmatrix},$$

$$\mathbf{X}_0^{-1}(t) = \begin{bmatrix} \cos\omega t & -\omega^{-1}\sin\omega t \\ \omega\sin\omega t & \cos\omega t \end{bmatrix}.$$

(13)

Thus, at $\varepsilon = 0$ and $\beta = 0$, the monodromy matrix

takes the form

$$\mathbf{F}_0 = \mathbf{X}_0(2\pi) = \begin{bmatrix} \cos 2\pi\omega & \omega^{-1}\sin 2\pi\omega \\ -\omega\sin 2\pi\omega & \cos 2\pi\omega \end{bmatrix}. \quad (14)$$

The eigenvalues (multiplicators) of the matrix are as follows:

$$\rho_{1,2} = \cos 2\pi\omega \pm i\sin 2\pi\omega. \quad (15)$$

For all values $\omega \neq \dfrac{k}{2}$, $k = 1, 2, \ldots$, the multiplicators are complex conjugate and lie on the unit circle (stability). Since $\mathrm{Tr}\mathbf{G} = 0$ for the system of Eqs. (7) and (8) for $\beta = 0$, the corresponding characteristic equation is reciprocal [4–6]. For this reason, under small variations of the parameters ω and ε, simple multiplicators cannot leave the unit circle. We will show that the presence of friction ($\beta > 0$) results in the asymptotic stability of the system in this case.

Using Eqs. (8), (10), and (12)–(14), we obtain the following approximate expression for the monodromy matrix $\mathbf{F}$ including the terms of the order β:

$$\mathbf{F} = \mathbf{F}_0(\mathbf{I} + \mathbf{A}\beta), \quad (16)$$

where F_0 is determined in Eq. (14) and

$$\mathbf{A} = \begin{bmatrix} \dfrac{\sin 4\pi\omega}{4} - \pi\omega & \dfrac{\sin^2 2\pi\omega}{2\omega} \\ \dfrac{\omega\sin^2 2\pi\omega}{2} & -\dfrac{\sin 4\pi\omega}{4} - \pi\omega \end{bmatrix}. \quad (17)$$

From Eqs. (16) and (17), we obtain

$$\begin{aligned} \det\mathbf{F} &= \det\mathbf{F}_0\det(\mathbf{I} + \mathbf{A}\beta) = 1 + \beta\mathrm{Tr}\mathbf{A} + o(\beta) \\ &= 1 - 2\pi\beta\omega + o(\beta). \end{aligned} \quad (18)$$

Since the monodromy matrix determinant is equal to the product of two complex-conjugate multiplicators, $|\rho_{1,2}| < 1$ follows from Eq. (18) at fairly small values of $\beta > 0$, which implies asymptotic stability.

Therefore, instability (parametric resonance) can occur only near the points

$$\mathbf{p}_0: \quad \varepsilon = 0, \quad \beta = 0, \quad \omega = \frac{k}{2}, \quad k = 1, 2, \ldots, \quad (19)$$

where the multiplicators are doubled.

For determining the parametric resonance domains, the monodromy matrix $\mathbf{F}$ near the points $\mathbf{p}_0$ is expanded in a Taylor series in the parameters ε, β, and $\Delta\omega = \omega - \dfrac{k}{2}$:

$$\mathbf{F}(\mathbf{p}) = \mathbf{F}(\mathbf{p}_0) + \frac{\partial\mathbf{F}}{\partial\varepsilon}\varepsilon + \frac{\partial\mathbf{F}}{\partial\beta}\beta + \frac{\partial\mathbf{F}}{\partial\omega}\Delta\omega + \ldots. \quad (20)$$

Using Eqs. (8), (13), and (14), we calculate the derivatives $\dfrac{\partial\mathbf{F}}{\partial\varepsilon}$, $\dfrac{\partial\mathbf{F}}{\partial\beta}$, and $\dfrac{\partial\mathbf{F}}{\partial\omega}$ at $\mathbf{p} = \mathbf{p}_0$ from formulas (10). As a result, the expression

$$\mathbf{F}(p)$$

$$= \cos\pi k \begin{bmatrix} 1 + \dfrac{3}{4}k\pi b_k\varepsilon - \dfrac{1}{2}k\pi\beta & \dfrac{4}{k}\pi\Delta\omega - \dfrac{3}{2}\pi a_k\varepsilon \\ -k\pi\Delta\omega - \dfrac{3}{8}k^2\pi a_k\varepsilon & 1 - \dfrac{3}{4}k\pi b_k\varepsilon - \dfrac{1}{2}k\pi\beta \end{bmatrix} \quad (21)$$

correct to first-order terms is obtained from Eq. (12). Here,

$$a_k = \frac{1}{\pi}\int_0^{2\pi}\varphi(\tau)\cos k\tau\, d\tau,$$

$$b_k = \frac{1}{\pi}\int_0^{2\pi}\varphi(\tau)\sin k\tau\, d\tau, \quad k = 1, 2, \ldots \quad (22)$$

are the Fourier coefficients of the function $\varphi(\tau)$.

Approximate expressions for the multiplicators of matrix (21) are determined in the form

$$\rho_{1,2} = (-1)^k\left(1 - \frac{1}{2}k\pi\beta\right) \pm \pi\sqrt{D}, \quad (23)$$

$$D = k^2 r_k^2\varepsilon^2 - (2\Delta\omega)^2, \quad r_k = \frac{3}{4}\sqrt{a_k^2 + b_k^2}. \quad (24)$$

The system is unstable if at least one of the multiplicators is less than unity in absolute value [5, 6]. For $\beta < 0$, this condition is fulfilled and the system is unstable. For $\beta \geq 0$, this condition is fulfilled only when $\sqrt{D} > \dfrac{1}{2}\beta k$.

Thence, in view of Eq. (24), the domain of instability (parametric resonance) lies inside the half-cone

$$\frac{k^2\beta^2}{4} + 4\left(\omega - \frac{k}{2}\right)^2 < k^2 r_k^2\varepsilon^2, \quad \beta \geq 0, \quad (25)$$

joining with the $\beta < 0$ half-space (Fig. 2). This inequality can also be represented in the more convenient form

$$\left(\frac{\beta}{2}\right)^2 + \left(\frac{2\omega}{k} - 1\right)^2 < r_k^2\varepsilon^2, \quad \beta \geq 0. \quad (26)$$

Hence, in particular, the kth resonance domain depends only on the kth Fourier coefficients of the periodic excitation function. We note that formulas (25) and (26) are the first-order approximations for the instability domains. For $a_k = 0$ and $b_k = 0$, $r_k = 0$, and the first-order

approximations degenerate to the straight line $\beta = 0$ and $\omega = \dfrac{k}{2}$. In this case, to determine the resonance domain more accurately, higher order approximations should be used. This can also mean that the corresponding resonance domain is empty.

Setting $\beta = 0$ in Eq. (25), we obtain the parametric resonance domains in the absence of friction:

$$-\frac{kr_k}{2} < \frac{\omega - k/2}{\varepsilon} < \frac{kr_k}{2}. \qquad (27)$$

The section of cone (25) by the plane $\beta = \text{const}$, $\beta \geq 0$ gives a parametric resonance domain bounded by a hyperbola (Fig. 3). The asymptotes of the hyperbola are determined from inequalities (27). In the presence of friction ($\beta > 0$), the minimum amplitude of resonance excitation is equal to $\varepsilon_{\min} = \dfrac{\beta}{2r_k}$ according to Eq. (25).

The section of domain (25) by the plane $\varepsilon = \text{const}$ represents a semiellipse with the semiaxes $\left|\omega - \dfrac{k}{2}\right| = \dfrac{kr_k\varepsilon}{2}$ and $\beta = 2r_k\varepsilon$ (Fig. 4). We note that the resonance domain in the frequency ω shrinks with an increase in the friction coefficient β and disappears at $\beta > 2r_k\varepsilon$.

We will analyze the behavior of the resonance domains with an increase in the resonance number k. It is known that, if a periodic function $\varphi(\tau)$, together with its sth-order derivatives, is continuous, the Fourier coefficients a_k and b_k behave as $a_k k^{s+1} \to 0$ and $b_k k^{s+1} \to 0$ for $k \to \infty$. Therefore, for continuously differentiable functions, the quantities kr_k tend to zero for $k \to \infty$. This means that cone (25) shrinks when k increases. Moreover, the minimum amplitude $\varepsilon_{\min} = \dfrac{\beta}{2r_k}$ of resonance excitation increases without bound when k increases at a fixed β value. Owing to this behavior, it is easier to set a swing into motion at the lower resonances $k = 1$ and 2, whereas large excitation amplitudes and forces must be applied to achieve resonance for higher k values.

From Eqs. (3) and (19), we obtain that setting a swing into motion occurs at the excitation frequencies Ω near to the critical values

$$\Omega_k = \frac{2}{k}\sqrt{\frac{g}{l_0}}, \quad k = 1, 2, \dots. \qquad (28)$$

We note that the quantity $\sqrt{\dfrac{g}{l_0}}$ is the natural frequency of a pendulum with the mean length l_0. According to
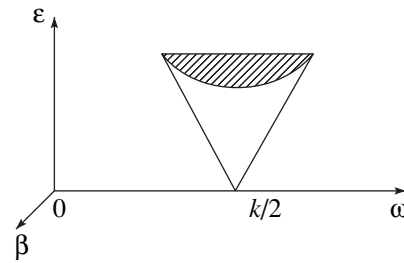

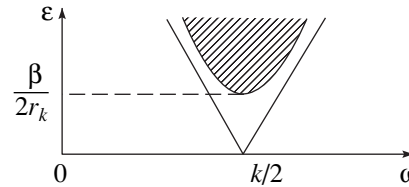**Fig. 2.** Domains of instability (parametric resonance).

Fig. 3. Section of the instability domain by the $\beta = \text{const}$ plane.
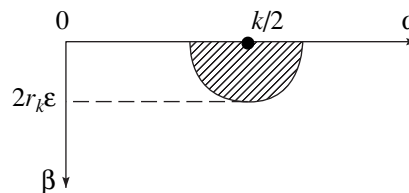

Fig. 4. Section of the instability domain by the $\varepsilon = \text{const}$ plane.

Eq. (26), the corresponding resonance domains are described by the expressions

$$\frac{\gamma^2 l_0}{4gm^2} + \left(\frac{\Omega}{\Omega_k} - 1\right)^2 < \frac{r_k^2 a^2}{l_0^2}. \qquad (29)$$

This formula is similar to the expression obtained in [9] for the instability domains of a pendulum with a vertically oscillating suspension point and differs from the latter by the dependence of the right-hand sides of the inequalities on the resonance number k. This difference can apparently be attributed to the fact that the equation of oscillations of the pendulum with the oscillating suspension point involves an acceleration proportional to the square of the excitation frequency.

3. As an example, we will consider oscillations excited by the periodic piecewise constant function

$$\varphi(\tau) = \begin{cases} 1, & 0 \leq \tau \leq \pi \\ -1, & \pi < \tau \leq 2\pi. \end{cases} \qquad (30)$$

For this function, we have

$$a_{2k-1} = 0, \quad b_{2k-1} = \frac{4}{\pi(2k-1)},$$

$$r_{2k-1} = \frac{3}{\pi(2k-1)}, \qquad (31)$$

$$a_{2k} = 0, \quad b_{2k} = 0, \quad r_{2k} = 0,$$

$$k = 1, 2, \dots.$$

Thus, all even resonance domains are degenerate in the first approximation, while odd domains are described by formula (29). Substituting $\gamma = 0$, $k = 1$, and $r_k = \frac{3}{\pi}$ into Eq. (29), we obtain the following formula for the first resonance domain of the frictionless system with the piecewise constant excitation function (30):

$$2\sqrt{\frac{g}{l_0}}\left(1 - \frac{3a}{\pi l_0}\right) < \Omega < 2\sqrt{\frac{g}{l_0}}\left(1 + \frac{3a}{\pi l_0}\right). \qquad (32)$$

This result coincides with that obtained in [1] [formulas (4.74)–(4.76) in that study] if $\Omega = 2\omega_0 + \Delta\Omega$ is substituted into Eq. (4.74) from [1] and the approximate equality

$$\tan\frac{\pi\omega_0}{2\Omega} \approx 1 + \frac{\pi\Delta\Omega}{4\omega_0}$$

is used. This also coincides with the result obtained in [3] in a more complicated form.

For $\varphi(\tau) = \cos\tau - \sin 2\tau$, we obtain $a_1 = 1$, $b_2 = -1$, $a_2 = b_1 = 0$, and $r_1 = r_2 = \frac{3}{4}$ and $a_k = b_k = r_k = 0$, $k = 3$, 4, …. Thus, all resonance domains are degenerate, except for the first and second ones.

In accordance with Eqs. (28) and (29), we obtain the following inequality for the first resonance domain:

$$\frac{\gamma^2 l_0}{4gm^2} + \left(\frac{\Omega}{2\sqrt{g/l_0}} - 1\right)^2 < \frac{9a^2}{16l_0^2}. \qquad (33)$$

In the absence of air resistance ($\gamma = 0$), hence follows the relation

$$2\sqrt{\frac{g}{l_0}}\left(1 - \frac{3a}{4l_0}\right) < \Omega < 2\sqrt{\frac{g}{l_0}}\left(1 + \frac{3a}{4l_0}\right) \qquad (34)$$

for the first resonance domain. Similar expressions can be obtained for the second resonance.

REFERENCES

1. K. Magnus, *Schwingungen* (Teubner, Stuttgart, 1961; Mir, Moscow, 1982).
2. Ya. G. Panovko and I. I. Gubanova, *Stability and Oscillations of Elastic Systems: Modern Concepts, Paradoxes, and Fallacies* (Nauka, Moscow, 1987).
3. S. L. Chechurin, *Parametric Oscillations and Stability of Periodic Motion* (Leningr. Gos. Univ., Leningrad, 1983).
4. V. I. Arnold, *Mathematical Methods of Classical Mechanics* (Nauka, Moscow, 1989; Springer-Verlag, New York, 1989).
5. I. G. Malkin, *Theory of Motion Stability* (Nauka, Moscow, 1966).
6. V. A. Yakubovich and V. M. Starzhinskiǐ, *Parametric Resonance in Linear Systems* (Nauka, Moscow, 1987).
7. A. P. Seyranian, F. Solem, and P. Pedersen, Arch. Appl. Mech. **69**, 160 (1999).
8. A. P. Seyranian, F. Solem, and P. Pedersen, J. Sound Vib. **229** (1), 89 (2000).
9. A. P. Seyranian, Dokl. Akad. Nauk **376** (1), 44 (2001) [Dokl. Phys. **46**, 41 (2001)].

Translated by M. Lebedev